Advanced physical modelling of step graded Gunn Diode for high power TeraHertz Sources

A thesis submitted to The University of Manchester for the degree of
Doctor of Philosophy
in the Faculty of Engineering and Physical Sciences

2011

FAISAL AMIR

SCHOOL OF ELECTRICAL AND ELECTRONIC ENGINEERING

TABLE OF CONTENTS

Words count, including footnotes and endnotes: 36,822

LIST OF FIGURES

LIST OF TABLES

LIST OF ABBREVIATIONS

2D	Two Dimensional
ACC	Adaptive Cruise Control
ACCS	Adaptive Cruise Control Systems
ADS	Advanced Design System by Agilent Technologies
AlAs	Aluminium arsenide
AlGaAs	Aluminium gallium arsenide
AlSb	Aluminium Antimonide
As	Arsenic
AWR	Advancing the Wireless Revolution
BARITT	Barrier Injection Transit Time
CB	Conduction band
cc	Carrier Concentration
CdTe	Cadmium Telluride
CMS	Collision Mitigation Systems
CO2	Carbon dioxide
CVD	Chemical Vapour Deposition
CW	Continuous Wave
DC	Direct Current
EM	ElectroMagnetic
fF	Femto Farad
FMCW	Frequency Modulated Continuous Wave
Ga	Gallium
GaAs	Gallium arsenide
GaAsP	Gallium Arsenide Phosphide
GaInAs	Gallium Indium arsenide
GaN	Gallium Nitride
GHz	Gega Hertz
HFSS	High Frequency Structure Simulator
IMPATT	Impact Ionization Transit Time
InAs	Indium arsenide

Inc	Incorporation
InP	Indium Posphide
I-V	Current-Voltage
K	Kelvin
L	Satellite
LSA	Low Space-charge Accumulation
MBE	Molecular Beam Epitaxy
micron	micrometre
MITATT	Mixed Tunnelling-Avalanche Transit-Time
mm	milli metre
MMIC	Monolithic Microwave Integrated Circuit
mW	milli watt
NDR	Negative Differential Resistance
Plc	public limited company
RF	Radio Frequency
RIE	Reactive Ion Etching
RTD	Resonant Tunnelling Diode
SI	Semi-Insulating
SRH	Shockley-Read-Hall
STFC	Science and Technology Facilities Council
TADAR	Tactical Area Defence Alerting Radar
TCAD	Technology Computer-Aided Design
TD	Tunnel diode
TDTS	Time-domain THz Spectroscopy
TED	Transferred Electron Devices
TEM	Transverse ElectroMagnetic
THz	Terahertz
Ti	Titanium
TM	Trademark
TUNNETT	Tunnel Injection Transit Time
UMS	Universal Marking Systems Ltd
VWF	Virtual Wafer Fab
ZnSe	Zinc Selenide
Γ	Gamma

ABSTRACT

The mm-wave frequency range is being increasingly researched to close the gap between 100 to 1000 GHz, the least explored region of the electromagnetic spectrum, often termed as the 'THz Gap'. The ever increasing demand for compact, portable and reliable THz (Terahertz) devices and the huge market potential for THz system have led to an enormous amount of research and development in the area for a number of years. The Gunn Diode is expected to play a significant role in the development of low cost solid state oscillators which will form an essential part of these THz systems.

Gunn and mixer diodes will "power" future THz systems. The THz frequencies generation methodology is based on a two-stage module. The initial frequency source is provided by a high frequency Gunn diode and is the main focus of this work. The output from this diode is then coupled into a multiplier module. The multiplier provides higher frequencies by the generation of harmonics of the input signal by means of a non-linear element, such as Schottky diode Varactor. A realistic Schottky diode model developed in SILVACO^{TM} is presented in this work.

This thesis describes the work done to develop predictive models for Gunn Diode devices using SILVACO^{TM}. These physically-based simulations provide the opportunity to increase understanding of the effects of changes to the device's physical structure, theoretical concepts and its general operation. Thorough understanding of device physics was achieved to develop a reliable Gunn diode model. The model development included device physical structure building, material properties specification, physical models definition and using appropriate biasing conditions.

The initial goal of the work was to develop a 2D model for a Gunn diode commercially manufactured by e2v Technologies Plc. for use in second harmonic mode 77GHz Intelligent Adaptive Cruise Control (ACC) systems for automobiles.

This particular device was chosen as its operation is well understood and a wealth of data is available for validation of the developed physical model. The comparisons of modelled device results with measured results of a manufactured device are discussed in detail. Both the modelled and measured devices yielded similar I-V characteristics and so validated the choice of the physical models selected for the simulations. During the course of this research 2D, 3D rectangular, 3D cylindrical and cylindrical modelled device structures were developed and compared to measured results.

The injector doping spike concentration was varied to study its influence on the electric field in the transit region, and was compared with published and measured data.

Simulated DC characteristics were also compared with measured results for higher frequency devices. The devices mostly correspond to material previously grown for experimental studies in the development of D-band GaAs Gunn devices. Ambient temperature variations were also included in both simulated and measured data.

Transient solutions were used to obtain a time dependent response such as determining the device oscillating frequency under biased condition. These solutions provided modelled device time-domain responses. The time-domain simulations of higher frequency devices which were developed used modelling measured approach are discussed. The studied devices include 77GHz (2nd harmonic), 125 GHz (2nd harmonic) and 100 GHz fundamental devices.

During the course of this research, twelve research papers were disseminated.

The results obtained have proved that the modelling techniques used, have provided predictive models for novel Transferred Electron Devices (TEDs) operating above 100GHz.

DECLARATION

No portion of the work referred to in the thesis has been submitted in support of an application for another degree or qualification of this or any other university or other institute of learning.

COPYRIGHT STATEMENT

I. The author of this thesis (including any appendices and/or schedules to this thesis) owns certain copyright or related rights in it (the “Copyright”) and he has given The University of Manchester certain rights to use such Copyright, including for administrative purposes.

II. Copies of this thesis, either in full or in extracts and whether in hard or electronic copy, may be made only in accordance with the Copyright, Designs and Patents Act 1988 (as amended) and regulations issued under it or, where appropriate, in accordance with licensing agreements which the University has from time to time. This page must form part of any such copies made.

III. The ownership of certain Copyright, patents, designs, trade marks and other intellectual property (the “Intellectual Property”) and any reproductions of copyright works in the thesis, for example graphs and tables (“Reproductions”), which may be described in this thesis, may not be owned by the author and may be owned by third parties. Such Intellectual Property and Reproductions cannot and must not be made available for use without the prior written permission of the owner(s) of the relevant Intellectual Property and/or Reproductions.

IV. Further information on the conditions under which disclosure, publication and commercialisation of this thesis, the Copyright and any Intellectual Property and/or Reproductions described in it may take place is available in the University IP Policy, The University Library’s regulations and in The University’s policy on presentation of Theses.

(see http://www.campus.manchester.ac.uk/medialibrary/policies/intellectual-property.pdf), (see http://www.manchester.ac.uk/library/aboutus/regulations).

ACKNOWLEDGEMENTS

I would like to thank my supervisor Prof M Missous, for his guidance and encouragement in the project, which motivated me to learn and develop the skills for modelling performed using the SILVACO^{TM} software. These physically based engineering model simulations provided me an opportunity to increase understanding of changes to the device physical structure, theoretical concepts and its general operation. Thanks also to Dr. Novak Farrington who remained involved with the research work and provided the best possible help and support. His valuable time spent on different aspects of project discussions, provision of experimentally measured data and suggestions for the write-up resulted in high quality research.

I would like to thank the M&N group PhD students performing semiconductor device modelling for their encouragement, motivation and assistance when required during the device model development phase.

The National University of Sciences and Technology (NUST, Pakistan) is greatly acknowledged for supporting my PhD studies under ‘faculty development programme’. Thanks to my supervisor who arranged finances from the School of Electrical and Electronic Engineering (E&EE) and M&N Group, which allowed me to remain focused and achieve research goals. Thanks are also due to the IEEE Electron Devices Society for the award of a PhD fellowship in August 2009. Thanks are also due to Mike Carr (e2v Technologies Plc, UK) for providing the experimentally measured data for the Gunn diodes.

DEDICATION

This thesis is dedicated to my family.

In particular to my

caring parents and beloved wife Fatima.

gorgeous daughter Farheen Wardah and

adorable son Muhammad Daud, both born

during the course of this research work

Chapter 1 Introduction

1.1 Project Overview

The aim of this project was to develop a physical model for an advanced GaAs hot electron injector Gunn diode to be used as a high power terahertz source. The physically-based model has been developed in SILVACO^{TM}, Inc.-TCAD (Technology Computer-Aided Design) using the ATLAS^{TM} Virtual Wafer Fab^{TM} (VWF^{TM}) device simulation software. The model I-V simulation response was then compared to the fabricated devices measured data to validate the various models used during simulations and their associated material parameters. The injector performance was evaluated and the effects of doping spike carrier concentration were studied. Time domain transient simulations were performed to determine modelled devices operating frequency and to investigate transit length scaling effects on device performance.

A Schottky diode 2D model was also developed in ATLAS^{TM} to study the underlying device physics and extract parameters to be used in harmonic balance simulations created using Microwave Office ® by AWR (Advancing the Wireless Revolution) Corporation.

1.2 Project Motivation

The research work was undertaken as part of the STFC (Science and Technology Facilities Council) funded project, ‘High Power Semiconductor Terahertz Frequency Sources for Imaging Applications’. The research was aimed at accessing the THz region through the use of high frequency Gunn diodes in conjunction with frequency multipliers. The project was a joint collaboration between The University of Manchester (UoM) and e2v Technologies (UK) Plc. The main objective of this project was to design, fabricate and test the components (Gunn diodes and multipliers) covering the range 100 to 600 GHz. This was planned to be achieved by the development and delivery of high power graded gap Gunn diodes with measurable output of at least 20 to 40 mW at 200

GHz and novel multipliers sources with overall efficiency of at least 5% for 600 GHz operation.

e2v Technologies (UK) Plc have been working on step-graded gap diodes for automotive applications at 77 GHz for over a decade whilst developing technologies to increase the operational frequency of these GaAs devices to well over 100 GHz [13].

This research work presented here is focused on predictive modelling of Gunn diodes using the SILVACO^{TM} software package. The developed model was ruggedly tested against actual data at 77GHz to demonstrate its worth to forming a bench mark for future predictive device modelling and research. It was then used as the basis for predicting the response and performance characteristic of higher frequency Gunn diodes prior to their fabrication. The model proved to be an extremely useful tool for the optimisation of the required epitaxial structures.

1.3 Research Papers

The following papers have been presented during the course of this research work.

1. N. Farrington, **F. Amir**, J. Sly and M. Missous, 'SILVACO modelling of a Gunn diode with step-graded hot-electron injector, and pulsed DC testing of on-wafer quasi-planar mm-wave Gunn diode structures', *16th European Workshop on Heterostructure Tech., HETECH'07*, 2-5 Sept 07, Fréjus, France, pp. Tu2-7. Research undertaken as part of MSc Dissertation project 'Terahertz (THz) Sources for Space and Security Applications'.
http://www.crhea.cnrs.fr/hetech07/index.htm

2. **F. Amir**, N. Farrington, J. Sly and M. Missous, 'Step-graded Hot Electron Injector Gunn Diode Modelling in SILVACO', *Workshop on Theory, Modelling and Computational Methods for Semiconductor Materials And Nanostructures*, 31 Jan – 1 Feb 08, The University of Manchester, UK.
http://www.eee.manchester.ac.uk/research/groups/mandn/docs/abstractsv3.pdf

3. **F. Amir**, N. Farrington, J. Sly and M. Missous, 'Physical Modelling of a GaAs Gunn Diode with a Step-graded AlGaAs Hot Electron Injector', *UK semiconductors 2008*, 2-3 Jul 08, University of Sheffield, Sheffield, UK.
http://www.uksemiconductors.com/

4. **F. Amir**, N. Farrington, T. Tauqeer, M. Missous, 'Physical Modelling of a Step-Graded AlGaAs/GaAs Gunn Diode and Investigation of Hot Electron Injector Performance', *Advanced Semiconductor Devices and Microsystems, 2008. ASDAM 2008. International Conference* pp.51-54, 12-16 Oct 08.
http://ieeexplore.ieee.org/xpls/abs_all.jsp?arnumber=4743356

5. T. Tauqeer, J. Sexton, **F. Amir**, M. Missous, 'Two-Dimensional Physical and Numerical Modelling of InP-based Heterojunction Bipolar Transistors,' *Advanced Semiconductor Devices and Microsystems, 2008. ASDAM 2008. International Conference*, pp.271-274, 12-16 Oct 08.
http://ieeexplore.ieee.org/xpls/abs_all.jsp?arnumber=4743335

6. **F. Amir**, N. Farrington, T. Tauqeer and M. Missous, 'A Novel Physical Model Developed of an Advanced Cylindrical Step Graded Heterostructure mm-wave Gunn Diode', *17th European Workshop on Heterostructure Technology, HETECH'07*, 2-5 Nov 08, Venice, Italy.
http://www.hetech2008.org/

7. **F. Amir**, C. Mitchell, N. Farrington and M. Missous, 'Advanced Step-graded Gunn Diode for mm-wave Imaging Applications', *5th ESA Workshop on Millimetre Wave Technology and Applications and 31st ESA Antenna Workshop*, 18-20 May 09, ESTEC, Noordwijk, The Netherlands, pp. 201-205.
http://www.congrex.nl/09c05/

8. T. Tauqeer, J. Sexton, M. Mohiuddin, R. Knight, **F. Amir** and M. Missous, 'Physical modelling of base-dopant out diffusion in Single Heterojunction Bipolar Transistors', *UK semiconductors 2009*, 1-2 Jul 09, University of Sheffield, Sheffield, UK.
http://www.uksemiconductors.com/

9. **F. Amir**, C. Mitchell, N. Farrington and M. Missous, 'Advanced Gunn Diode as High Power Terahertz Source for a Millimetre Wave High Power Multiplier', *SPIE Europe Security + Defence 2009*, 31 Aug to 03 Sept 09, Berliner Congress Centre, Berlin, Germany, Proc. SPIE, vol. 7485, pp 748-50I.
http://spie.org/x648.html?product_id=830296

10. **F. Amir**, C. Mitchell, N. Farrington, T. Tauqeer and M. Missous, 'Development of Advanced Gunn Diodes and Schottky Multipliers for High Power THz sources', *2nd UK/Europe-China Workshop on Millimetre Waves and Terahertz Technologies*, 19-21 Oct 09, Rutherford Appleton Laboratory (RAL), Oxford, UK pp. 80.
http://www.sstd.rl.ac.uk/mmt/ukchinathz2009.php

11. **F. Amir**, N. Farrington, C. Mitchell and M. Missous, 'Time-domain analysis of sub-micron transit region GaAs Gunn diodes for use in Terahertz frequency multiplication chains', *SPIE Europe Security + Defence 2010, SD108 'Millimetre Wave and Terahertz Sensors and Technology' (Session I - Millimetre and THz Devices)*, 20-23 Sept 10, Centre de Congrès Pierre Baudis, Toulouse, France. Proc. SPIE 7837, 783702 (2010).
http://spie.org/x648.html?product_id=864872

12. **F. Amir**, C. Mitchell and M. Missous, 'Development of Advanced Gunn Diodes and Schottky Multipliers for High Power THz sources', *Advanced Semiconductor Devices and Microsystems (ASDAM), 2010. 8th International Conference*, Smolenice, Slovakia, 25-27 Oct 10, pp. 29-32.
http://ieeexplore.ieee.org/xpls/abs_all.jsp?arnumber=5667005

1.4 Prizes / Awards

a. MSc Dissertation project 'Terahertz (THz) Sources for Space and Security Applications', research work adjudged best in the class and presented in 16th European Workshop on Heterostructure Technology (HeTech 07) held in Nice, France, September 2007.

b. Awarded 2009 IEEE EDS PhD Student Fellowship representing entire region 8 (Europe, Africa and Middle-East), for the demonstration of significant ability to perform independent research in the field of electron devices and a proven record of academic excellence.
http://eds.ieee.org/eds-phd-student-fellowship-program.html

c. The fellowship award was announced in January 2010 issue of EDS newsletter. A brief research progress report was published in July 2010 issue.
http://eds.ieee.org/eds-newsletters.html

d. Awarded 1st Prize during Post Graduate Research (PGR) Poster Conference 2009 at The University of Manchester, School of E&EE.
http://www.eee.manchester.ac.uk/research/pgr_conference/pgrconf09/

e. SPIE Europe Security + Defence 2009 Symposium's paper 'Advanced step-graded Gunn diode for millimetre applications' was published on the SPIE Newsroom page http://spie.org/x36521.xml?highlight=x2404&ArticleID=x36521.

f. In February 2010, nominated for the 2010 University of Manchester Distinguished Achievement Awards in category 'Postgraduate Research Student of the year', representing the School of E&EE, The University of Manchester.

1.5 Thesis Organization

The organization of the remainder of this thesis is as follows:

Chapter 2 briefly covers Terahertz technology and its applications with an emphasis on Gunn diodes. The multiplier and harmonic generation methodology is covered in Chapter 3. Chapter 3 presents an oscillator cavity developed in HFSS^{TM} at e2v. The harmonic balance simulation tool created in Microwave Office ® by AWR is discussed and both semiconductor components of the multiplier are also presented. Chapter 4 provides a detailed account of conventional Gunn diode theory with an explanation of the Negative Differential Resistance (NDR) effects, which depends on the bulk material properties.

Various device operating modes are presented with emphasis on the high frequency oscillations before summarizing the limitations of conventional Gunn diode. Chapter 5 will discus the concept and theory behind the hot electron injector. It would provides a literature survey of the step graded hot electron injector Gunn diode that has been developed to overcome the limitations of the conventional Gunn diode. Chapter 6 will provide a step-by-step process used to develop a model in SILVACO^{TM}. Chapter 7 would outline device physical models and discusses them in detail along with the material parameters used. Gunn diode DC I-V characteristics that are compared to the measured results will be presented in chapter 8. The doping spike carrier concentration optimization is also presented. Chapter 9 will discuss Gunn diode Time-domain analyses. Also presented would be the results of a novel 100 GHz fundamental device that has been simulated in an oscillator cavity. Chapter 10 will provide the conclusion and summary of the Gunn diode modelling work. It also gives a brief account of proposed future research work.

The appendices of this thesis contain SILVACO^{TM} codes.

Chapter 2 Terahertz Generation and Applications

2.1 Introduction

The Terahertz (THz) spectrum is being increasingly researched to close the frequency gap between microwaves and infrared. The THz region, typically referred to as the frequencies from 100 GHz to 10 THz, is the least explored region of the electromagnetic spectrum, often termed as the ‘THz Gap’. Table 1 list the common terminologies used to describe the frequency bands within this gap.

Frequency	Wavelength	Used term
30 to 300 GHz	10 mm to 1 mm	Millimetre
300 GHz to 3 THz	1 mm to100 μm	Sub millimetre [14]
100 GHz to 10 THz	3 mm to 30 μm	Terahertz [15]
3 to 30 THz	100 μm to 10 μm	Far infrared

Table 2.1 Terahertz terminology

THz waves can penetrate through dielectric materials such as fabrics, plastics and cardboard, which makes it an ideal choice to replace X-ray imaging and ultrasound imaging for security applications such as detecting concealed objects. Its non-ionizing properties and lower photon energy levels, milli-electron volt, makes it safe for people during security checks, inspection of various biological samples, etc. At THz frequencies the living tissues are semi-transparent and have ‘terahertz fingerprints’, permitting them to be imaged, identified, and analyzed. THz spectral imaging technology not only differentiates objects morphology, but it also identifies their composition. Additionally, it provides higher spatial resolution, and therefore an ideal choice for non-destructive testing.

THz radiation has higher frequency and bandwidth that provides short-distance high-capacity wireless communications. An increasingly widespread application is automotive FMCW (Frequency Modulated Continuous Wave) radar in the low atmospheric attenuation window at 77GHz (Fig. 2.1). The unique characteristics of THz radiation have important applications in the field of astrophysics, plasma physics, materials science, information science and engineering etc.

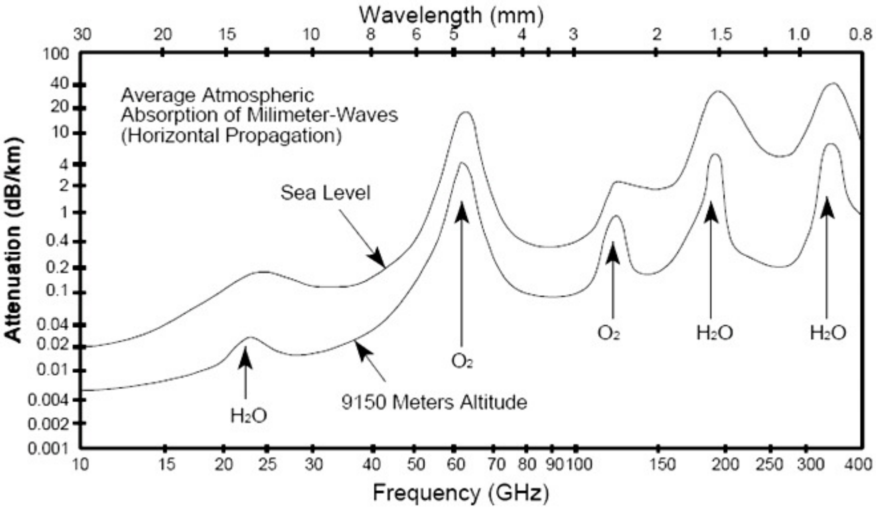

Fig. 2.1 Attenuation due to atmospheric absorption at microwave and millimetre wave frequencies [7]. At millimetre wave range, the attenuation not only increases, but becomes more dependent upon absorbing characteristics of H_2O and O_2.

The demand for high-frequency, high output power device technology has increased enormously in the past decade due to an array of emerging applications, which has resulted in focused and intense research in the field. This has led to an interest in the development of Physically-based models to aid in the development of next generation devices.

The Gunn Diode has long been considered the heart of mm-wave power generation. However, in recent years Monolithic Microwave Integrated Circuit (MMIC) solutions for power generation at mm-wave frequencies have become commercially viable but suffer from high cost and low output power levels as discussed later.

2.2 The Terahertz (THz) Spectrum

As shown in Fig. 2.2, THz frequencies correspond to photon energy levels from approximately 4 to 40 milli-electron volts or to an equivalent black body temperature between 50 and 500 Kelvin. The frequency range spans 100 GHz to

10 THz, which corresponds to wavelengths 3 mm to 30 µm [16]. The potential applications for THz devices have increased many fold during the past few years and range from security radar to medical imaging for tumour detection [17]. Other potential applications include high bandwidth communications, high resolution radar systems, security imaging systems and space exploration.

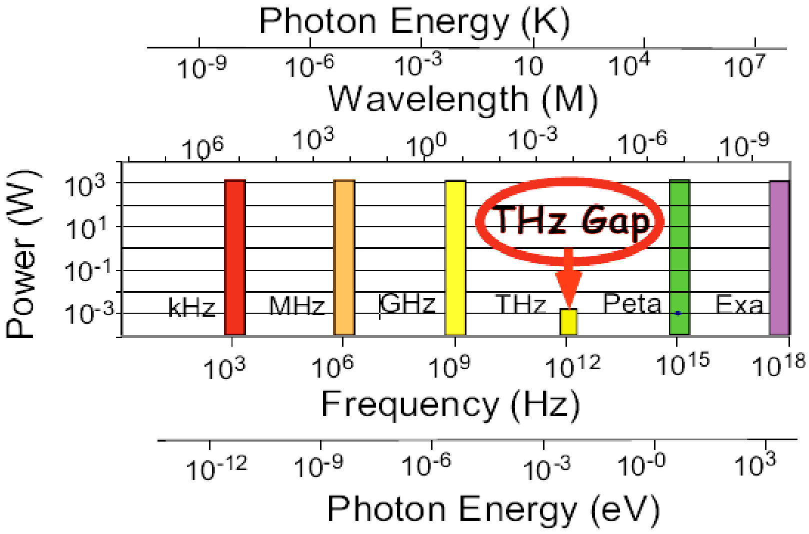

Fig. 2.2 **TeraHertz (THz) Gap [8]**

The transition from electronics to optics takes place in the infrared region of the electromagnetic spectrum where the wavelengths are less than 1mm. The lower-frequency region of the infrared is known as 'far infrared' and is generally considered as extension of the microwave region. Originally, the edge of the microwave band (300 GHz) was considered the highest viable frequency for electronics, but as technology has progressed, the limits of electronics have been pushed further into the infrared. However, the lower efficiency of both optical and electronic devices in the THz region has been a big impediment in the development of Terahertz systems. Therefore, research has been focused on the THz gap (Fig. 2.2) with aims to improve device efficiency and increase its output power levels [15]. In optics, apart from a few electron lasers, which reached the kilowatt power range [18], other laser sources are limited to milliwatt and microwatt power levels [8]. In electronics fabrication of 77 & 125 GHz systems using Gunn diode & MMIC technology have been developed. Although these currently operate in the mm-wave frequency range, they are being researched to extend in to the THz region [19].

2.3 THz Generation

Terahertz sources can be broadly divided into three categories namely, vacuum tube, optical and solid state sources. The vacuum tube sources are bulky, large and need huge power to generate substantial electric and magnetic fields and current densities. Additionally, their physical scaling is very difficult. The optical sources operate at very low energy levels ~meV. The low energy levels requires cryogenic cooling due to the effect of lattice phonons [16]. The electronic solid state sources are preferred for room temperature operation. They are limited due to parasitics and transit time effects. Their engineering becomes challenging due to power rolling off exponentially as the frequency increases.

2.4 Solid State two Terminal Active Devices for Terahertz Generation

Millimetre-wave frequencies can be generated using various two-terminal solid state active devices. The most commonly used devices include Transferred electron or Gunn diodes (TEDs) [20], Esaki tunnel diodes (TDs) [21], resonant tunnelling diodes (RTDs) [22] and transit-time diodes. The transit-time diodes includes Impact Ionization Transit Time (IMPATT) [23], Barrier Injection Transit Time (BARITT) [24], Tunnel Injection Transit Time (TUNNETT) [25] and Mixed Tunnelling-Avalanche Transit-Time (MITATT) [26, 27] diodes. All of these devices display the property of Negative Differential Resistance (NDR).

The transferred electron effect, tunnelling and transit-time diodes are discussed next;

2.4.1 Transferred Electron Devices (Gun Diodes)

The Gunn Diode named after J. B. Gunn [20] who discovered the effect named after him, is an active solid state two terminal device, classed as a Transferred Electron Device (TED). The most conspicuous feature of the device is the negative differential resistance, which depends on bulk material properties [28].

The Gun diode in its basic form is a homogenous two terminal device with an ohmic contact at each end. The device has a sandwich-like structure and comprises of n^+-n-n^+ semiconductor materials and is commonly grown using Molecular Beam Epitaxy (MBE). GaAs and InP are the most commonly used material systems although other materials such as CdTe, ZnSe, GaAsP and GaN may possibly also exhibit the transferred electron effect and are being researched for use at higher frequencies [29]. State of the art GaAs and InP Gunn diode output powers, and DC to RF conversion efficiencies are shown in Fig. 2.3. It can be seen that the output power of Gunn devices falls rapidly with the increase in frequency due to material limitations such as energy relaxation time. Generally two or more diodes are employed in conjunction with a frequency multiplier to achieve frequency generation above the fundamental limit e.g. from 200 GHz to 1 THz, with power levels of 0.1 to 1 mW at 400 GHz [6] being achieved.

Although GaAs or InP Gunn diode devices are simple in physical structure, they require extreme care during growth for optimization of physical parameters such as doping concentration and device length. The ohmic contact resistance needs to be as small as possible, as this can significantly affect device resistance and thus has considerable effect on the device operating frequency range. Devices operating in W-band (60 to 110 GHz) have typically specific contact resistivity values of less than $5\times10^{-6}\,\Omega cm^{-2}$, while for W-band and above (i.e. above 110 GHz) values of specific contact resistivity of $5\times10^{-7}\,\Omega cm^{-2}$ or less are required [30].

GaAs Gunn diodes currently being commercially fabricated provide moderate power levels of typically around 60 mW at 94 GHz for GaAs in second harmonic mode [31]. Due to low phase noise (-88 dBc / Hz at 100 KHz offset) at mm-wave frequencies, Gunn diodes are considered extremely suitable for Frequency Modulated Continuous Wave (FMCW) radar and imaging systems. However, the biggest problem of the Gunn diode is its low DC-to-RF conversion efficiency and associated high operational temperatures. Due to the high cost associated with device fabrication, physically-based predictive modelling can be used to complement experimentally verified devices. A typical model of an advanced Gunn Diode developed at Manchester, and used in commercial Adaptive Cruise Control Systems (ACCS) in BMW and Audi cars, is shown in Fig. 2.4.

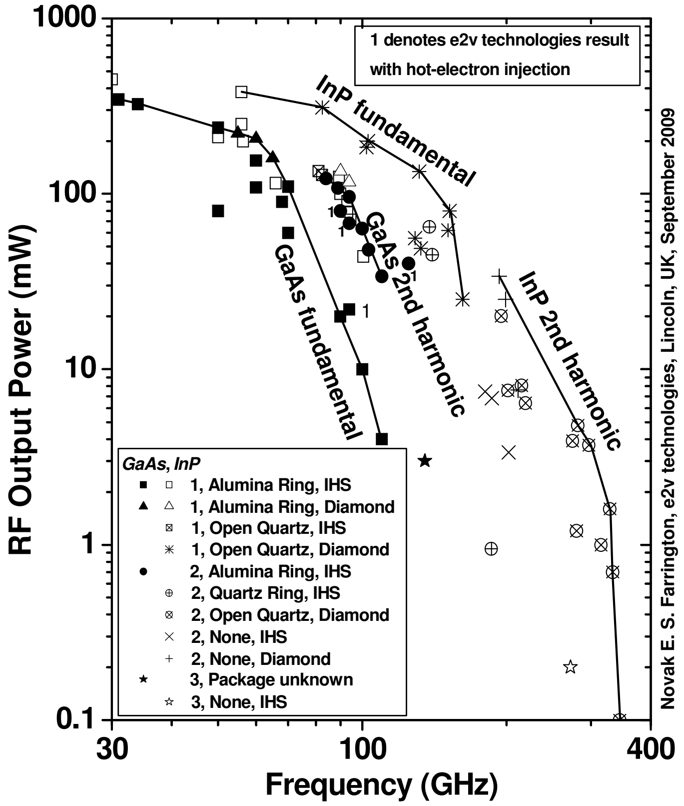

Fig. 2.3 Compilation of published state-of-the-art results between 30 and 400 GHz for GaAs and InP Gunn diodes under CW operation. Legend format: ‘mode of operation (‘1’ denotes fundamental, ‘2’ second-harmonic, etc.), package type, heatsink technology’. Solid lines outline the highest powers and frequencies achieved experimentally to-date from each material in fundamental and second-harmonic [6]

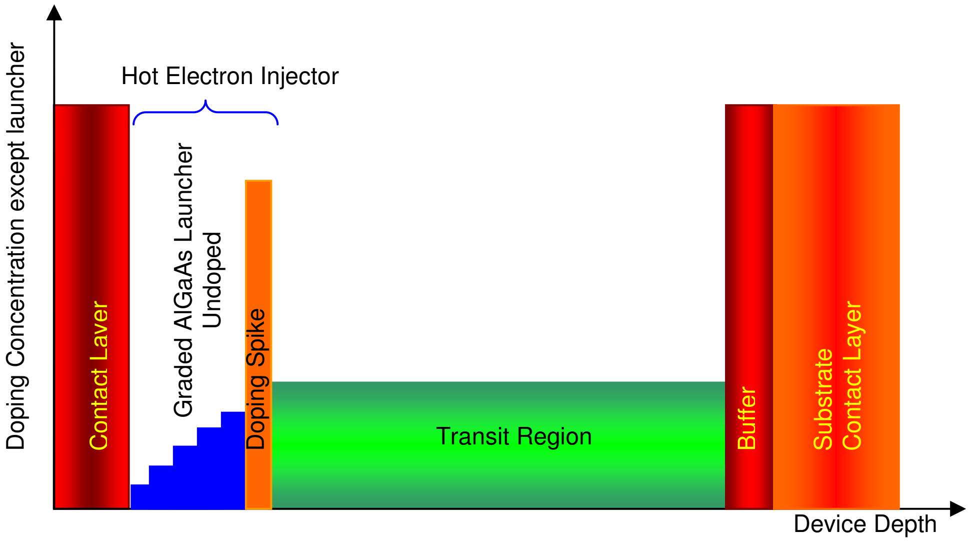

Fig. 2.4 Typical Advanced Gunn Diode Structure (not to scale)

2.4.2 Tunnelling Devices

Both Esaki Tunnel diodes (TDs) [21] and Resonant Tunnelling Diodes (RTDs) [22] fall under this category. These devices generate oscillations by exhibiting negative differential resistance in their I-V characteristics. They are active solid state two terminal devices and work on different tunnelling mechanisms. The TDs comprises of a heavily doped (degenerate) p^+-n^+ junction where interband tunnelling takes place from the valence band to the conduction band. In RTDs, the tunnelling occurs in the conduction bands of a double-barrier heterostructure.

In contrast to other solid state two terminal devices, both TDs and RTDs provide very low output power. The output power is limited by the small voltage swing (RF) and large junction capacitance. State of the art RTDs have achieved power levels of 0.3 µW at 712 GHz using InAs/AlSb RTD [32] and 1 µW at 831 GHz using GaInAs / AlAs double-barrier RTD [33].

2.4.3 Transit – Time Diodes

The transit-time diodes include devices that use special current injection mechanism and are categorized accordingly. These devices have carriers injected into a depletion region which drift through the device active region with the drift velocity. The drift velocity depends on the applied electric field in the active region. This creates a phase shift between device terminal voltage and current, which in turn creates a NDR and generates RF oscillations [34].

Various transit-time diodes carrier generation and injection is discussed as follows;

- In IMPATT diodes [23] carriers are generated and injected due to avalanche multiplication through impact ionization occurring in a reverse-biased p-n junction. These devices are known to be capable of providing high power at mm-wave frequencies. However, they not only require a high current source to operate but also due to the avalanche effect they have an inherently high phase-noise. Thus, their application as Local Oscillators (LOs) in FMCW systems is not a viable option. However, presently Si IMPATT diodes are being used in passive mm-wave radiometric imaging systems as incoherent noise sources for illumination [3].

- The BARITT diodes [24] generate microwave oscillations by using thermionic emission of carriers over a forward biased barrier. The barrier is formed due to p-n or Schottky junction or heterojunction, which contributes to positive active resistance by forming an RC circuit. Other BARITT diode limitations include longer active region, small NDR, low output power and efficiency as compared to IMPATT diodes [34].

- The TUNNETT diodes [25] have carriers injected by tunnelling. The tunnelling is band-to-band in case of a p-n junction and through the barrier for Schottky barriers. The TUNNETT diodes have lower noise then IMPATT diodes but are limited by low output power due to low tunnelling current. However, they can work at lower operating voltages and theoretically can achieve 1 THz. Experimentally, it has been shown that the TUNNETT diodes have achieved power levels of 7.9 mW at 655 GHz [35].

- MITAT diodes [26, 27] use both tunnelling and impact ionization mechanism for carrier generation. These devices have smaller carrier generation region and are designed for high frequency operation [26]. Their limitations include high noise level, small NDR, series resistance and poor impedance matching characteristics. It has been shown that the MITATT diodes have achieved power levels of 3 mW at 150 GHz [36].

2.5 Monolithic Microwave Integrated Circuit (MMIC)

MMIC solutions are generally preferred over hybrid technologies due to their reliability and increased functionality. This was reflected in the 2004 GaAs device market segmentation, which showed that 83% of the market was taken by MMIC technology, with the remaining 16% and 1% accounted for by discrete and digital ICs respectively [19].

In contrast to Gunn diode based systems, MMIC solutions have a compact design, can be easily integrated into planar circuits, do not require a cavity and can provide a higher degree of functionality. However, commercial MMIC solutions have yet not reached the output power levels provided by Gunn Diodes at mm-wave frequencies [37] and generally cost more. Recently, planar Gunn diodes work has produced promising results [38-41] but still the output power levels are low. The output power of state of the art planar Gunn has been reported as 1.58 µW at 115.5GHz [42] .

Commercially available low phase-noise pHEMT-based MMIC chip-sets generating a frequency of 77 GHz have been developed for automotive and general radar applications, where they exhibits a slightly lower phase noise than Gunn diode based oscillators. United Monolithic Semiconductors (UMS) has developed a MMIC based FMCW chipset using a low frequency oscillator MMIC (38.5 GHz) and a x2 frequency multiplier MMIC [19, 31].

2.6 Applications of THz Sources

Applications of THz Sources are discussed, including space, security, Imaging and spectroscopy systems, communications systems, mm-wave automotive RADAR systems and mm-wave RADAR industrial applications.

2.6.1 THz Space Applications

Receiver diode based heterodyne receivers have been extensively used by radio astronomers to investigate the composition and chemistry of interstellar matter, the energy budget of interstellar clouds and the process of star formation [43]. Other important scientific applications include diagnostics for nuclear fusion experiments and particle accelerators. Technology advancements continue due to upcoming challenging projects. For instance a new generation ‘Microwave Limb Sounder’ is being developed by NASA to monitor additional molecular species (such as hydroxide ion OH^-) at frequencies as high as 2.5 THz, which is expected to be installed on NASA’s ‘Earth Observing System’. Additionally, a Millimetre Array (MMA) radio telescope is being developed by the National Radio Astronomy Observatory. The MMA would cover all atmospheric windows from below 100 GHz through 1 THz. Although, ultra-low noise cryogenic superconductive junctions would be used for the mixers in MMA, LO powers would still be provided by the GaAs multiplier diodes [43].

Recently a mm-wave diode system was used to detect Space shuttle insulation foam defects. The system satisfactorily detected defects by using 12 mW, 0.2 THz Gunn diode oscillator [44].

2.6.2 THz Security Applications

The current geopolitical situation has increased the desire to have sophisticated and reliable mm-wave imaging systems in sensitive places. In particular both airport and sea port security markets are expected to grow exponentially [37]. Applications of THz imaging include detection of concealed weapons and recording the signatures of explosives and chemical & biological agents, which unlike x-ray imaging, causing no harm to the person or object being scanned.

2.6.3 THz Imaging and Spectroscopy Systems

Security screening of people is generally accomplished using stand off surveillance or portal screening. As an example the Smiths Detection company has developed a passive TADAR (Tactical Area Defence Alerting Radar) system with a detection range of 25 metres, the system uses 77 GHz, 94 GHz and 140 GHz sensors [45]. Portal screening generally uses a passive system optimized for wavelengths of around 77 GHz to 140 GHz). Clothes are transparent at these wavelengths and denser objects such as plastics and metals become clearly visible after image processing. Gunn diode oscillators are preferred for LO frequencies from 94 GHz upwards in both portal and stand off screening systems. However, higher frequency sources are desirable due to the higher spatial resolutions achievable.

The detection of explosives and their related compounds has been accomplished using Time-domain THz Spectroscopy (TDTS). Previous detection was limited to spectral regions less than 3 THz. However, it has been reported [46] that due to the advancement of emitters and sensors the spectra has now been extended from 0.5 to 6 THz. Thus four new explosives compounds, RDX (1, 3, 5 – Trinitroperhydro - 1, 3, 5 - Triazine), HMX (1, 3, 5, 7 – Tetranitroperhydro -1, 3, 5, 7 - tetrazocine), PETN (Pentaerythritol Tetranitrate), and TNT (2, 4, 6 - Trinitrotoluene) were successfully studied and evaluated [46].

2.6.4 Communications Systems

The relatively low costs associated with point-to-point line-of-sight ‘last mile’ communication links mean they are preferred over optical fibre connections, especially in urban built-up areas. Last mile communication links are currently available from Bridgewave Communications Inc. (30 GHz) and E-Band communications corp. (94 GHz) [19]. The offered per link cost is approximately one tenth of the MMIC chip-sets fibre link commercially available (UMS Ltd. and Northrop Grumman corporation) [19]. Operation of these links at higher frequencies is desirable due to the higher achievable bandwidths and narrow beam widths. The later being an important security consideration.

2.6.5 MM-Wave Automotive RADAR Systems

Radar is one of the most widely used mm-wave systems, whose spatial resolution increases with frequency due to narrowing of the achievable beamwidth. The main utilization of mm-wave radar systems to date has been in the automotive industry. A recent study by TRW Automotive ® 2011 showed that in North America road accidents involving heavy vehicles were reduced by 70 percent due to the installation of collision warning and avoidance systems on vehicles [47]. Radar systems using both Pulse Doppler and FMCW modes, operating at 77 GHz have been successfully installed and used in top of the range automobiles for over a decade. Future deployment of Collision Mitigation Systems (CMS), which would initiate various safety actions such as seatbelt pre-tensioning and airbags deployment upon detection of a probable collision has already begun [47].

2.6.6 MM-Wave RADAR Industrial Applications

Another significant FMCW radar application includes its utilization in a factory for vibration and displacement measurements. In this regard coherent radar operating at 37.5 GHz with 50 mW power has been developed and tested, which would be an alternate to traditional piezoelectric sensor measurements [48].

2.7 Conclusion

The THz spectrum is being increasingly researched to close the frequency gap between microwaves and infrared. Terahertz technology and its applications with an emphasis on Gunn diodes have been presented. It was shown that THz waves can be used for in the field of astrophysics, plasma physics, materials science, information science and engineering etc. Applications of THz Sources were discussed, including space, security, Imaging and spectroscopy systems, communications systems, mm-wave automotive RADAR systems and mm-wave RADAR industrial applications.

THz generation was discussed with a review of solid state two terminal active devices. The commonly used devices discussed included TEDs, Esaki TDs, RTDs and transit-time diodes. The transit-time diodes presented include IMPATT, BARITT, TUNNETT and MITATT diodes. It was shown that the Gunn Diode has long been considered the heart of mm-wave power generation. The development of Physically-based models is shown to aid in the development of next generation devices.

The MMIC solutions for THz generation were discussed. It was shown that MMIC solutions have a compact design, can be easily integrated into planar circuits, do not require a cavity and can provide a higher degree of functionality. However, commercial MMIC solutions have yet not reached the output power levels provided by Gunn Diodes at mm-wave frequencies.

Chapter 3 Multiplier and Harmonic generation for Terahertz frequency

3.1 Introduction

Gunn and mixer diodes will make a significant contribution to “power” future THz systems. The THz frequencies considered (up to 600 GHz) are to be generated in a two-stage module with the initial frequency source provided by the high frequency Gunn diodes. The output from these diodes is then coupled into a multiplier module. The realisation of high power Gunn diodes operating at higher frequency, enable THz generation with a single stage multiplier module. A single stage multiplier potentially reduces losses and increases output power, whilst also providing a simpler, lighter and cheaper device for room temperature operation. The key technology issues are therefore Gunn diode designs and packaging to provide adequate power at high frequencies and the efficiency of a single stage multiplier. The multiplier provides higher frequencies by the generation of harmonics of the input signal by means of a non-linear element. In this case the non-linear element is provided by a Schottky diode Varactor with low RC time constants to increase efficiency.

Design considerations of the microstrip and multiplier block are discussed in the next section. The semiconductor materials for such a complete device including modelling, design and testing; focusing in depth on the Gunn diode module and Schottky diode are also presented.

3.2 Gunn Diode Oscillator Design

The accurate physical modelling of Gunn diodes requires them to be mounted in an oscillator circuit. The circuit provides DC power, and couples out the generated RF power. The circuit will have reactive elements and a resonant frequency associated with it. The circuit can therefore be designed to resonate with the Gunn diode in order to optimise output power and efficiency at a given frequency. At millimetre-wave frequencies the most common circuit configuration used to do this is the waveguide-based second-harmonic resonant disk oscillator. A schematic diagram of the cross-section of a second harmonic resonant disk oscillator is shown in Fig. 3.1-3.2.

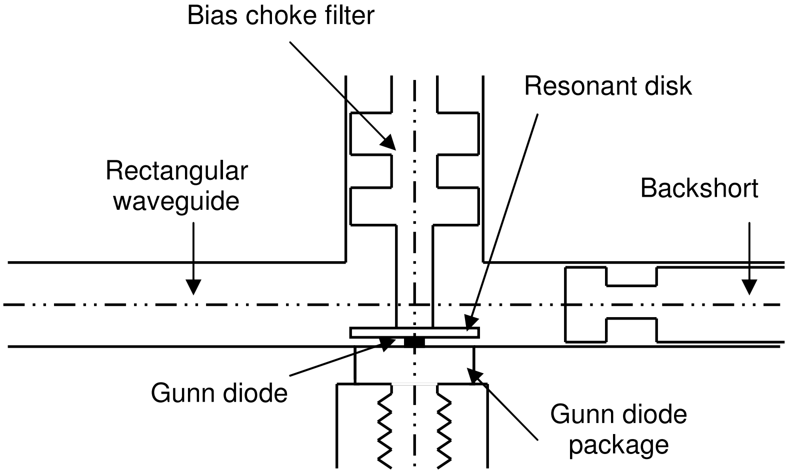

Fig. 3.1 Simplified schematic of the mechanical outline of a second harmonic resonant disk Gunn diode oscillator.

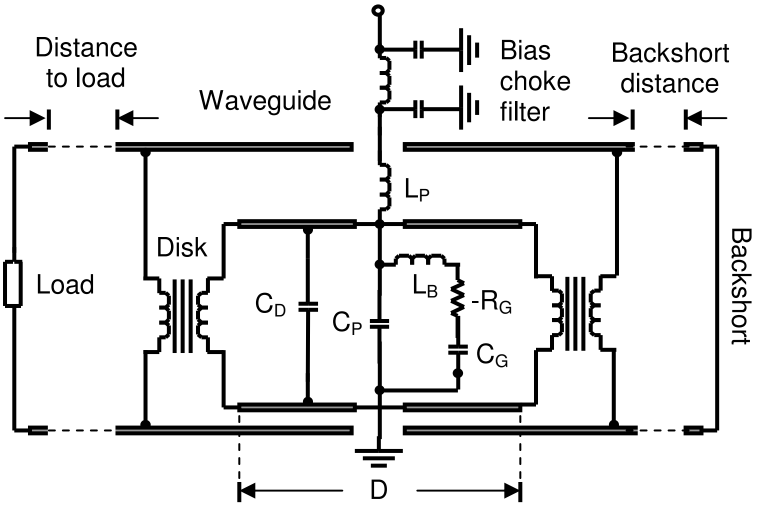

Fig. 3.2 Equivalent electrical circuit model of a second harmonic resonant disk Gunn diode oscillator.

In a resonant disk oscillator the packaged diode will typically be positioned on or near the waveguide floor and the DC power for the diode is supplied through the bias post and choke assembly (often a single piece of machined metal), which is insulated from the waveguide block. The operational principle is such that three distinct electromagnetic modes of propagation exist [12, 49]: a TE01 rectangular waveguide mode (in the rectangular waveguide section) at second harmonic frequency, a radial mode (between the resonant disk and the waveguide floor), and a quasi-coaxial (quasi-TEM) mode (between the resonant disk and the bottom of the choke). Operation is such that a fundamental frequency resonance exists in the TEM (Transverse ElectroMagnetic) mode along the quasi-coaxial line between the choke and the disk. The radial disk couples energy between the magnetic fields of the radial mode and the TE01 waveguide mode at the second harmonic frequency.

The equivalent electrical circuit for a second harmonic resonant disk oscillator is given in Fig. 3.2. Here the Gunn diode itself is represented as a capacitance C_G and a negative resistance $-R_G$, while package capacitance and bond wire inductance are modelled as C_P and L_B respectively. The capacitance C_D is associated with the resonant disk while the inductance L_P is that of the post. Generally speaking, the impedances of the bias post, disk and cavity are much greater than those associated with the packaged diode. The frequency of oscillation is therefore determined mainly by a combination of the resonant disk diameter, post width, and the length of the post between the resonant disk and the bottom of the lowest choke section. It is however noted that as frequency is increased, the impedance's related to the packaged Gunn diode becomes increasingly significant compared to those of the post, disk and cavity: it has been shown (through measurement and simulation) that a small, controlled change in bond ribbon profile can easily produce a frequency shift of around 800 MHz in a 77 GHz oscillator. In order to obtain maximum second harmonic power at the output, the dimensions and position of the radial disk must be optimised not only to obtain, in conjunction with the post geometry, a particular fundamental frequency resonance in the quasi-coaxial region, but also to maximise the coupling between the radial mode and the TE01 waveguide mode at the second harmonic frequency. This coupling is also dependent on the backshort position: it is noted that in practical oscillators, the coupling between the radial mode and waveguide mode is detuned (decoupled) from the optimum to reduce load pull effects. It is also noted that the fundamental frequency is below the cut-off of the rectangular waveguide and so is confined to the quasi-TEM region.

The Gunn diode operation and hot-electron injection, Gunn diode electromagnetic modelling, interaction between the diode and oscillator circuit and proposed modelling techniques are discussed below.

3.2.1 Gunn Diode Operation and Hot-Electron Injection

A brief description of Gunn diode and Gunn diode oscillator operation is included here as this is required to adequately explain the non-trivial nature of accurate oscillator simulation. The details including device physics are discussed in chapters 4 and 5. The Gunn diode can, at its most basic, be thought of as a DC-to-RF converter: when an applied bias voltage exceeds a certain threshold, oscillation will occur, the free-running frequency of which will depend on the material properties and the geometry of the device itself. This is due to the transferred electron effect exhibited by certain binary and ternary compound semiconductors.

As an electron is accelerated by an electric field through a transferred electron effect supporting material, it accumulates energy and so the probability of it being scattered (transferred) from the central conduction band valley to the nearest (in terms of energy and momentum) satellite valley increases. This probability increases dramatically when the electric field reaches a certain threshold value related to the distance in energy and momentum, between the conduction band’s central valley and the nearest satellite valley. The scattering mechanism is columbic in nature and involves a change in both momentum and energy and so the transfer process is extremely inefficient with large amounts of energy being lost to phonon excitation (and consequent elevation of the lattice temperature).

The transferred electron effect results in oscillation because the effective electron mass (related to the parabolicity of the conduction band profile) is greater in the satellite valley than in the central valley. This means electron velocity in the satellite valley due to an applied electric field is lower than that in the central valley. The effect of this is a ‘bunching’ of electrons as they travel along the length of the device, with those in the satellite valley moving at a slower rate than those in the central valley. This leads to a depleted region (of electrons) followed by a region of accumulation (known collectively as a high-field domain), which sets up an internal electric field opposing that applied externally. The effect of this is a continuing reduction in the net electric field across the device which continues until a certain threshold electric field is crossed (preventing the nucleation of any further high-field domains). At this point the high-field domain stops expanding and propagates at a constant velocity through the device until it reaches the anode contact layer at which point it collapses and the electric field through the device increases again. Oscillation is observed in the current and voltage at the device terminals as the domain forms at the cathode, expands, propagates and collapses at the anode, before another domain nucleates at the cathode.

The oscillation frequency and RF output power level are therefore fundamentally governed by a combination of the transit region length and carrier concentration: these define the high-field domain’s transit time through the diode, and the size (in the direction of the electric field gradient) of the high-field domain. However, the maximum useable frequency of a transferred electron device is generally limited by the inter conduction band energy relaxation time: the time constant governing the return of an electron from the satellite valley to the central valley.

The fundamental physics behind conventional Gunn device operation are therefore very much centred on electron energy, lattice temperature, and random scattering processes. These give rise to the following inherent limitations of conventional Gunn devices:

- The onset of oscillation (turn-on voltage) in a Gunn device varies greatly with ambient temperature.

- The oscillation frequency is highly dependent on temperature as it is defined (in part) by the length of the region in which the domain propagates (transit region). A small portion (referred to as the ‘dead zone’) of this region is required to accelerate electrons to the point at which they have sufficient energy to transfer to the satellite valley. The length of the dead zone, and therefore the effective transit region length and oscillating frequency are also dependent on temperature.

- The random nature of the scattering mechanisms which facilitate domain nucleation, lead to small variations in the point at which domain nucleation occurs. This effectively varies the length of the transit region from cycle-to-cycle leading to enhanced phase noise at the output.

In order to address these issues the use of a hot electron injection structure based on a graded gap AlGaAs launcher was proposed and demonstrated in the 1980's [12, 50, 51]. The reasoning behind this was to raise the electron energy sufficiently to greatly increase the probability of their direct entry to the conduction band satellite valley upon delivery to the transit region. The injected electrons have greater energy than those at equilibrium with the transit region lattice, and so are referred to as 'hot'. With the majority of the injected electrons directly entering the satellite valley, the dead-zone is effectively eliminated along with the temperature dependency of the oscillation frequency and turn-on voltage. In addition the overall conversion efficiency is increased (due to the reduced parasitic positive resistance) and because the random factors of domain nucleation are reduced, the phase noise is decreased.

3.2.2 Gunn Diode Electromagnetic Modelling

In order to accurately model the behaviour of a waveguide oscillator circuit, a full-wave, 3D high-frequency electromagnetic solver, such as Ansoft (ANSYS$^{®}$) High Frequency Structure Simulator (HFSS^{TM}), is required. To this end, numerous HFSS^{TM} models of different second harmonic resonant disk oscillators that correspond to the oscillators used to obtain measured results have been developed at e2v Technologies Plc. These are typically 3-port models with ports at the output waveguide, the top end of the choke (to evaluate filtering effectiveness at both fundamental and harmonic frequencies) and at the Gunn diode location. The Gunn diode port is, as in [52-54], set up as a coaxial transmission line (the effects of which are de-embedded post-process) to accurately represent the radial mode in the region of the diode and the resonant disk, and allow the impedance in the region of the diode to be evaluated.

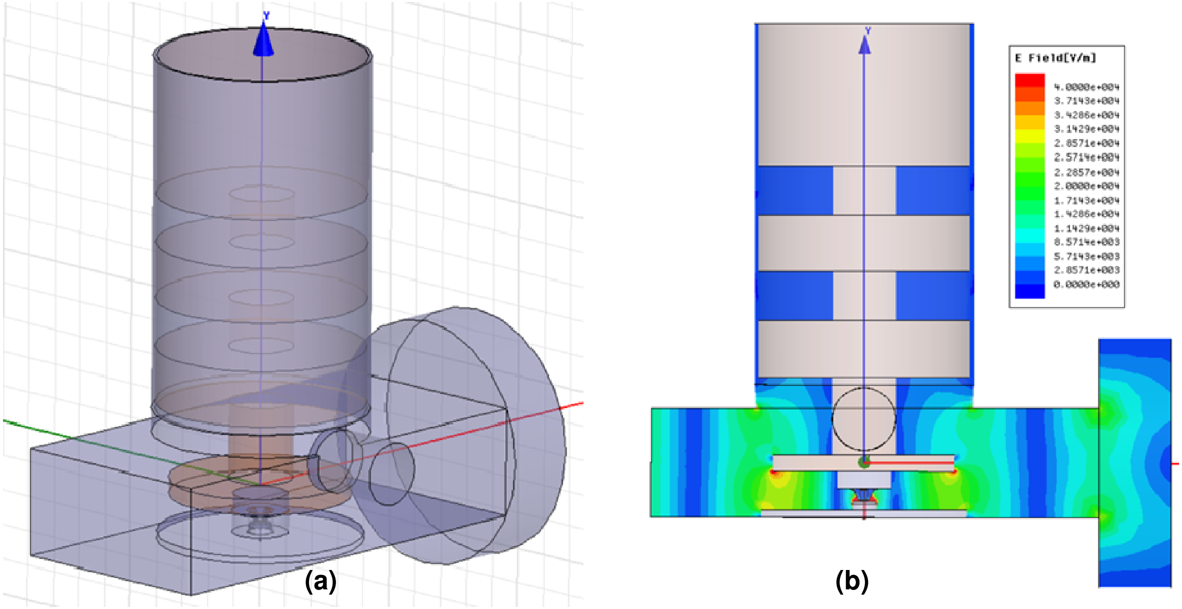

Fig. 3.3 (a) Ansoft HFSS™ model of a second harmonic resonant disk millimetre-wave oscillator with tuning pin and circular waveguide sliding backshort. (b) Simulated field electric field plot for the oscillator at second harmonic frequencies.

Fig. 3.3a shows an ANSYS® High Frequency Structure Simulator (HFSS™) model and electric field plot of a second harmonic resonant disk oscillator configuration using a circular waveguide contacting back short and frequency tuning pin. Although not showing the resonance in the quasi-coaxial TEM mode (the plot illustrates the electric field at second harmonic frequencies, not fundamental), Fig. 3.3b shows power being coupled between the diode and the waveguide output (left), and a degree of interaction between the resonant disk and the waveguide floor. For future work it is proposed to use these models to establish the diode embedding impedance at both fundamental and second harmonic frequencies. This will enable equivalent lumped element circuits for the fundamental and second harmonic resonators to be defined, which can then be coupled with the SILVACO™ model for subsequent time-domain simulations (chapter 9).

Oscillators were modelled and simulated at e2v to assess the performance of resonant disk Gunn diode oscillators (Fig. 3.4). It was believed that a reduced-height waveguide oscillator could be used to increase the output power obtained from the current D-band oscillators. An initial design was outlined and finalized for fabrication. Additionally, Quartz packages (Fig. 3.5b) were tested at e2v for use at frequencies above 125 GHz allowing increased power and frequencies than achieved with standard alumina packages (Fig. 3.5a). Power combining of two GaAs Gunn oscillators was achieved at 62.5 GHz with 210 mW output (Fig. 3.5c). That was intended for use as a high-power source for a frequency multiplier.

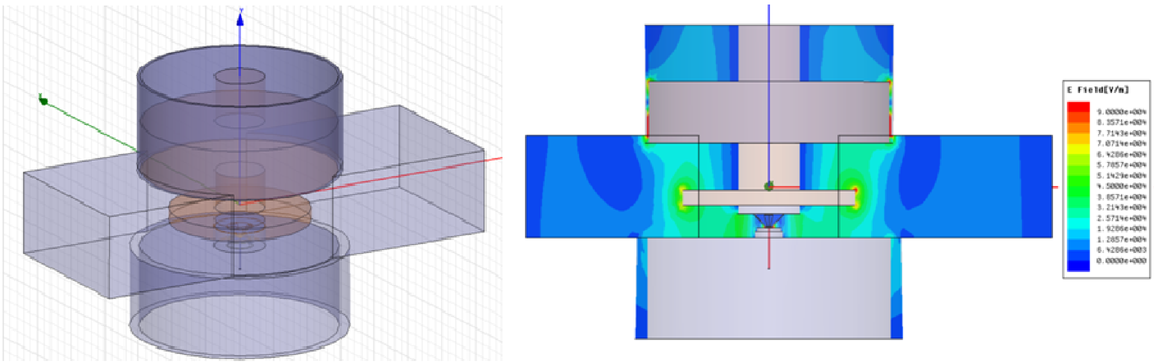

(a) **(b)**

Fig. 3.4 Ansoft HFSS^{TM} simulations of a reduced-height waveguide model developed at e2v (a) second harmonic resonant disk millimetre-wave oscillator (b) simulated field electric field plot.

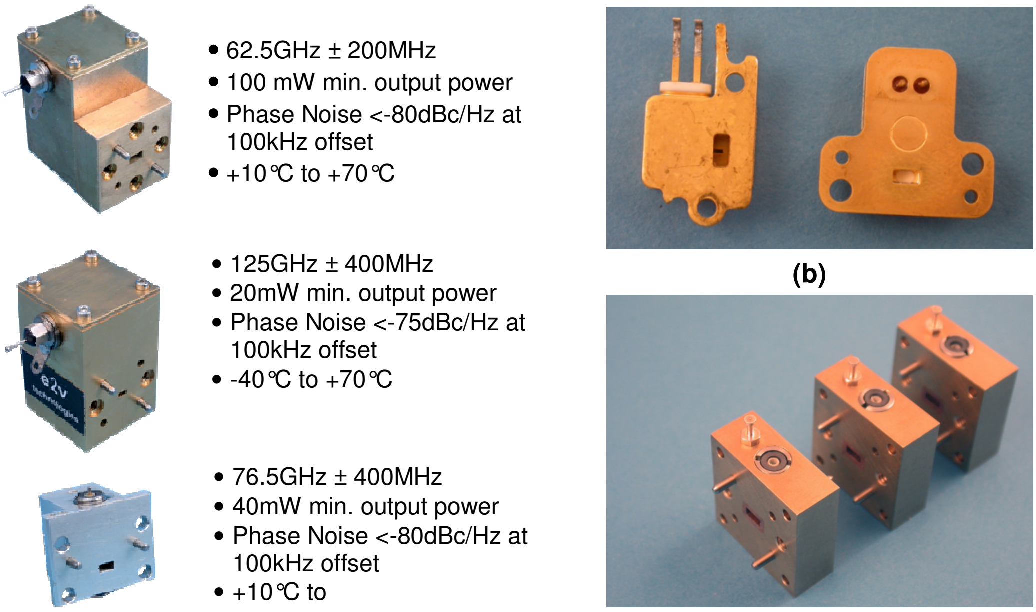

- 62.5GHz ± 200MHz
- 100 mW min. output power
- Phase Noise <-80dBc/Hz at 100kHz offset
- +10℃ to +70℃

- 125GHz ± 400MHz
- 20mW min. output power
- Phase Noise <-75dBc/Hz at 100kHz offset
- -40℃ to +70℃

- 76.5GHz ± 400MHz
- 40mW min. output power
- Phase Noise <-80dBc/Hz at 100kHz offset
- +10℃ to

(a) **(b)** **(c)**

Fig. 3.5 Gunn diode packages developed at e2v (a) Standard Alumni Packages DA810xx Bias-tuned Oscillators (b) Quartz Package.(c) Power Combining

3.2.3 Accounting for Interaction between the Diode and Oscillator Circuit

Previous modelling efforts have been concentrated on electromagnetic (EM) modelling of the oscillator using idealized approximations for the diode [12, 55-57]. Most advanced diode modelling work typically used either a hydrodynamic based approach [9, 57, 58] or Monte Carlo simulation techniques [59-61]. A novel approach is proposed here which will be the first time a semiconductor device modelling technique has been combined with an accurate 3D electromagnetic modelling tool to accurately compute the behaviour of a Gunn diode mounted in an oscillator.

Work has been reported where efforts have either been concentrated on EM modelling of the oscillator using idealised approximations for the diode, or concentrated on modelling the diode with approximations used for the oscillator circuit. Of the work reported on the EM modelling of second harmonic Gunn diode oscillators (mainly using HFSS^{TM}), either the impedance of the Gunn device is estimated as a static value [52], or a non-linear harmonic balance simulator has been used to estimate the reactance of the device mounted in an equivalent circuit [54]. Although the latter [54] attempts to incorporate the effects of the dynamic reactance of the device in the EM simulations, the device model used in the harmonic balance simulation was an idealised spice model (i.e. not a true semiconductor device modelling tool) as the research focussed mainly on the optimisation and behaviour of wideband tuneable Gunn oscillators rather than evaluating the performance of the Gunn device itself. However, the latter [54], represents the most accurate modelling technique yet demonstrated, predicting oscillation frequency to a few GHz and RF output power to within 20%.

The majority of the work that concentrated on modelling the diode itself, which typically used either a hydrodynamic based approach [57] or Monte Carlo simulation techniques [12, 55, 59-62], generally relies on estimated values for the parameters of an approximate equivalent oscillator circuit. These investigations centred on analysis of the behaviour and performance of the diode in isolation rather than in conjunction with an accurately modelled equivalent circuit: this is partly due to the difficulties in combining Monte Carlo simulation results with external circuit models due to the solution noise generated by the stochastic nature of the technique. The aim of the majority of previous work was to enable a study of domain formation and to compare the performance of different device variations, and not to enable accurate modelling of the Gunn diode and associated oscillator as a whole.

3.2.4 Proposed Modelling Techniques

The oscillator circuit effectively determines the oscillation frequency and so in turn affects both the dynamics of the high-field domain within the device's transit region and therefore the dynamic reactance of the device itself. Here, due to the cycle of domain nucleation, growth, propagation and collapse during each oscillation cycle, the device capacitance (itself partly dependent on the oscillator circuit parameters) varies throughout the oscillation cycle. It is therefore not accurate to simply extract a small-signal s-parameter model of the Gunn device from the SILVACO^{TM} model and use this in conjunction with the HFSS^{TM} model of the oscillator (i.e. terminate the diode port in the HFSS^{TM} simulation with a SILVACO^{TM} generated s-parameter matrix). This would not enable the effects of the oscillator circuit to be taken into account when computing a device's time-domain response.

As SILVACO^{TM} has the ability to include the effects of an external circuit on a simulated device through the definition of a lumped element circuit in which the device can be embedded, the effects of the external circuit can be considered during computation of device behaviour. The equivalent frequency-domain behaviour of a second harmonic oscillator circuit can therefore be simulated using HFSS^{TM} at the fundamental oscillation frequency and the equivalent circuit parameters at this frequency extracted: this can then be used to define a suitable circuit model for inclusion in the SILVACO^{TM} simulations. From simulation of the same HFSS^{TM} model at second harmonic frequencies, the values of the equivalent circuit elements at this frequency can be extracted and used in a lumped element equivalent circuit model to estimate the conversion efficiency to second harmonic. This will allow estimation of the second harmonic output power for a device mounted in the oscillator. This will ultimately enable the effects of both variations in the semiconductor device and the oscillator geometry to be evaluated simultaneously.

The HFSS^{TM} models for second harmonic resonant disk oscillators described in section 3.2 accurately represent the geometry and materials of the circuit including the package reactance values. The Gunn diode itself is currently modelled using conductive GaAs for the contact layers and launcher, and bulk semi-insulating GaAs (representing the depletion region in the high-field domain) for the transit region. From the resulting small-signal frequency-domain s-parameter file, all equivalent circuit element values (with the exception of the diode parameters C_G and $-R_G$) can be accurately extracted at both fundamental and second harmonic frequencies. It is noted here that modelling the whole transit region as dielectric (representing the depletion region of the high-field domain) is an approximation: in reality the depletion region does not fill the whole transit region, only a varying portion of it. The depletion region increases through the oscillation cycle as the high-field domain grows until, depending on the length and doping of the transit region, it reaches a constant value that traverses the length of then transit region, or (for short transit region devices) potentially continues to grow until it collapses at the anode. This will influence the shape of the fundamental frequency waveform and therefore its harmonic content meaning it will also affect the level of second harmonic power that can be extracted by the resonant disk circuit.

As the frequency of operation increases, not only do the impedances related to the packaged diode become increasingly significant in relation to those of the circuit, but in the shorter (sub-micron) transit region lengths the required mean spread in variation of device reactance over the oscillation cycle will also increase. This is due to a smaller percentage of the cycle time being devoted to the steady propagation of the high-field domain through the transit region (i.e. more of the cycle time will be consumed by domain formation and collapse as opposed to steady domain propagation through the device). It is currently thought that neglecting this variation when simulating the EM model will not significantly affect the behaviour of the EM model produced, so long as an accurate approximation of the diode structure is made. To achieve this, the micron-scale transit region will be modelled as a suitably conductive bulk GaAs material with an embedded insulating layer representing the high-field domain. The size and position of this layer, along with suitable material properties (permittivity and loss factor) can be estimated from an initial, free-running SILVACO^{TM} simulation.

As the dynamic nature of the depletion region is not negligible when simulating the EM behaviour of the oscillator circuit (leading to degradation in accuracy of the model as a whole) the growth of the high-field domain will need to be adequately represented within the EM model. A proposed technique to achieve this is to approximate the continuous process of domain growth and propagation in the HFSS^{TM} model by treating it as a sequence of discrete stages, each with an individual HFSS^{TM} model in which the length and/or the position of the dielectric region is altered. The size, position and material properties of the depletion region would again be estimated from an initial SILVACO^{TM} result. A time-varying series of equivalent circuit parameters could then be extracted, and using curve fitting, continuous functions approximated for each of the oscillator circuit spice model parameters. Although initially seeming labour intensive, this process could be simplified through exploitation of the parametric sweep functionality of HFSS^{TM}. Suitable code would then be written to update the values of the equivalent spice circuit model used to represent the oscillator circuit in the SILVACO^{TM} time-domain simulations, as the oscillation cycle progresses. This approach is proposed as future work while developing and designing high power THz sources using multipliers.

3.3 Frequency Multipliers

Multipliers were designed at e2v and several key doubler components (DC bias filter, output waveguide taper, and a broadband cross-waveguide coupler) were modelled for output at 140 GHz. The approach allowed verifying the design at relatively low frequency, before it could be scaled to higher frequencies.

The fabrication technique used for the multiplier split block waveguide circuit is dictated by the smallest feature size (typically the reduced height waveguide required for the broadband performance of the cross-waveguide coupler). Thin-film production of quartz circuits was routinely carried out at e2v on 127 µm substrates. It was thought that for prototyping and higher-frequencies, circuits using thinner substrates could be fabricated using standard semiconductor processing techniques.

The design methodology used to design multiplier is shown in Fig 3.6 and discussed below:

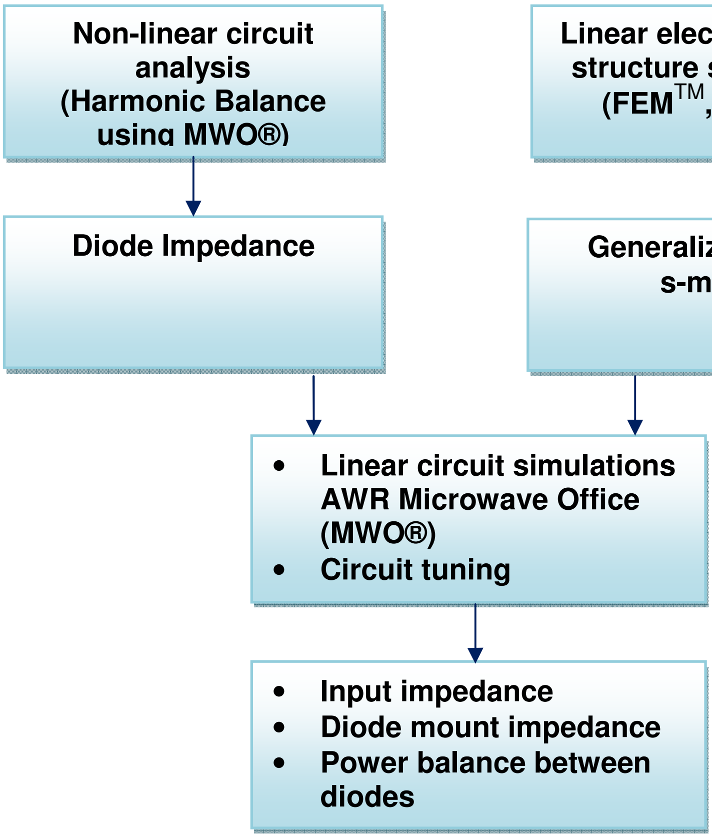

Fig. 3.6 Frequency multiplier design methodology developed at e2v showing both hydrodynamic and liner electromagnetic structure modelling.

- Based on the operational frequency and power requirements, a suitable diode or diode array geometry is identified. The diode size and number of anodes are determined.

- The diodes C-V, I-V and RF characteristics are measured. The SPICE parameters (series resistance, series current, built-in potential, ideality factor, and capacitance) are fitted to the measurements.

- Non-linear circuit analysis is performed using harmonic balance simulator tool such as Microwave Office ® by AWR. The harmonic balance simulator determines optimum diode embedding impedance, especially for resistive (real) impedance component. It calculates maximum theoretical conversion efficiency and power. It can be used to study the effects of chip parasitics on maximum theoretical efficiency.

- HFSS^{TM} is used to create a model of the diode chip and the waveguide circuit in which it is embedded. It enables impedance seen at the individual anodes to be evaluated.

- Simulation and tuning of entire multiplier circuit.

Millimetre-wave frequency multiplication using Schottky diode technology design methodology was extensively verified against published designs and data at e2v. The harmonic balance simulation tool, Linear EM Structure Simulations and Schottky diode Varactor are discussed;

3.3.1 Harmonic Balance Simulation Tool

A harmonic balance simulation tool was created using Microwave Office ® by AWR (Fig. 3.7), specifically for analysis and prediction of GaAs Schottky diode performance given device’s basic electrical characteristics. The extensive comparison to published work at e2v allowed accurate prediction of maximum conversion efficiency for a given device, under specified conditions. The tool is fully parametric and can be used to study the effects of operating conditions etc. on the final performance (Fig. 3.8), as well as calculating the optimum embedding impedances in the multiplier circuit. The results of the harmonic balance simulations can therefore be used along with electromagnetic simulators to design and tune circuit parameters for optimal circuit performance. Other circuit components such as input and output waveguide tapers, microstrip-to-waveguide coupling structures, and hammerhead bias filters have all been designed at e2v Technologies Plc. at frequencies up to 140 GHz.

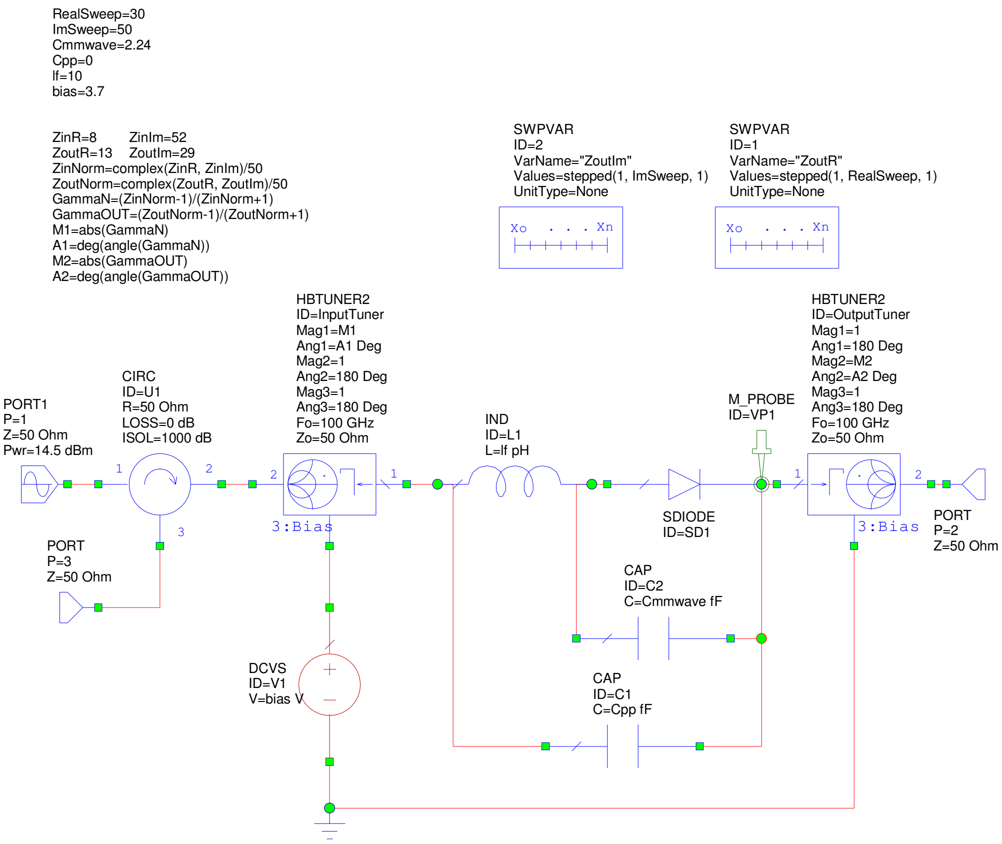

Fig. 3.7 A harmonic balance simulation tool schematics created using Microwave Office ® by AWR, specifically for analysis and prediction of GaAs Schottky diode performance given device's basic electrical characteristics.

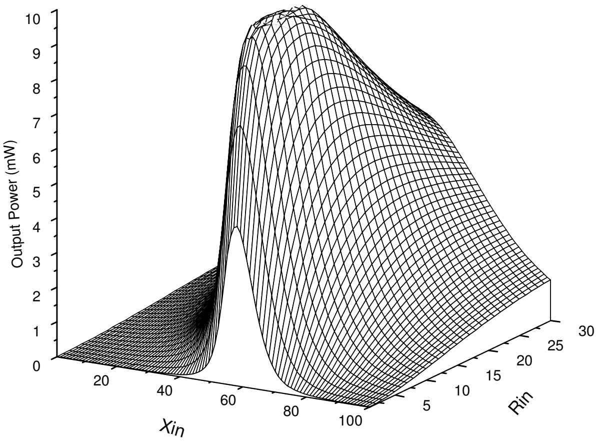

Fig. 3.8 Result of a harmonic balance parametric sweep to study output power with variation in input embedding impedance (with other operating conditions fixed) P_{IN} = 21 mW at 100 GHz, F_{OUT} = 200 GHz

3.3.2 Linear EM Structure Simulations

Other circuit components such as input and output waveguide tapers, microstrip-to-waveguide coupling structures, and hammerhead bias filters have all been designed at e2v Technologies Plc at frequencies up to 140 GHz. Initial designs outlining the geometry of Schottky diode arrays suitable for use in frequency doublers and triplers have been produced (Fig. 3.9).

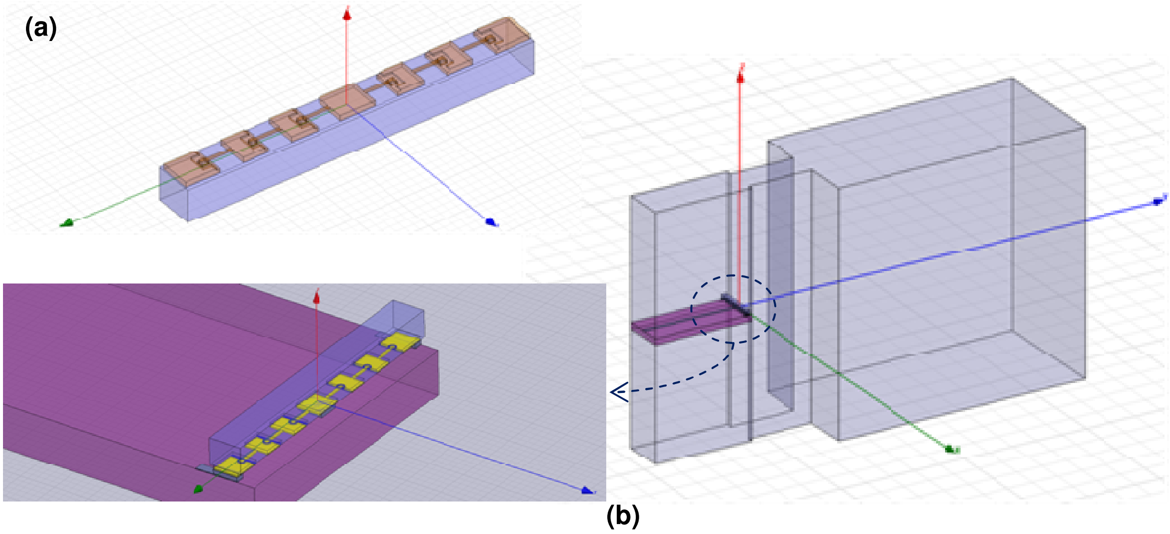

Fig. 3.9 (a) Varactor Diode Chip and the waveguide circuit model created using HFSS^{TM} at e2v Technologies Plc (b) HFSS^{TM} diode chip model embedded in waveguide diode mount.

HFSS^{TM} was used to create a model of the diode chip and the waveguide circuit in which it is embedded, which enables impedance seen at the individual anodes to be evaluated (Fig. 3.9a). Varactor Chip Waveguide Mount Modelling (Fig. 3.9b) shows diode chip model embedded in a waveguide diode mount.

3.3.3 Semiconductor Component – Schottky Diode Varactor

The harmonic oscillations of the input signal created in the multiplier are produced by a non-linear component, in this case a Schottky diode Varactor. In order to achieve a low RC time constant, both the capacitance and series resistance need to be kept as low as possible. In practice this is achieved by using small area anodes for the lowest possible capacitance, and although this does increase the series resistance, the overall effect is still to reduce the RC time constant in properly designed structures. The challenge is then to reduce the series resistance as much as possible for a specific Schottky contact.

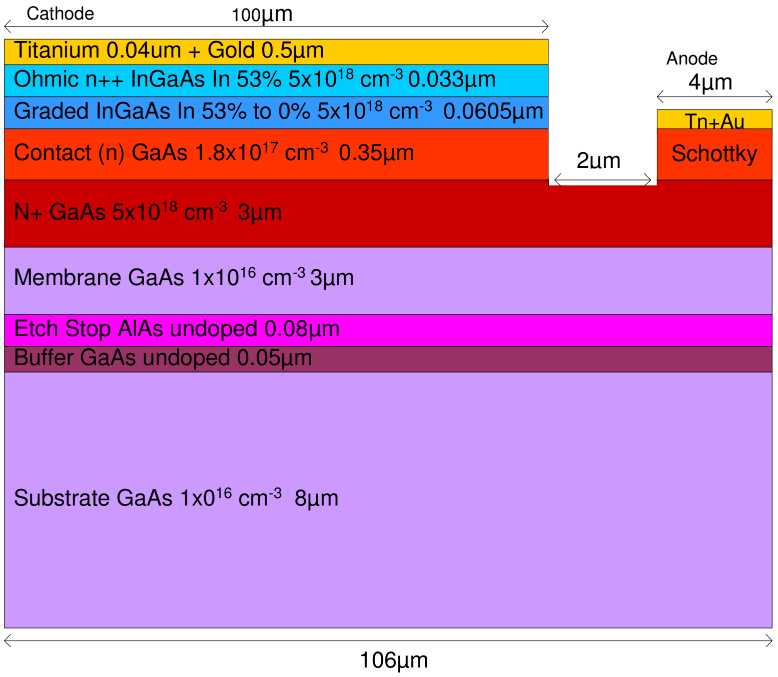

Fig. 3.10 2D GaAs diode structure topped by a heavily doped region of $In_xGa_{1-x}As$ graded from x=0 at the GaAs interface to x=0.53 at the upper surface.

The device structure shown in Fig. 3.10 consists of a traditional GaAs diode structure topped by a heavily doped region of $In_xGa_{1-x}As$ graded from x=0 at the GaAs interface to x=0.53 at the upper surface. A subsequent heavily doped layer was grown to form the low resistance non-alloyed Ti/Au Ohmic contact. The fabrication process was such that the metallisation layer used to form the Ohmic contact was also utilised to provide the Schottky contact, after the appropriate patterned wet recess etch though the InGaAs layers to the GaAs. A methane/hydrogen RIE (Reactive Ion Etching) step was then used to etch through the lightly doped GaAs layer to the highly doped conductive region below (conventionally the Ohmic contact layer with alloyed contacts). Importantly the contact metals are used as an etch mask. An air bridge (2 µm wide) was then formed between the anode and a bond pad to complete the device.

Developing such a device, the doping and thickness of the GaAs layer beneath the anode becomes critically important in reducing the series resistance. Carriers have to pass through the undepleted region of this layer to the highly doped GaAs region as in a conventional Schottky, but then back through this lightly doped region to the InGaAs contact layer. Calculating the exact value of the depletion region at breakdown is therefore of importance in reducing the series resistance. Increasing the doping in this region reduces the resistivity of the material and the thickness of material required (reduced depletion width) further reducing the series resistance. Unfortunately the breakdown voltage is also reduced. However, using the anodic metal as a mask in the RIE means that the maximum breakdown voltage is achieved by increasing uniformity of current density under the anode. Effective balancing of these parameters provides optimum device performance. Shown below (Fig. 3.11a) is the C-V plot for a 4 μm device obtained by extracting the S11 parameter from RF testing and fitting the data to an ADS^{TM} simulation at each bias point with constant values of inductor, resister and co-planar waveguide elements in the simulation.

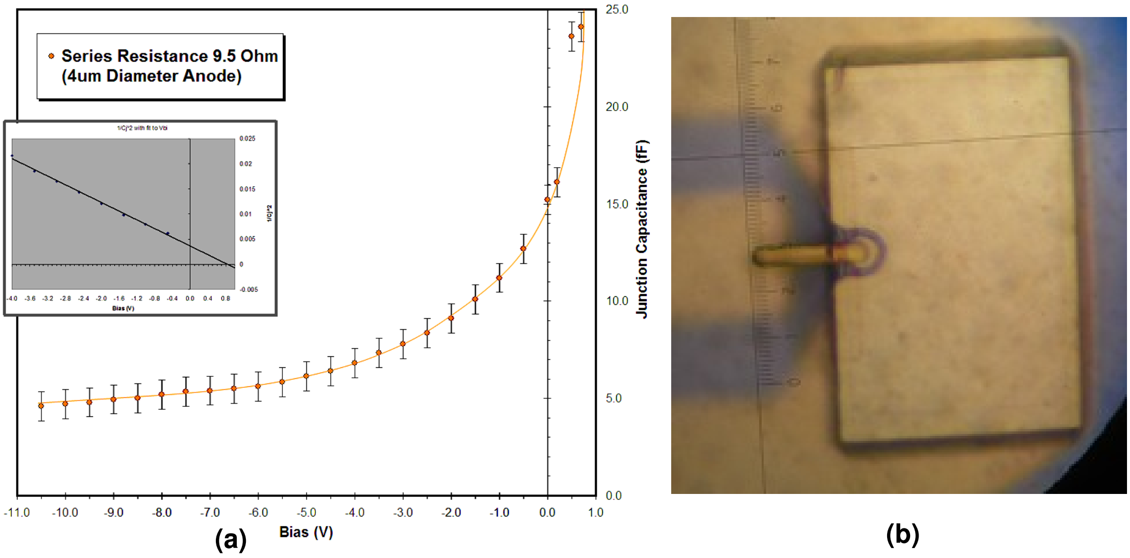

(a) (b)

Fig. 3.11 (a) C-V plot of 4 μm Schottky device. Junction capacitance of fabricated single anode device (bias - 1/C_{j0}^2 inset) (b) image of a 4 μm Schottky device with 2 μm bridge to the anode.

These small area Schottky diodes were fabricated and improved over several iterations to give a reduced RC time constant producing a cut-off frequency approaching 900 GHz (thus operation up to ~300 GHz). The design was developed to utilise a non-alloyed self aligned contacts structure with the smallest anode diameter of 4 μm and a thin 2 μm contacting air-bridge (see Fig.

3.11b). It produced low contact resistance and capacitance with a still relatively high breakdown voltage. That material was decided to be used to fabricate smaller anode devices for reduced RC time constant and higher frequency operation.

At the University of Manchester new process techniques were developed for undercut air bridges to reduce device parasitics, process complexity and series resistance. Yield and uniformity was increased in order to repeatedly deliver the more complicated multiple device anti-series structures required and thick (> 2.5 µm) lift-off processes were developed. Those processes allowed the design of new devices in collaboration with multiplier design requirements across a wide range of chip size and device combination totalling over 700 individual device structures (such as Fig. 3.12). Junction capacitance was extracted from RF testing indicating 4.8 fF at breakdown (Fig. 3.11). These devices gave a theoretical cut-off frequency in excess of 1.1 THz.

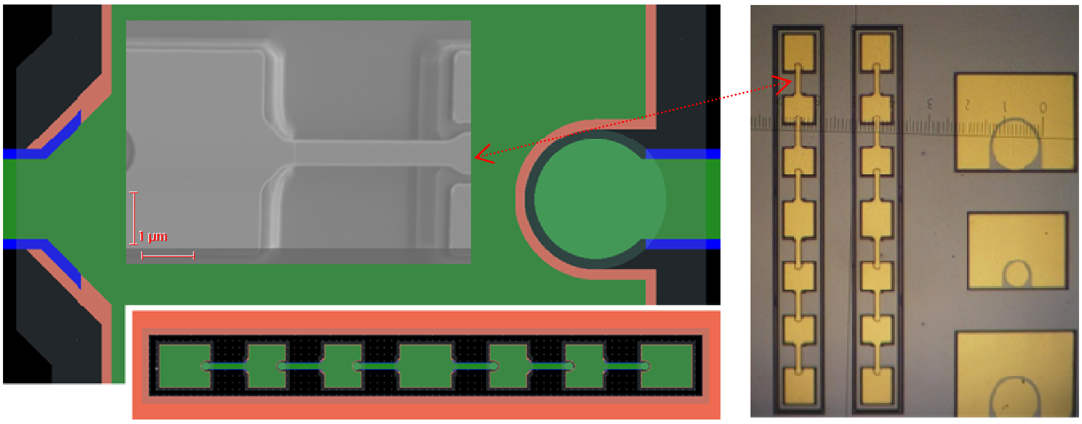

(a) (b)

Fig. 3.12 Six anode anti-series device single anode (full circuit inset) (a) design (b) fabricated device.

3.4 Schottky Diode SILVACO^{TM} Modelling

A Schottky diode 2D model has been developed in SILVACO^{TM}. Its epitaxial structure is shown in Fig. 3.13. The conduction band diagram of both ohmic and Schottky contacts are shown in Fig. 3.13b and 3.13c. The models and material parameters are given in Appendix 2.

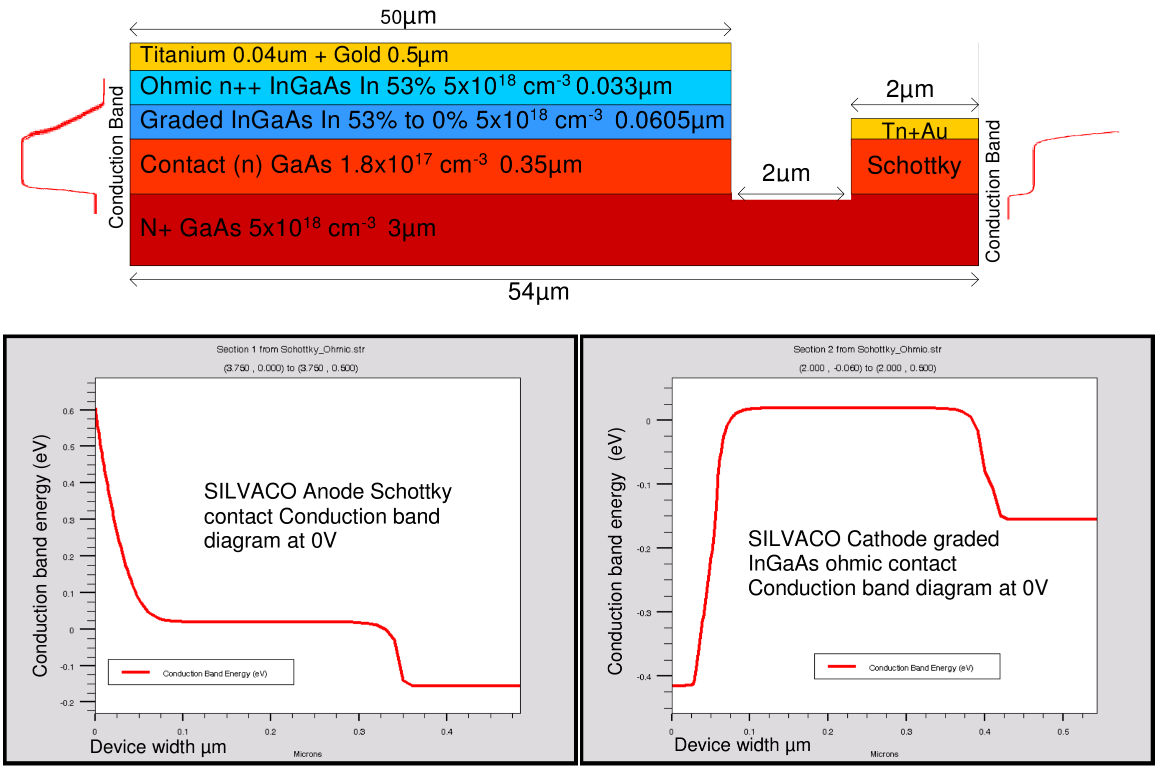

Fig. 3.13 **GaAs Schottky diode SILVACO™ 2D model. Equal area rule was maintained same as the manufactured device (a) 2D device structure for a 4 μm diameter anode Schottky diode (b) Conduction band diagram for GaAs Schottky contact (c). Conduction band diagram at zero bias showing graded InGaAs ohmic contacts**

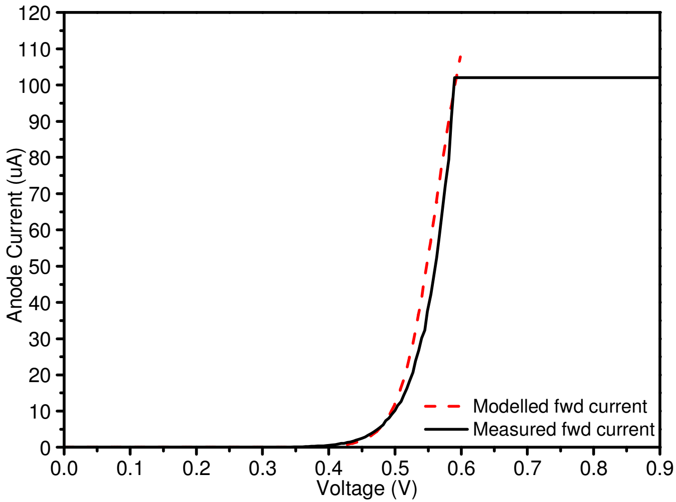

Fig. 3.14 **Forward bias I-V curve for a 4 μm diameter anode Schottky diode. Series resistance R_s was calculated from curve's slope.**

The modelled versus measured results matched very well (Fig 3.14 - 3.16). The Schottky contact breakdown voltage analysis is shown in Fig. 3.14. The model gives a series resistance of 6 Ohms, substantially less than the measured value of 9.5 Ohms. This is attributed to external device resistances and modelled device rectangular geometry. The model can be used to study underlying device physics and extract parameters such as ideality factor, zero voltage junction capacitance, built in voltage and breakdown voltage. These parameters will be used in harmonic balance simulations created using Microwave Office ® by AWR, which will allow analysing and prediction of the GaAs Schottky diode performance at mm-wave frequencies.

The modelled Schottky diode capacitance-voltage (C-V) plot matched very well with measured data (Fig. 3.15). The junction capacitance indicated 4.6 fF at breakdown and a C_{jo} of ~17 fF giving a theoretical cut-off frequency in excess of 1.1 THz.

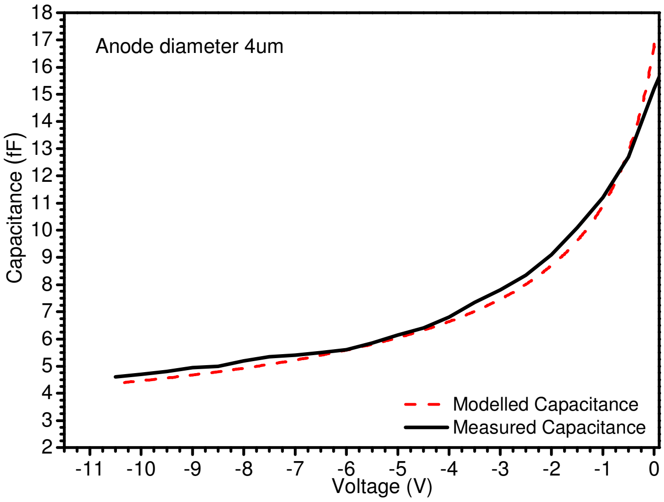

Fig. 3.15 **C-V plot for a 4 μm diameter anode Schottky diode**

Three Schottky models listed in table 3.1 were developed and compared with measured results (Fig. 3.16). They were designed in collaboration with multiplier design requirements for ~120 GHz output. An additional area was included in modelled devices that were in line with fabricated devices. The C-V plots were compared with measured results and junction capacitance C_{j0} was determined. The cut-off frequencies were calculated as shown in table 3.1

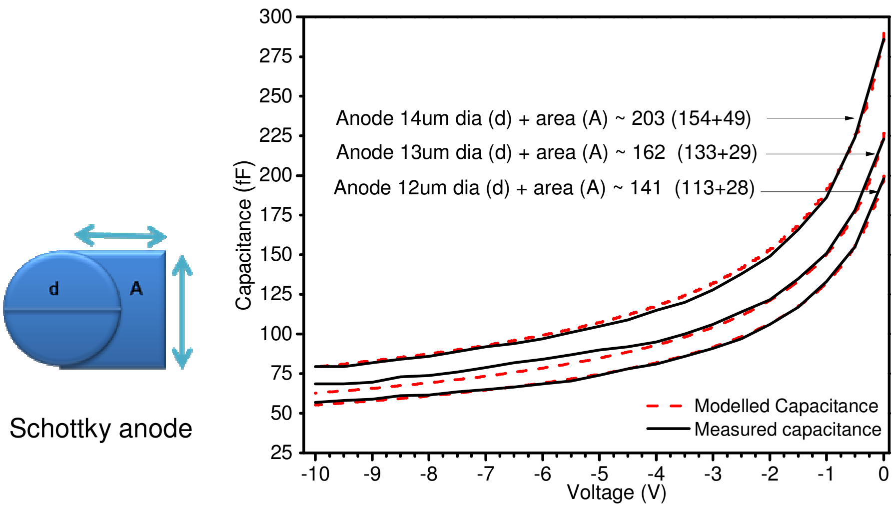

Fig. 3.16 **Schottky diode C-V plots for 14 µm, 13 µm and 12 µm anode diameters.**

Parameters	**Schottky anode diameter (d)**		
	14µm	13µm	12µm
Anode area calculated using $d = \frac{\pi d^2}{4}$ **in** um^2	154	133	113
Anode additional area (A) added in SILVACO^{TM} **model, which is due to processing in** um^2	49	29	28
Total Area (d+A) in um^2	203	162	141
Capacitance (C_{j0}**) obtained from C-V plot in** fF	286	223	198
Cut off frequency $f_c = \frac{1}{2\pi R_s C_{j_0}}$ **in** GHz **with** $R_s = 0.9\Omega$	**618**	**793**	**893**

Table 3.1 Schottky diode models with 14µm, 13µm and 12µm anode diameters showing an additional area and calculated cut off frequencies.

3.5 Conclusion

The Gunn diode operation and hot-electron injection, Gunn diode electromagnetic modelling, interaction between the diode and oscillator circuit and proposed modelling techniques were discussed. Two novel modelling techniques to merge SILVACO^{TM} and HFSS^{TM} models and to account for interaction between the Gunn diode and oscillator circuit were presented. The techniques include the lumped element model for SILVACO^{TM} and taking into account Gunn diode domain growth and propagation in the HFSS^{TM} model

Multipliers designed at e2v and several key doubler components (DC bias filter, output waveguide taper, and a broadband cross-waveguide coupler) modelled for output at 140 GHz have been presented in detail. Oscillator cavity developed in HFSS^{TM} and harmonic balance simulation tool created in Microwave Office ® by AWR at e2v Technologies Plc. were discussed. The harmonic balance simulation tool, Linear EM Structure Simulations and Schottky diode Varactor were presented.

Both semiconductor components of the multiplier namely the Gunn diode and the Schottky diode have been presented. It was shown that the modelled Schottky diode C-V plot matched very well with measured data. The junction capacitance indicated 4.6 fF at breakdown and a C_{jo} of ~17 fF giving a theoretical cut-off frequency in excess of 1.1 THz. Additionally, three Schottky models, designed in collaboration with multiplier design requirements for ~120 GHz output, were also compared with measured results. An additional area was included in modelled devices that were in line with fabricated devices. The C-V plots were compared with measured results and junction capacitance C_{j0} was determined. The cut-off frequencies were shown.

Chapter 4 Gunn Diode Theory

4.1 Introduction

The Gunn Diode, named after J. B. Gunn, who discovered the Gunn Effect, is an active solid state two terminal device, classed as Transferred Electron Device (TED). The most conspicuous feature of the device is the negative differential resistance, which depends on the bulk material properties [28]. In this chapter after covering the basic Gunn diode theory, the negative differential resistance phenomenon will be analyzed with relation to material band structure. Finally the various device operating modes will be discussed with emphasis on the high frequency oscillations before summarizing the limitations of conventional Gunn diodes.

4.2 Gunn Diode as Transferred Electron Effect (TED) Device

The Gunn diode can, at its most basic, be thought of as a DC-to-RF converter: when an applied bias voltage exceeds a certain threshold, voltage oscillation will occur, the free-running frequency of which will depend on the material properties and the geometry of the device itself. This is due to the transferred electron effect exhibited by certain binary and ternary compound semiconductors. The transferred electron effect is reviewed in detail through Electric Field Effects on Electron Drift Velocity, High Field Transport in n-GaAs, Negative Differential Resistance (NDR) and Conditions for Negative Differential Mobility.

4.2.1 Electric Field Effects on Electron Drift Velocity

At low electric-fields the electron drift velocity is linearly proportional to the applied electric field. However, it departs from the linear relationship with the increase in applied electric-field, which causes the drift velocity to approach the thermal velocity value. Before considering the high electric field effects the following gives a brief account covering the essentials of low field electron drift velocity and its corresponding high field effects [3].

The low field electron drift velocity is given as:

$$v_n = -\left(q\tau_c / m_n \right)\varepsilon \quad cm/s \qquad (4.1)$$

where v_n is electron drift velocity, ε is the applied electric field, τ_c is the mean free time and m_n is the effective electron mass. The drift velocity is proportional to the electric field and the proportionality factor is known as the mobility, which is given by:

$$u_n = \frac{q\tau_c}{m_n} \qquad (4.2)$$

Thus the drift velocity can be written as:

$$v_n = -u_n\varepsilon \qquad (4.3)$$

where the negative sign indicates that the electrons move in the opposite direction to the applied electric field. The mobility determines the influence of electric field on the motion of an electron. At low electric-field values the drift velocity of electrons is linearly proportional to the applied electric field and is smaller than the thermal carrier velocity (which is $7.7 \times 10^6 cm/s$ [1] for n-type GaAs). As the electron drift velocity approaches the thermal velocity, the linear relationship due to the corresponding constant mobility breaks down. The drift velocity increases with the increase in electric field until reaching a saturation velocity value. The plots of carrier drift velocity versus electric field for Gallium Arsenide (GaAs), Indium Phosphide (InP) and Gallium Nitride (GaN) are shown in Fig. 4.1, where it can be seen that the drift velocity after reaching a maximum value decreases with an increase in applied field.

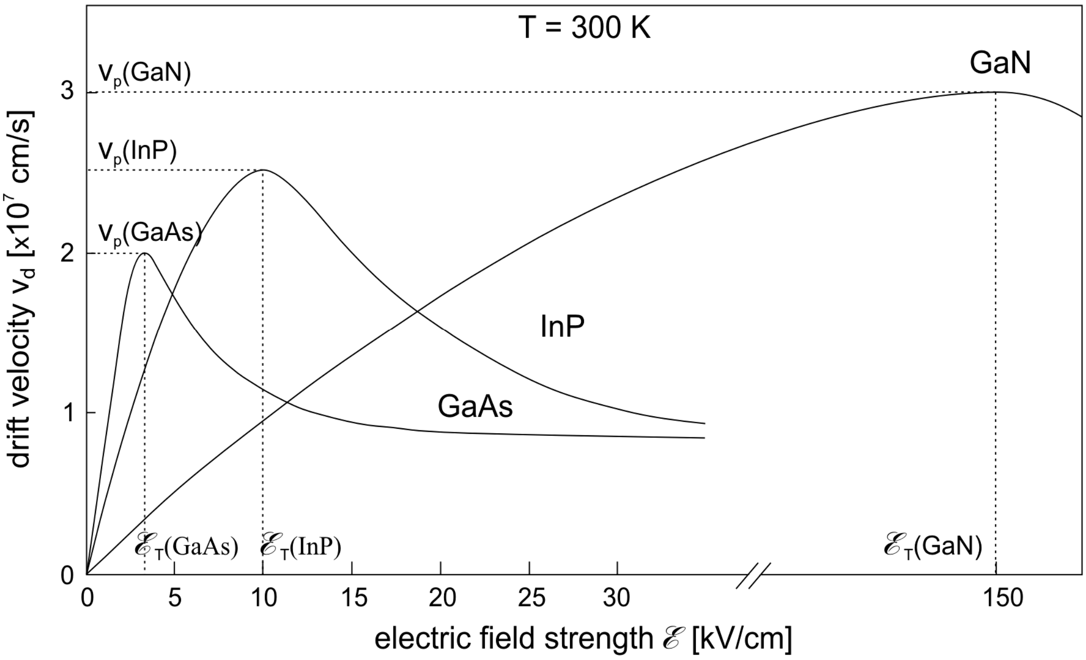

Fig. 4.1 **Carrier Drift Velocity verses Electric Field graph [1]**

Note that the threshold field at which NDR occurs for GaN is very high implying large voltages for operation (about 50 times larger than those of GaAs).

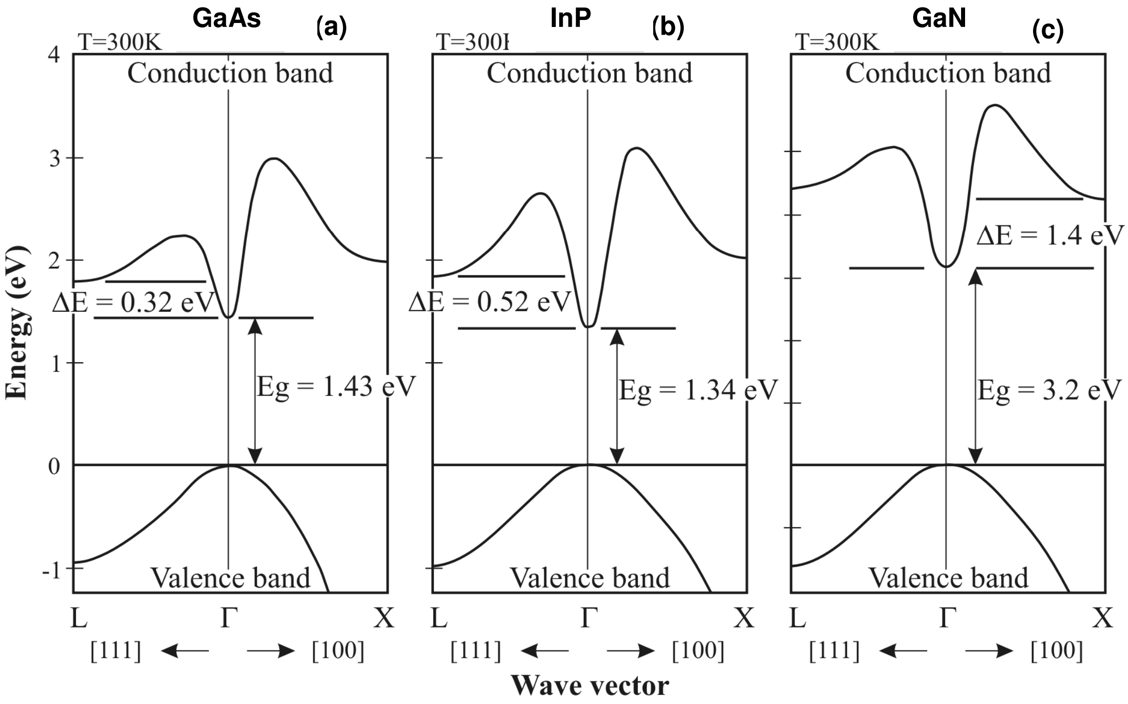

Fig. 4.2 **Electron occupations for (a) GaAs, (b) InP and (c) GaN [3]**

4.2.2 High Field Transport in n-GaAs

The negative differential mobility phenomenon can be explained through consideration of the band diagrams shown in Fig. 4.2. Fig. 4.2a shows that GaAs is a direct band gap material with an energy gap, between the top of valence band and bottom of conduction band, of 1.43 eV at *k*=0 (zero wave vector). The satellite conduction band minimum (L) is 0.32 eV higher than the conduction band minimum (Γ) and is at $k = \pm 2\pi / a$ (where *a* is the lattice constant). At 300K, n-type GaAs has its valence band highly occupied with few electrons in the conduction minimum (central Γ band) and nil in the satellite L band. However, as the increase in applied electric field reaches ~3kV/cm, some electrons from the Γ valley gain sufficient energy and are scattered into the L valley.

As shown by equation 4.2, electron mobility is dependent on effective electron mass, which is different in the different conduction band valleys and depends on the local curvature of the band structure. The effective electron mass is given by [29]:

$$m^* = \frac{1}{\frac{1}{2\hbar^2}\left[\frac{\partial^2 E}{\partial k^2}\right]} \quad \text{..(4.4)}$$

Where m^* is the effective mass, $\hbar = h/2\pi$ is planks constant and *k* is the wave vector. In the satellite valley the curvature is higher than the central valley, which results in a higher effective mass compared to the central Γ valley. For GaAs, electrons have an effective mass of $0.4m_0\,(m_1{}^*)$ in the L valley and $0.068m_0$ $(m_2{}^*)$ in the Γ valley [2].

The density of states of each Γ and L valley represent a number which is proportional to energy interval available to the conduction electrons and number of allowed energy states per unit volume. Its ratio, R, is given by:

$$R = \frac{M_2}{M_1}\left(\frac{m_2{}^*}{m_1{}^*}\right)^{\frac{3}{2}} \quad \text{..(4.5)}$$

Where M_1 and M_2 are the equivalent Γ and L valley whose values for GaAs are 1 and 4 respectively [34]. Thus the density of states ratio becomes R=94 [34, 63], which is much higher than the corresponding Γ valley. In the L valley in addition to the higher electron effective mass, the electrons are also subjected to stronger scattering processes [64]. These effects collectively result in lower electron mobility (up to 70 times) in the L valley compared to the Γ valley.

4.2.3 Negative Differential Resistance (NDR)

In Fig. 4.3a applied electric-field is low ($\varepsilon < \varepsilon_a$) thus all the electrons are in the central valley. As the field is increased ($\varepsilon_a < \varepsilon < \varepsilon_b$) some electrons gain the energy required to transfer to upper valley as shown in Fig. 4.3b. Finally when the field is large enough ($\varepsilon > \varepsilon_b$) effectively all the electrons are transferred to the upper valley. The effect of this on the drift velocity is shown in Fig. 4.4, which can be equated as [3]:

$$v_n \cong u_1\varepsilon \text{ when } 0 < \varepsilon < \varepsilon_a \quad \ldots\ldots(4.6)$$

$$v_n \cong u_2\varepsilon \text{ when } \varepsilon > \varepsilon_b \quad \ldots\ldots(4.7)$$

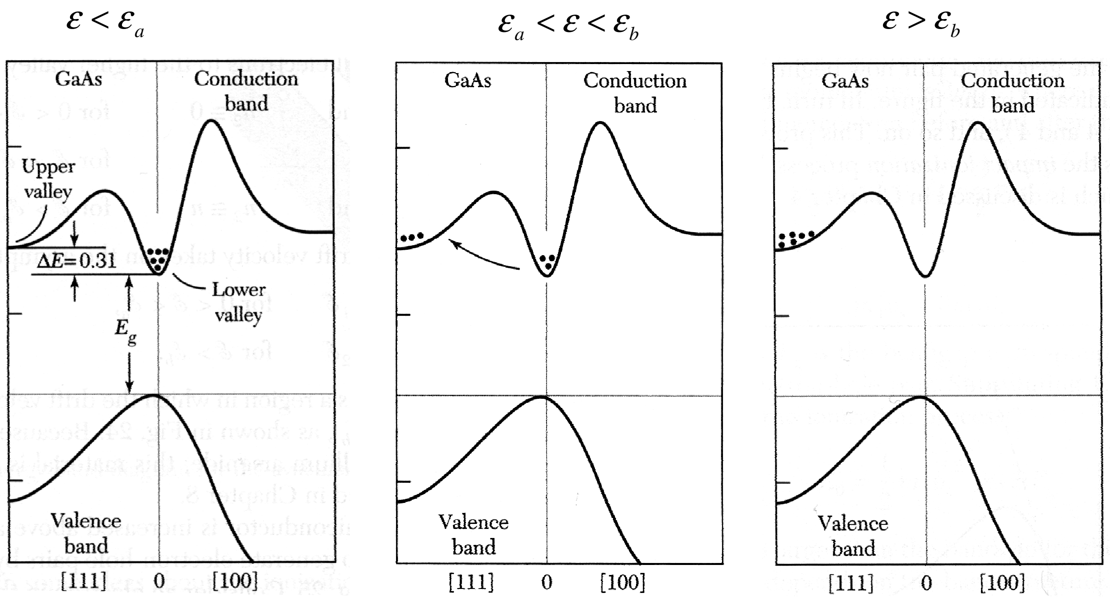

(a) (b) (c)

Fig. 4.3 **Electron occupations under various Electric Field levels for n-GaAs [3]**

The electron drift velocity increases linearly until the onset of negative differential resistance where the electric filed value is given as ε_a. The drift velocity continues to decrease until the field acquires the maximum value ε_b as shown in Fig. 4.4.

It can be seen from Fig. 4.4 that $u_1\varepsilon_a$ is greater than $u_1\varepsilon_b$, which results in a decrease of drift velocity between ε_a and ε_b, The NDR exists between the threshold field (ε_T) and final valley field (ε_V) as shown in Fig. 4.4 [1, 3].

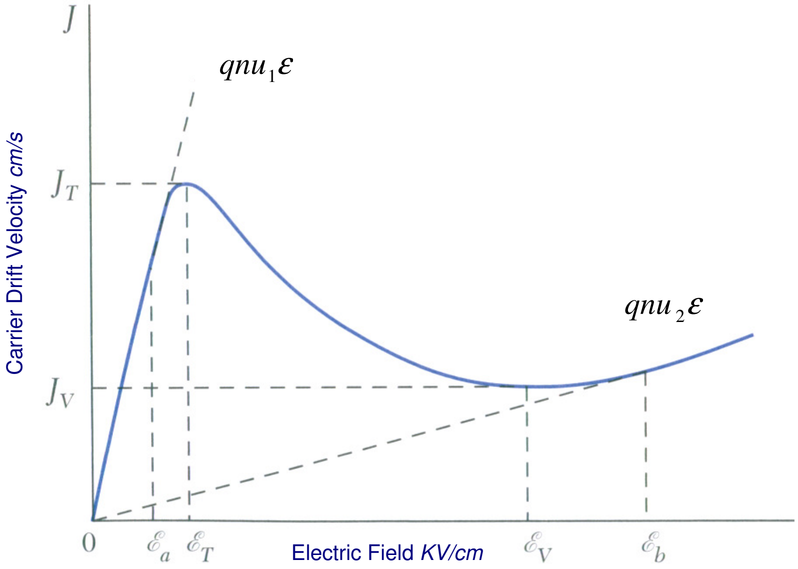

Fig. 4.4 **Negative Differential Resistance region [3]**

If the electron mobility, effective mass and density for both central (Γ band) and satellite (L band) valleys are denoted by u_1, m_1, n_1 and u_2, m_2, n_2 respectively then the steady state conductivity of n-type GaAs is given as [3]:

$$\sigma = q(u_1 n_1 + u_2 n_2) = qn\bar{u} \quad \text{……………………………………..…………(4.8)}$$

Where $\bar{u}$ is the average mobility and is given by:

$$\bar{u} = \frac{(u_1 n_1 + u_2 n_2)}{(n_1 + n_2)} \quad \text{………………………………………………………(4.9)}$$

Thus the average drift velocity can be written as:

$$v_n = \bar{u}\varepsilon \quad \text{...(4.10)}$$

4.2.4 Conditions for Negative Differential Mobility

For a material to exhibit the transferred electron effect and therefore negative differential mobility, it must display the following characteristics [65]:

- The material satellite or L band energy minimum is above the normal conduction band (Γ) minimum.
- The *E* verses *k* curvature for L band is less than the Γ band minimum, thereby providing greater effective mass values.
- The density of states in L band has a higher value than the Γ conduction band.
- The energy gap between Γ and L valley must be greater than kT to avoid occupation of L valley due to thermal occupations at low electric field: This ensures that the occupation of L band is due to the applied electric-field.
- The fundamental energy gap, E_g, must be greater than ΔE to avoid impact ionization of electrons across E_g before inter-valley transfer occurs.
- Some mechanism must be present to supply the k-value (momentum) change required for transition to the satellite valley.

Besides GaAs materials such as InP and GaN depict the above characteristics and thus are the favoured materials choices for the implementation of Transferred Electron Devices (TED) [1, 3, 66].

4.3 Instability and Domain Formation

Semiconductors such as GaAs and InP, which exhibit the Transferred Electron Effect are inherently unstable. The instability is due to the formation of a space charge region that grows exponentially with time due to a small, random change in carrier density in the semiconductor. This instability has been explained in [2], and is discussed below:

In a uniformly doped semiconductor device with an electron concentration N_D, a noise process or variation of doping level or some crystal defects can cause a spontaneous fluctuation in the electron density (N). This spontaneous fluctuation forms a dipole, consisting of an accumulation and a depletion region with associated electric field gradient. The non-uniformity in the space charge is related to the electric field by the following Poisson equation:

$$q(N - N_D) = \varepsilon_0 \varepsilon_r \frac{\partial \varepsilon}{\partial x} \quad \text{...(4.11)}$$

where ε_0 and ε_r are the vacuum and relative permittivity respectively, and N_D is the doping density. If the mean electric field is less than the threshold field then electrons subjected to a higher electric field will move faster than those in the low-field region. The space charge would then fill the depletion region resulting in the dampening of the fluctuation due to dielectric relaxation.

Now considering the case when the applied electric field is greater than the threshold electric field ε_T: the electron drift velocity reduces in the region of higher field, causing the space charge fluctuation to grow along with time associated local electric field in the region as shown in Fig. 4.5b. This exponential growth of electric field continues until a stable domain is formed as shown in Fig. 4.5c. Stability arises because to keep the total voltage drop across the device the same, the electric field outside the domain remains below the threshold level. It can be seen in Fig. 4.5c that the electric field within the domain reaches a peak value ε_P, while outside the domain the electric field (ε_R) is less than the threshold value. ε_R is therefore less than ε_T removing the drift velocity difference (which causes the space charge to grow) and a stable domain is formed. Additionally this means that when the domain is stable another domain does not grow as ε_R remains below ε_T.

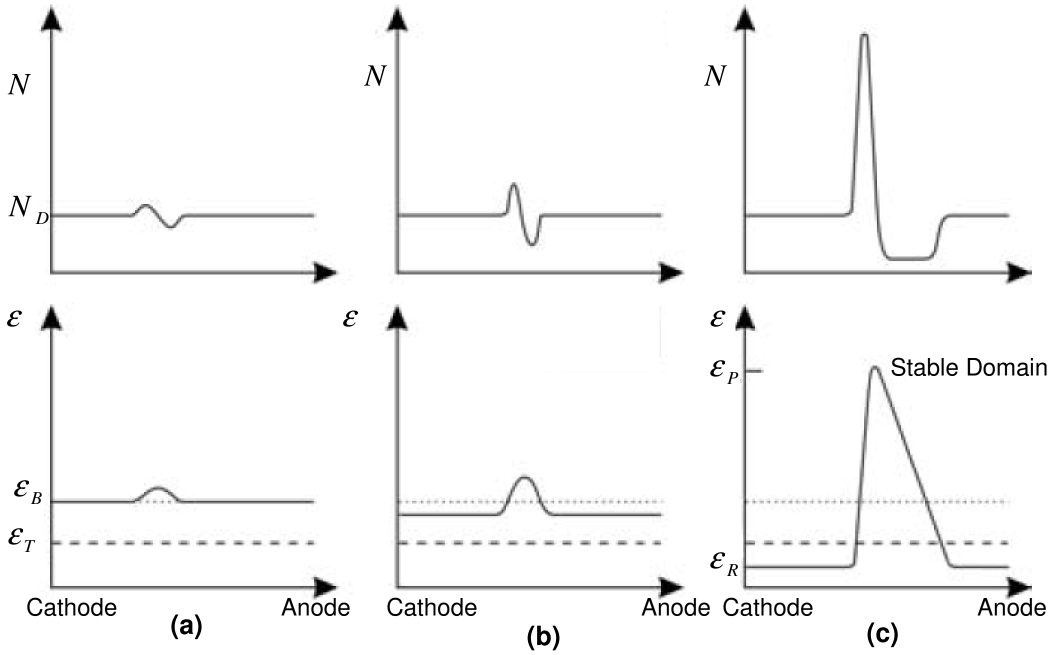

Fig. 4.5 **Stable dipole domain formation with the growth of space-charge [2]**

4.3.1 Domain Dynamics

Once stable, the domain drifts through the device at a constant velocity. The electric field is less than the threshold level outside the domain. The electric field is at its peak at the outside edge of the accumulation region, where it is above the threshold value. It drops across the domain until it becomes less than the threshold field (at the outer edge of the depletion region). Butcher [58] has done a detailed analysis of domain formation, which concluded that if the diffusion parameter *D* is assumed constant and independent of electric field, then the electron velocity outside domain, v_R, is the same as the domain drift velocity, v_D. Secondly ε_P and v_R are related by the dynamic characteristic. The dynamic characteristic curve is related to velocity electric field ($v-\varepsilon$) curve by equal area rule shown in Fig. 4.6 [1]. Using these results Hobson explained the current conduction process within the domain as [2]:

$$J = qNv_R(\varepsilon) + \varepsilon_0\varepsilon_r \frac{\partial \varepsilon}{\partial t} - qD\frac{\partial N}{\partial x} \quad \text{...(4.12)}$$

where, the current density *J* is constant throughout the device, and the three terms represent, drift, displacement and diffusion components respectively. Outside the domain both N and ε are independent of position thus the current is carried as conduction current and current density is due to the drift component $qNv_R(\varepsilon)$. Within the domain all three components play roles due to the gradient in both doping density (N) and ε. The change in electric field gradient causes a displacement current to flow. At the peak electric field, ε_P, value no displacement current flows because $\partial\varepsilon/\partial x = 0$. However, at ε_P an electron density gradient causes a diffusion current to flow. Thus in the depletion region, the current is due to the displacement current while in the accumulation region the current is due to the large conduction (drift) current, which is opposed by the displacement and diffusion currents [4].

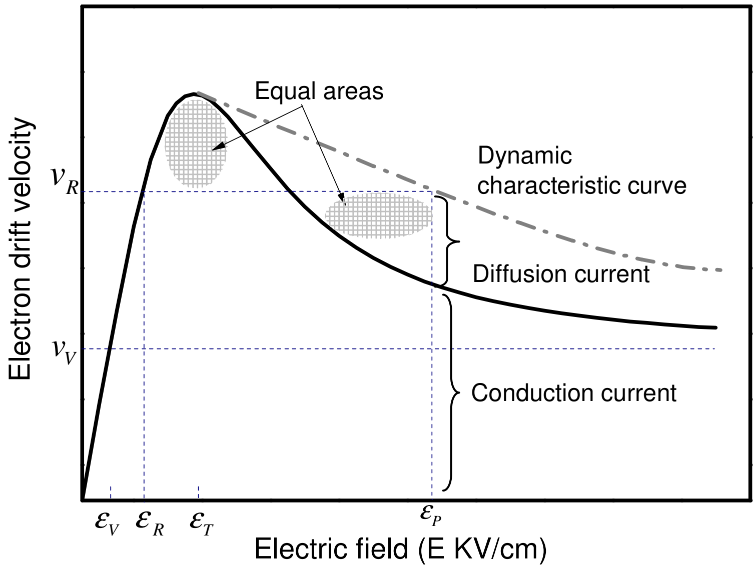

Fig. 4.6 Dynamic characteristics curve and electron drift velocity – electric field curve. It is plotted in SILVACO using MOCASIM (Monte Carlo simulator) for GaAs $1.1\text{x}10^{-16}$ doped. Equal area relationship between ε_P and v_R is shown.

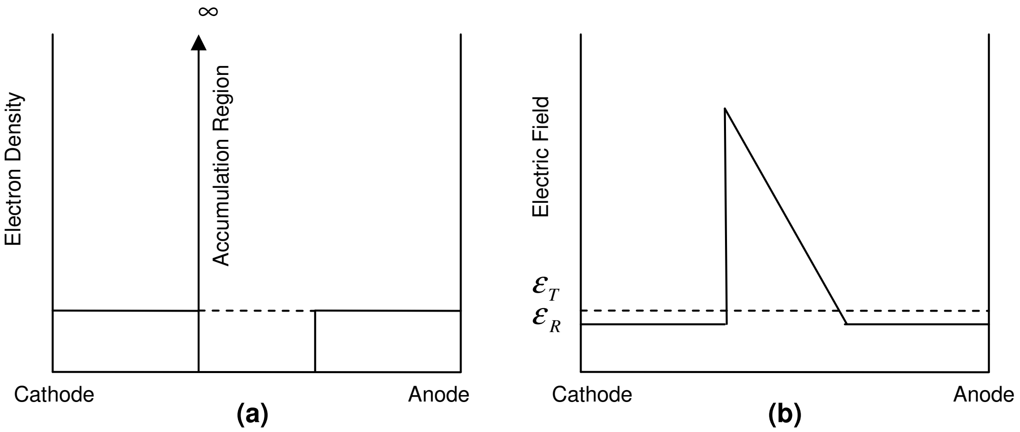

(a) **(b)**

Fig. 4.7 Zero Diffusion Domain profiles [5]

Finally, if the diffusion current is neglected i.e. diffusion coefficient D is zero, then the domain travels at the same velocity (v_D) as the electrons outside the domain (v_R). The electron density is zero in the depletion region and maximum (∞) at the accumulation region. Thus a triangular shaped electric field is formed within the domain, while outside domain the carrier concentration remains unchanged at N_D as shown in Fig. 4.7. The current density outside the domain is given as

$$J^* = N_D q v_R \qquad (4.13)$$

while inside the domain due to fully depleted region the current density is given as

$$J = \varepsilon_0 \varepsilon_r \frac{\partial \varepsilon}{\partial t} = -\varepsilon_0 \varepsilon_r \frac{\partial \varepsilon}{\partial x} v_D \qquad (4.14)$$

where v_D is the domain velocity. Poisson's equation requires that

$$\varepsilon_0 \varepsilon_r \frac{\partial \varepsilon}{\partial x} = -N_D q \qquad (4.15)$$

Thus the current density is given as

$$J = N_D q v_D \qquad (4.16)$$

whereas outside the domain at $\partial\varepsilon/\partial x = 0$ and carrier density $N = N_D$, using the current continuity equation

$$v_R = v_D \qquad (4.17)$$

the current is given as

$$J = q N_D v_R \qquad (4.18)$$

4.3.2 Device Oscillating Frequency

Generally in GaAs v_D is $\sim 1\times10^7 cm/s$ for moderately doped material. As the domain grows the current in an external circuit falls due to the fall in the field outside the domain. As the domain reaches the anode, the electric field gradient becomes zero and the domain collapses. The external electric field and current values increase until reaching the threshold value and allowing another domain to form at the cathode. The external current therefore oscillates at a frequency, which is inversely proportional to the transit length l_t (the distance between the domain formation point and anode). The oscillating frequency can therefore be given as:

$$f_0 = \frac{v_D}{l_t} \quad \text{...(4.19)}$$

Maximum operating frequency is determined by the material's inter-valley energy relaxation time. The electrons transfer from the Γ-valley to the L-valley and vice versa in a finite time. At high frequencies ~60 GHz the energy relaxation time is ~3×10^{-12} sec [2], which has a significant effect on energy relaxation time and as a result the RF cycle does not follow the $v-\varepsilon$ curve. The NDR is reduced since the current cannot rise as the electric field falls thus reducing the device efficiency and power [5].

4.3.3 The Doping – Length (*N*$_D$*L*) Product

Domain formation takes a finite time and distance and so to achieve stability requires a minimum device length l for a given doping density N_D. To determine the minimum device length, it is compared with the domain length under applied electric field. For a fully depleted triangular domain with width w, peak electric field ε_p and external field ε_R (as shown in Fig. 4.7b), the domain potential ϕ_D is given as:

$$\phi_D = (\varepsilon_p - \varepsilon_R)\frac{w}{2} \quad \text{...(4.20)}$$

From Poisson's equation

$$w = \frac{\varepsilon_0 \varepsilon_r (\varepsilon_p - \varepsilon_R)}{qN_D} \quad \text{..(4.21)}$$

And so solving equations 4.20 and 4.21, the domain potential becomes;

$$\phi_D = \frac{\varepsilon_0 \varepsilon_r (\varepsilon_p - \varepsilon_R)^2}{2N_D q} = \frac{qN_D w^2}{2\varepsilon_0 \varepsilon_r} \quad \text{.......................................(4.22)}$$

The ratio of peak to valley current is ~2 in GaAs, a threshold field twice as high as the electric field outside the domain. Mathematically the domain potential is given as;

$$\phi_D = \frac{w\varepsilon_T}{2} \quad \text{...(4.23)}$$

Thus it can be stated that

$$N_D l > \frac{\varepsilon_0 \varepsilon_r \varepsilon_T}{q} = 2.4 \times 10^{12} cm^{-2} \quad \text{...(4.24)}$$

4.3.4 Stable Operating Point of Domain

After analyzing the domain potential, the stable value of the outside field ε_R with regard to the applied voltage can be determined. If l_t is the device length, w the width, ϕ_D the domain potential and V_B the external bias voltage, then while maintaining the electrical boundary condition, the external bias voltage, V_B, is given as:

$$V_B = \phi_D + \varepsilon_R (l_t - w) \quad \text{...(4.25)}$$

As domain length is very small ($w <<< l_t$) it can be neglected and the bias voltage given as:

$$V_B = \phi_D + \varepsilon_R l_t \quad \text{...(4.26)}$$

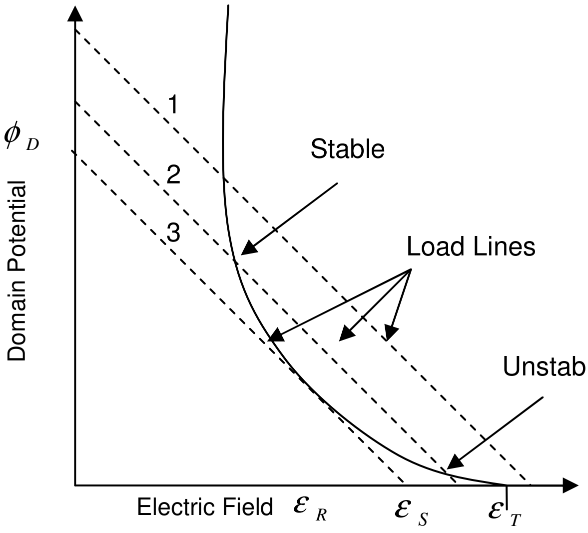

Fig. 4.8 The domain potential ϕ_D and minimum electric field ε_R (solid line) relationship due to the space-charge dynamics [2]

The minimum electric field value outside the domain required to sustain the domain is shown in Fig. 4.8, where for a constant voltage V_B, the domain potential ϕ_D is plotted against the minimum electric field ε_R. The three load lines correspond to three different terminal bias voltages (V_B). The intercepts are for a given doping density, N_D, and device length, l_t. Therefore, the following three configurations are possible [2, 29]:

- The average electric field, V_B / l_t, is greater than the threshold field yielding the load line 1, which intersects at a point higher than ε_T on the x axis. In this condition only one stable solution is possible.

- The average electric field V_B / l_t is greater than the sustaining voltage $V_S / l_t = \varepsilon_S$ but less that the threshold field (giving load line 2). For V_B / l_t less than ε_T, two solutions are possible. The first intersection point of the ϕ_D - ε_R curve and load line gives a stable operating point. It can be seen that for a steep load line i.e. a long device, the stable operating point is approximately half the threshold value. Therefore, as shown earlier in equation 4.26, the domain will sustain and continue to propagate even if the external voltage drops below the threshold voltage. The unstable intersection is explained through consideration of a small noise fluctuation, which causes ϕ_D to increase, thus decreasing ε_R. A decrease in the value of ε_R shifts the state higher than the ϕ_D - ε_R curve. It shows that outside the domain the electrons are moving faster than those inside the domain. It will cause the accumulation and depletion regions to grow to keep the Poisson's equation satisfied, resulting in a further increase in ϕ_D. Eventually it will reach steady state and the stable point on the load line will be achieved.

- The average electric field V_B / l_t is equal to the sustaining voltage $V_S / l_t = \varepsilon_S$ which gives line 3. This condition causes the domain to terminate while still growing, with V_B / l_t greater than or less than the sustaining voltage. At the sustaining voltage the load line is tangent to the ϕ_D - ε_R curve. Thus V_S is considered very important for the domain to grow and be sustained.

4.4 Conventional Gunn Diode

The Gun diode in its basic form is a homogenous device with ohmic contacts at each end. The device has a sandwiched structure and comprises of n^+ contact layers at the ends with a n^- transit region in between, as shown in Fig. 4.9.

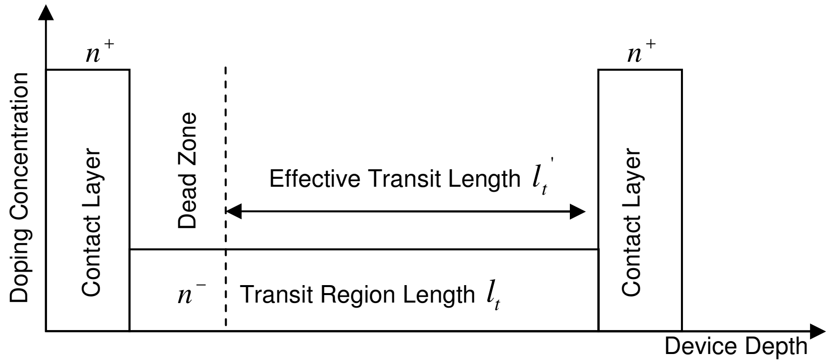

Fig. 4.9 **Conventional Gunn Diode structure**

As previously described, the transit region length partially determines the device’s operating frequency. However, domain formation in conventional Gunn diodes does not occur in the initial portion of the transit region, where the electrons are being accelerated to the energy levels required for inter-valley transfer. This initial portion is termed as the dead zone. Thus domain formation occurs at a certain distance away from the cathode depending on the applied bias. This reduces the effective length of the transit region and acts as parasitic positive resistance, which degrades the overall negative resistance and results in a reduction in DC-to-RF conversion efficiency. Generally the length of the dead zone is about 40 percent of the transit length in high frequency devices depending on the transit length and the applied bias [67]. The applied bias determines the point of domain nucleation, making the effective transit length and therefore operating frequency very sensitive to the applied bias.

The temperature effects on conventional Gunn diodes and their limitations are discussed below;

4.4.1 Temperature Effects on Conventional Gunn Diode

The temperature dependence of the velocity-field characteristic of low doped GaAs is shown in Fig. 4.10 [2]. The average electron velocity is lower than the formation energy of optical phonons (~0.035 eV in GaAs) at low lattice temperature and low electric field [68]. The electrons attain high drift velocity before acquiring sufficient energy for inter-valley transfer. At lower temperatures the threshold field and the onset of NDR decreases due to the shift of the domain nucleation point towards the cathode. This shift increases the device’s effective transit length and reduces the operating frequency [5]. However, the device critical current at the onset of NDR increases. Likewise, the device turn on voltage, required to achieve stable oscillations, also increases with reducing temperature. Thus a high turn on voltage results in lower device efficiency and output power. These factors make the conventional diodes operational characteristics extremely sensitive to changes in ambient temperature.

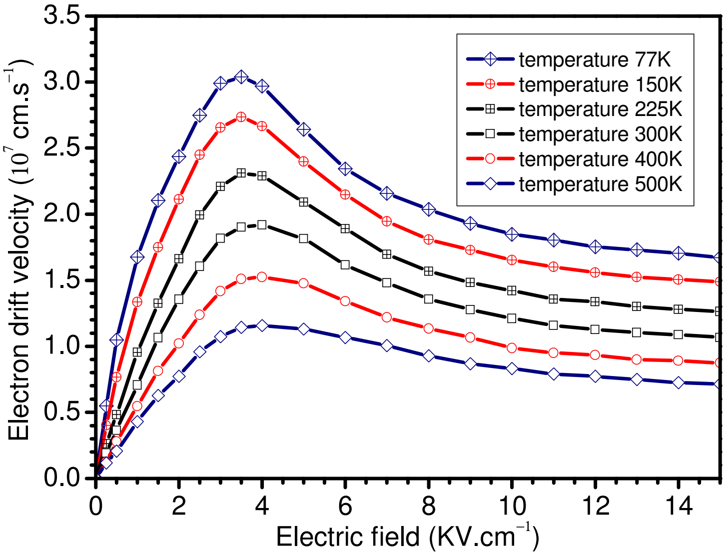

Fig. 4.10 **GaAs temperature dependant electron drift velocity curves. The curves are plotted in SILVACO using MOCASIM (Monte Carlo simulator) for GaAs 1.1x10^{-16} doped.**

4.4.2 Limitations of the Conventional Gunn Diode

Conventional GaAs Gunn Diodes can provide around 500 mW power at 20 GHz with 5.5% efficiency. The efficiency reduces to about 1.5% at 60 GHz and power to 50 mW. It has also been observed that at 77 GHz with 0.8% efficiency, powers of up to 50 mW have been achieved. The conventional Gunn Diode limitations are as follows [5]:

- The device has a high turn on voltage.
- The device exhibits poor bias and temperature stability
- Thermal parasitics value is high at higher frequencies.
- The device operating current is high thus leading to more power dissipation.
- At mm frequency the device has lower efficiency and provides lower power.

A number of these limitations are directly related to the presence of the transit region dead zone [67]. To overcome the limitations imposed by this the graded gap GaAs/AlGaAs hot electron injector Gunn diode was proposed [69]. The hot electron injector effect on dead zone reduction has been demonstrated by Monte Carlo analytical simulations [70] and experimental results [11, 69]. The state of art Gunn diode with step graded gap hot electron injector is the topic of discussion in the next chapter.

4.5 Gunn Diode Oscillation Modes

A Gunn diode generally needs to be placed in a resonant circuit to generate usable microwave power. In a controlled circuit various modes of operation are possible. The major factors affecting the mode of operation are:

- Device transit region length
- The resonant frequency of the external circuit
- Applied bias voltage
- Device doping uniformity and concentration

The various possible modes of operation will now be discussed.

4.5.1 Transit Time Mode

If the external circuit is purely resistive ($L \rightarrow \infty, C \rightarrow 0$) the device will operate in transit time mode and the domain transit-time across the transit region determines the operating frequency as long as the bias voltage is kept greater than the threshold field. Narrow current spikes are observed when the domain collapses at the anode and the next is being nucleated near the cathode as shown in Fig. 4.11. The oscillating frequency is therefore inversely proportional to the space-charge or domain transit time τ_d and is given as:

$$f_r = \frac{1}{\tau_d} = \frac{v_{drift}}{l_t} \qquad \text{(4.27)}$$

where v_{drift} is the electron drift velocity and l_t is the transit region length [29]. In this mode the voltage amplitude is small and current pulses narrow, indicating the conversion efficiency of this mode is low with a high harmonic content. Disadvantages of this mode is that the transit time frequency strongly depends on the temperature and operating voltage rather than the characteristics of the external circuit, thus poor bias and temperature stability are observed.

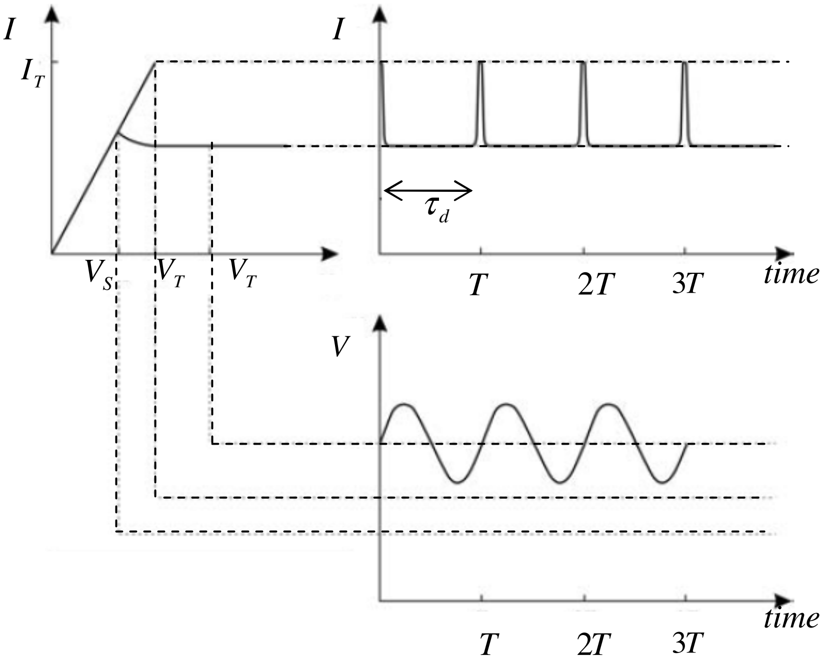

Fig. 4.11 **Transit Time Mode - I-V and Time Evolution [4]**

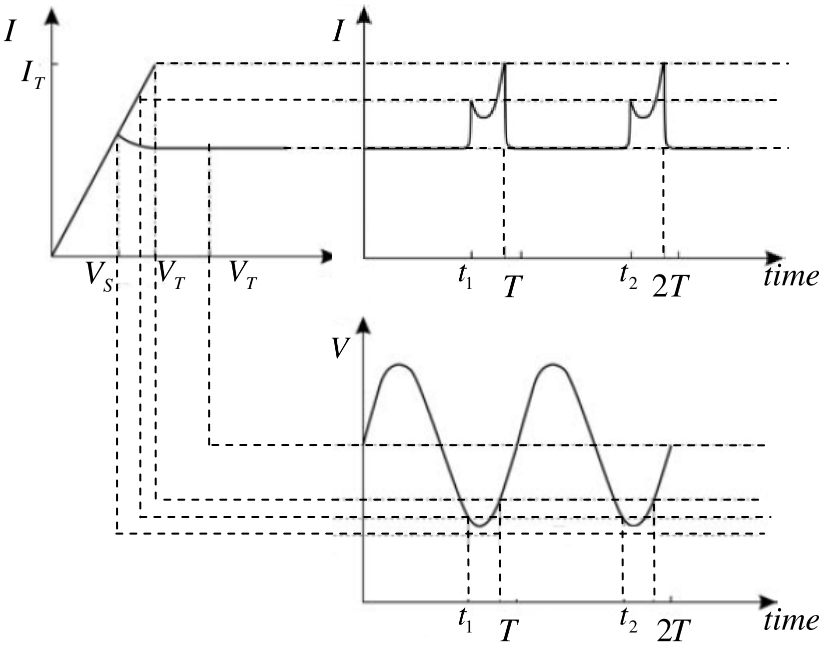

Fig. 4.12 **Delayed Domain Mode- I-V and Time Evolution [4]**

4.5.2 Delayed Domain mode

In delayed domain mode the external bias voltage drops below the threshold field level during part of RF cycle as shown in Fig. 4.12. This results in the delayed nucleation of the second domain at the cathode. Care is taken to avoid reduction of bias voltage below the sustaining voltage. Thus as the field drops below the threshold as the first domain reaches the anode and collapses, the new domain at the cathode does not nucleate until the field rises above the threshold value. This effect causes a reduction in the device operating frequency which is always below the transit time frequency. In this mode the resonant frequency of the external circuit determines the operating frequency. In other words the resonant period of circuit $T_r = 1/f_r$ is greater than τ_d, and so the device frequency is given by;

$$\frac{1}{2\times\tau_d} = \frac{v_{drift}}{2\times l_t} < f_r < \frac{1}{\tau_d} = \frac{v_{drift}}{2\times l_t} \quad \ldots\ldots\ldots\ldots\ldots\ldots\ldots\ldots\ldots\ldots\ldots\ldots(4.28)$$

Generally in delayed domain mode, devices can be operated over a wide range of frequencies depending on the external circuit. Additionally, the current spikes are broader with low harmonics thus yielding higher conversion efficiency.

4.5.3 The Quenched Domain Mode

In this mode the domain is quenched during the RF cycle due to a decrease in terminal voltage below the sustaining voltage. A new domain at the cathode does not nucleate until the terminal voltage rises above the threshold value as shown in Fig. 4.13. Operating devices in quenched domain mode yields higher operating frequencies and efficiencies than in transit time mode. In this mode the period of the resonant circuit $T_r = 1/f_r$ is less than τ_d, but is greater than the domain nucleation and extinction time τ_n.

$$\frac{1}{\tau_d} = \frac{v_{drift}}{l_t} < f_r < \frac{1}{\tau_n} \quad \ldots\ldots\ldots\ldots\ldots\ldots\ldots\ldots\ldots\ldots\ldots\ldots\ldots\ldots\ldots(4.29)$$

Conversion efficiency is lower than in delayed domain mode due to the tendency of quenched domain devices to generate narrow spike currents. It can be shown by considering the area under the pulse that the efficiency is about 5% higher than that of transit-time mode [2].

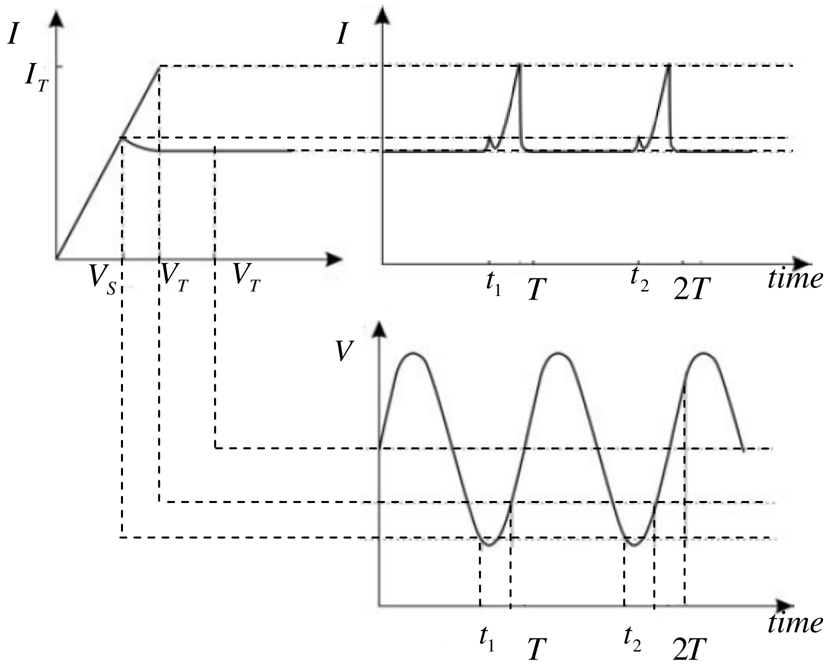

Fig. 4.13 Quenched Domain Mode- I-V and Time Evolution [4]

4.5.4 Low Space-charge Accumulation (LSA) mode

In LSA mode the external circuit configuration again plays a vital role. The effect has been explained by Copeland [71], in that the circuit causes the electric field to rise above the threshold field value and drops down instantly such that the space charge distribution associated with the high field domain does not have enough time to form. In this mode the operating frequency is much greater than that set by the device transit length. In other words the frequency is so high that the domain does not get enough time to form fully, while the field is above the threshold value. In LSA mode the I-V characteristics follows the velocity electric field ($v-\varepsilon$), which exhibits the negative differential mobility region.

The biggest advantage of this mode is the very high frequencies achievable, since the device length is not related to the operating frequency. Additionally, the mode provides high output powers since high terminal voltages can be applied without causing impact ionization [2] and efficiencies of up to 18.5% have been demonstrated [72].

4.5.5 Operating Modes Summary

The various operating modes discussed for GaAs are illustrated in Fig. 4.14 in terms of the stable oscillation, domain oscillation and LSA oscillation regions. In the stable region the device is used as an amplifier, since no domain formation occurs for $N_D l < 10^{12} cm^{-2}$. While for $N_D l > 10^{12} cm^{-2}$ three oscillation modes (Transit time, delayed domain and quenched) are possible. In GaAs case, at higher frequencies and $N_D / f \in [2\times10^{10}, 2\times10^{11}] sm^{-3}$, the device operates in LSA mode [73]. In all the modes the device boundaries vary depending on the applied bias voltage, circuit loading and environmental effects.

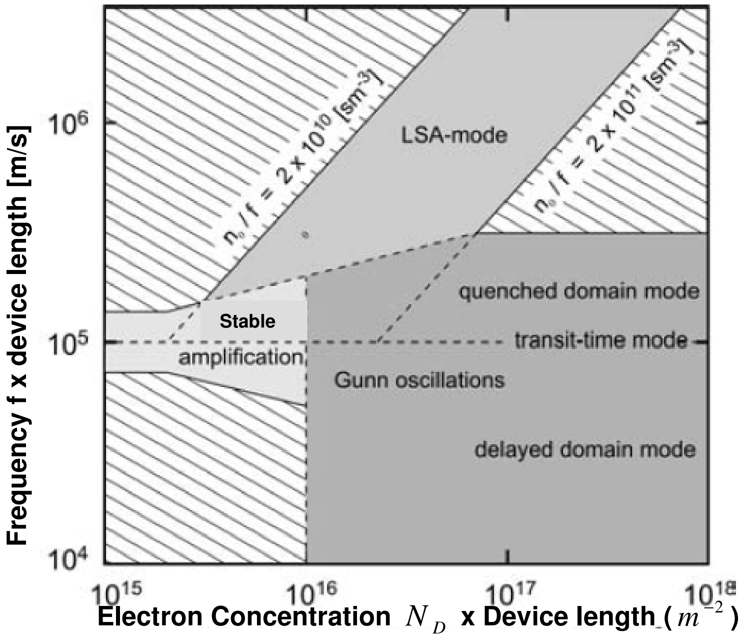

Fig. 4.14 **Gunn Diode Operating Modes Summary [2]**

4.6 Conclusion

The transferred electron effect was reviewed in detail through Electric Field Effects on Electron Drift Velocity, High Field Transport in n-GaAs, Negative Differential Resistance (NDR) and Conditions for Negative Differential Mobility. A detailed account of conventional Gunn diode theory has been provided with an explanation of the Negative Differential Resistance (NDR) effects, which depends on the bulk material properties.

A Gunn diode generally needs to be placed in a resonant circuit to generate usable microwave power. It was shown that in a controlled circuit various modes of operation are possible. The major factors affecting the mode of operation were shown as device transit region length, the resonant frequency of the external circuit, applied bias voltage and device doping uniformity and concentration. The various possible modes of operation were discussed.

The temperature effects on conventional Gunn diodes and their limitations were presented. The limitations included high turn on voltage, poor bias and temperature stability, high thermal parasitics value at higher frequencies, high operating current thus leading to more power dissipation and lower efficiency at mm-wave frequencies. It was shown that number of these limitations is directly related to the presence of the transit region dead zone. To overcome the limitations imposed by this the state of art Gunn diode with step graded gap hot electron injector is the topic of discussion in the next chapter.

Chapter 5 Advanced GaAs Gunn Diodes with Graded AlGaAs Hot Electron Injection

5.1 Introduction

A semiconductor structure formed between two dissimilar semiconductors joined together is known as a heterojunction, which gives rise to a heterostructure device. The heterostructure formed through epitaxial growth of one semiconductor on top of the other such as the wide bandgap material (AlGaAs) and narrow band gap material (GaAs) exhibits special properties. The heterojunction properties depend on the distribution of the band gap discontinuity (ΔE_g) between the conduction band offset (ΔE_c) and valence band offset (ΔE_v). The conduction band wave function primarily evolves from the atomic wave function of cations (Ga and Al) and the valence band wave function evolves from the atomic wave function of anions [74]. Thus the valence band structure of GaAs–AlGaAs heterostructure sharing a common anion element (As), is smaller than the conduction band offset i.e. $\Delta \mathrm{E}_c / \Delta \mathrm{E}_v \cong 2/1$ for direct gap range of $Al_x Ga_{1-x} As (x < 0.4)$.

The maturity of device growth techniques such as Chemical Vapour Deposition (CVD) and the more precise Molecular Beam Epitaxy (MBE) has led to the commercial manufacturing of devices which rely on bandgap engineering. Increase in RF power and improved efficiency of a Gunn diode with the introduction of a heterojunction based hot electron injector was first reported in 1988 [75]. It was shown that under forward bias electron energy increases by an amount equal to the AlGaAs-GaAs conduction band offset as the electron passes through the injector region. Thus by keeping the conduction band offset at the end of the AlGaAs injector close to the GaAs inter-valley separation, electrons will be injected directly into the satellite valley. Therefore, the device dead zone is effectively eliminated.

5.2 AlGaAs/GaAs Graded Gap Heterostructure

AlGaAs is capable of forming a lattice matched heterostructure with GaAs (lattice mismatch is $\Delta a / a \leq 1.2 \times 10^{-3}$) and provides a band gap range of 1.424 to 2.1 eV through variation of the Al components. The graded gap AlGaAs alloy is formed by using the chemical formula $(GaAs)_x (AlAs)_{1-x}$, where x is the mole fraction (or compound chemical composition). If the semiconductors are not lattice matched then microscopic defects occur in the material, which significantly degrade the device performance. The dependence of forbidden-gap energy on the Al fraction '*x*' is usually expressed in terms of parabolic (linear plus quadratic) dependence. The magnitude of the parabolic factor is termed as the bowing parameter E_b. The bandgap energy of the alloy $Al_x Ga_{1-x} As$ is given as:

$$E_{g\,(Al_x Ga_{1-x} As)} = x(GaAs) + 1 - x(AlAs) + x(1-x)E_b \text{ eV} \ldots\ldots\ldots\ldots (5.1)$$

where term $x(1-x)E_b$ describes the quadratic dependence of the gap. However, for $Al_x Ga_{1-x} As$ the bowing parameter is very small thus its band gap is given as:

$$E_{g\,(Al_x Ga_{1-x} As)} = x(GaAs) + 1 - x(AlAs) \text{ eV} \ldots\ldots\ldots\ldots (5.2)$$

At room temperature, the bandgap is given by the following empirical formula [37]:

$$E_{g\,(Al_x Ga_{1-x} As)} = 1.42 + 1.25x \text{ eV} \ldots\ldots\ldots\ldots (5.3)$$

The distribution of the bandgap discontinuity (ΔE_g) between the conduction (ΔE_c) and valence (ΔE_v) band has been researched extensively. Experimental data suggests that the ratio is approximately 60:40 for Al fractions less than 0.45 [4, 76, 77]. The conduction band offset is given as:

$$\Delta E_c = 0.6[E_{g\,(Al_x Ga_{1-x} As)} - E_{g\,GaAs}] \text{ eV} \ldots\ldots\ldots\ldots (5.4)$$

Thus from equations 5.3 and 5.4 the conduction band offset can be written as:

$$\Delta E_c = 0.75x \text{ eV} \quad \text{...(5.5)}$$

5.3 Hot Electron Injection

Electrons with kinetic energy greater than *kT*, where K_B is the Boltzmann's constant and *T* is the lattice temperature, are known as hot electrons. The process of raising the electron energy to the level of the satellite L band and its introduction into the transit region is known as hot electron injection. By employing a hot electron injector just before the transit region the device dead zone can be effectively eliminated. Additionally it results in the following advantages [4]:

- The turn on voltage improves (reduces), especially at low temperatures.
- Increase in device efficiency.
- Reduction in phase noise.
- Improved temperature stability characteristics.

The concept of graded gap hot electron injector and AlGaAs-GaAs hot electron injector are discussed.

5.3.1 The Graded Gap Hot Electron Injector Concept

The potential profile of a linearly graded hot electron launcher can be approximated to a triangular shape as discussed below [5]:

At zero bias condition Fig. 5.1 (a) shows the right hand side (RHS) and left hand side (LHS) of the barrier height ϕ_1 with lengths l_2 and l_1 respectively. A forward bias V_B results in a potential shift ϕ_2 given as:

$$\phi_2 = \phi_1 + \frac{l_2 V_B}{l_1 + l_2} \quad \text{...(5.6)}$$

A potential V_B changes the electric field on RHS given as:

$$\varepsilon_2 = \frac{\phi_1}{l_2} + \frac{V_B}{l_1 + l_2} \quad \text{..(5.7)}$$

The change in ε_2 becomes vanishingly small if the length $l_1 >> l_2$. The longer region on the LHS gives a rising potential profile and the small l_2 results in an abrupt interface at the injector transit region interface. Thus the injector structure with long rising potential region from cathode and abrupt interface gives an ideal potential profile for a heterostructure Gunn diode.

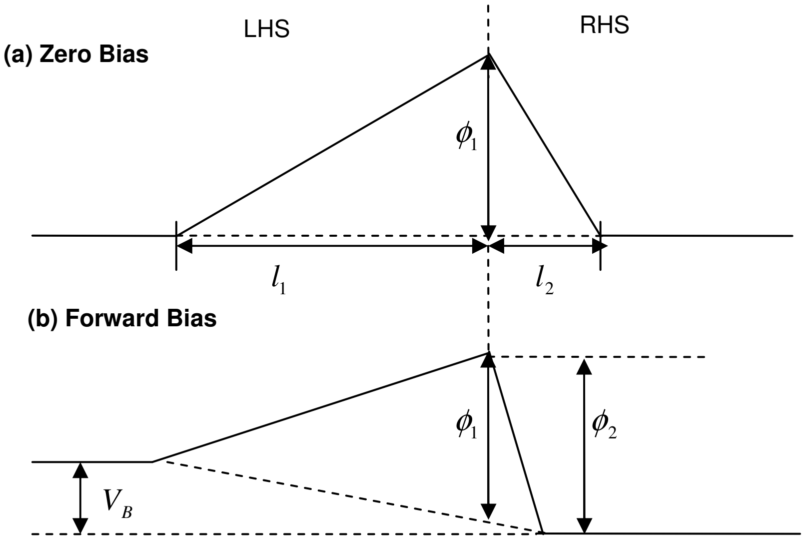

Fig. 5.1 Potential profile of Hot Electron Injector [5]

5.3.2 The AlGaAs/GaAs Hot Electron Injector

The AlGaAs/GaAs hot electron injector consists of two components: a step-graded AlGaAs barrier (launcher) and a thin n^+ GaAs doping spike. The graded AlGaAs barrier is used to form a launcher to ensure that the electrons gain sufficient energy to transfer directly in to the transit region conduction band satellite valley. The width of the launcher is large enough to avoid tunnelling at low energy levels while being narrow enough to avoid significant increase in the device's serial resistance. The n^+ doping spike is required to modify the downstream electrical field in the transit region and eliminate the depletion region which would be formed in its absence [70]. The hot electron injector structure is shown in Fig. 5.2.

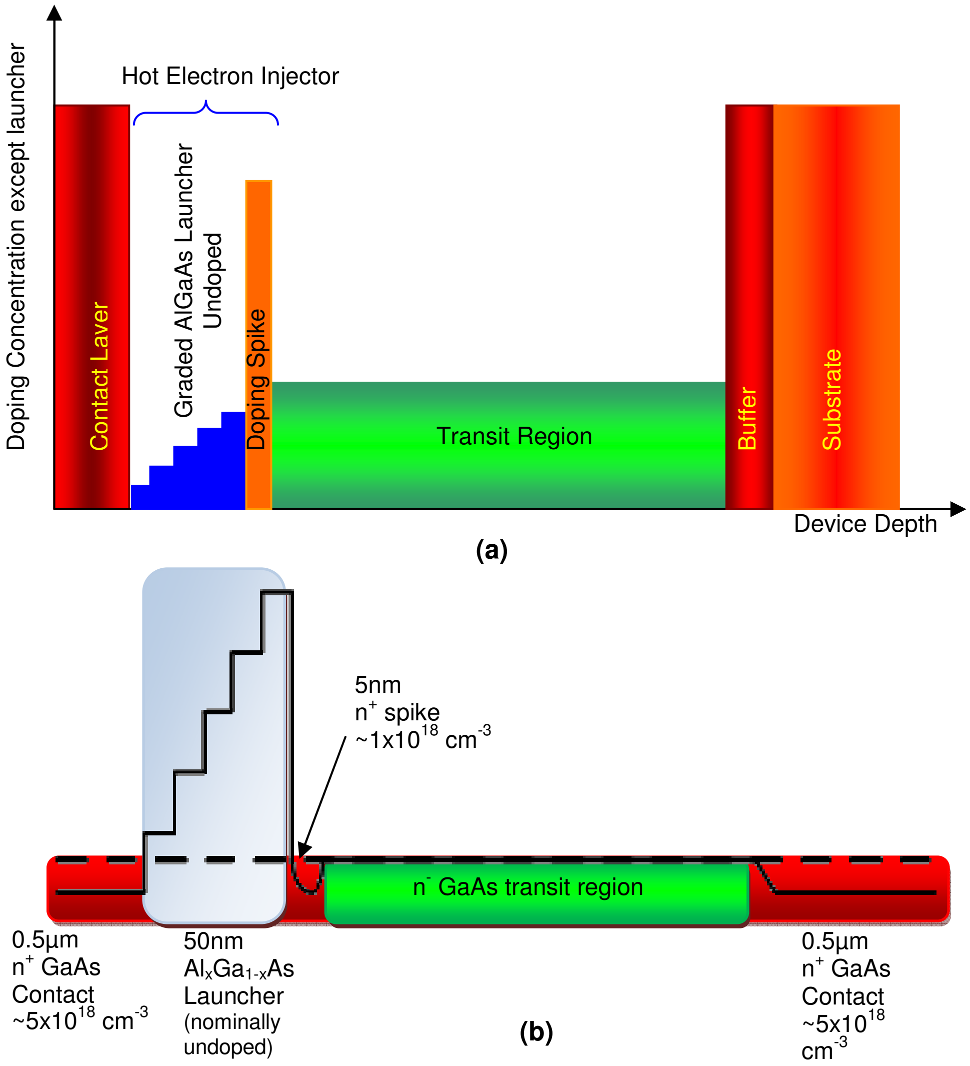

Fig. 5.2 **(a) Structure of a GaAs Gunn Diode with step graded hot electron injector (b) Conduction band profile of a Step Graded AlGaAs heterostructure Gunn Diode.**

The linear graded $Al_xGa_{1-x}As$ launcher was introduced with Al fraction '*x*' increased from the cathode side to its maximum value at the injector-transit region. The maximum Al composition used was 30% to form a conduction band discontinuity of 0.32 eV at the injector-transit interface [69]. Couch further concluded that the thickness and doping of n^+ GaAs layer played crucial part in the device performance.

The structure similar to the proposed by Couch was optimized [69] to yield high RF power and efficiency. The optimized device structure is shown in Fig. 5.3. It has an undoped AlGaAs step graded barrier (from 1.7% to a maximum value of Al ~32%). The maximum Al composition 0.32 formed the conduction band discontinuity of 0.38 eV at the injector-transit interface, which improved the device performance significantly [69]. The structure has two spacers to avoid dopant diffusion into the graded barrier, which is followed by highly doped delta (δ) layer and a thick transit region with low doping.

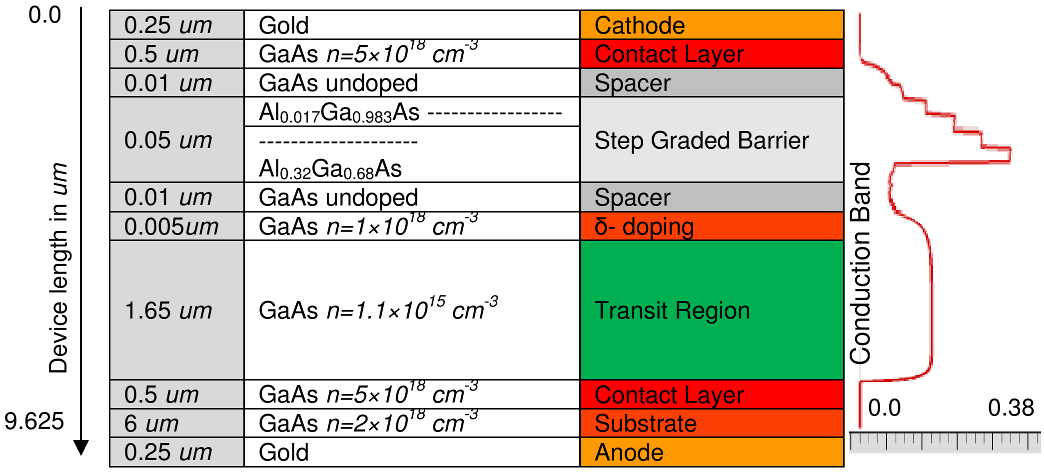

Fig. 5.3 **Typical advanced step graded injector Gunn Diode structure**

5.4 I-V Characteristics of graded gap injector GaAs Gunn Diode

Typical DC characteristics of Gunn Diodes with and without injector are shown in Fig. 5.4. The injector gives rise to asymmetrical I-V characteristics due to the Schottky like behaviour of the injector in reverse bias. The asymmetrical I-V plot indicates different electron occupations in the L-valley for forward and reverse currents due to the position of injector in the device. The graded gap injector starting from cathode is only effective in forward bias: in reverse bias it does not influence election transfer into the transit region. It may be noted that the injector effectiveness can be evaluated from the ratio of forward and reverse currents ($J_p^{Fw}/J_p^{\mathrm{Re}}$) and, to a point, high values are desired for high overall device efficiency [11]. This will be discussed in more detail later.

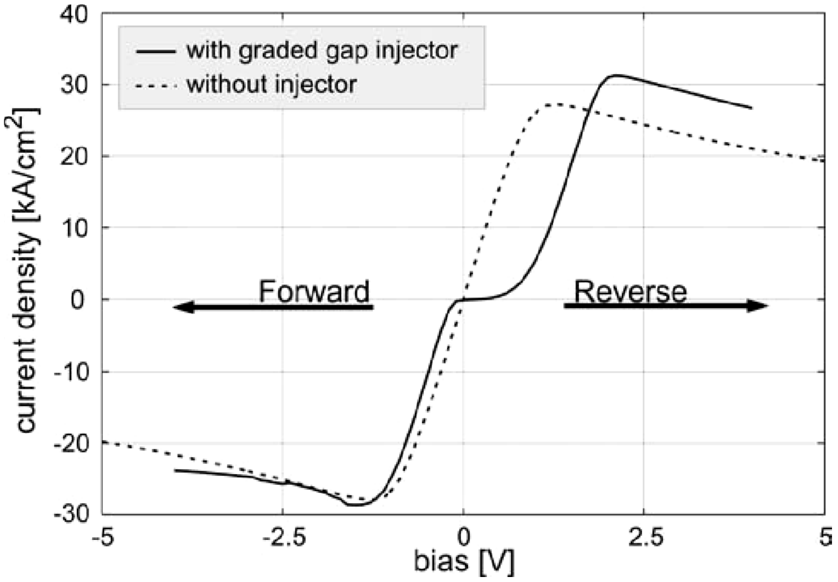

The heterostructure graded gap Gunn diode [11, 12], high frequency investigations, effects of hot electron injector barrier height and carrier concentration in the doping spike are discussed.

5.4.1 High Frequency Investigations of GaAs Gunn Diodes

The Gunn diode with graded gap injector admittance graphs are shown in Fig. 5.5 for negative (forward bias) and positive (reverse bias) voltages. The reverse bias graph is similar to the diode without graded gap injector. However, in forward bias a sharp negative peak in the response at 60 GHz shows the reduction in dead zone due to the graded gap injector. Additionally a second harmonic signal can also be observed at ~110 GHz [11].

5.4.2 Hot Electron Injector Barrier Height

The step graded heterostructure barrier with 32% maximum Al concentration provides a conduction band offset of ~0.38eV [78]. The comparative measurements for Al content in the range 28-32% is shown in Fig. 5.6 [10]. It can be seen that, as expected, increasing Al content makes the Schottky like behaviour more pronounced in the reverse direction due to higher barrier height. In the forward direction the peak saturation current reduces with the increase in

Al content due to higher transfer rate of electrons from the Γ to the L valley and higher injector efficiency [10].

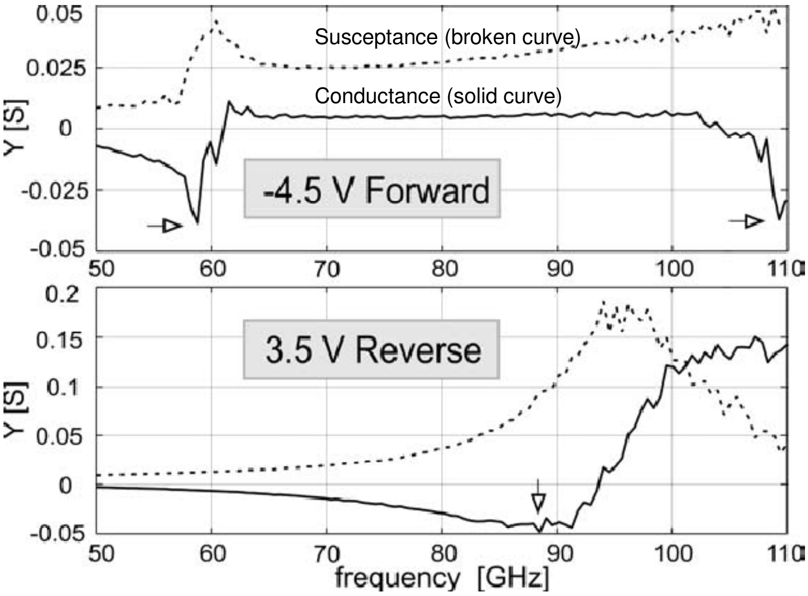

Fig. 5.5 **Conductance and Susceptance versus Frequency plot [11]**

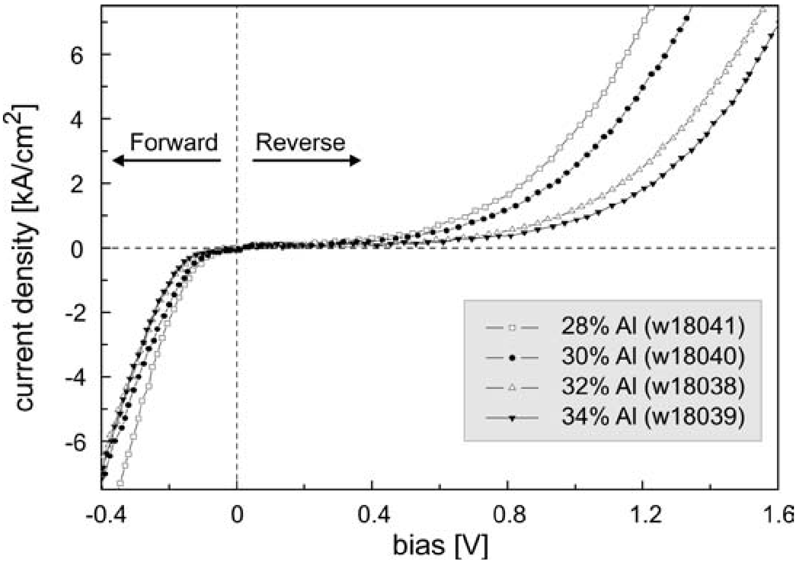

Fig. 5.6 **Low voltage I-V characteristics [11]**

5.4.3 Doping Spike

In addition to injector barrier height, the doping level of the spike plays an important role in controlling the electric field potential behind the graded gap barrier. The appropriate electric field potential behind the graded gap barrier retain the hot electron properties [10, 51, 79]. It has been shown [78] that the absence of an n^+ doping spike results in the opposite electric field gradient to that required for domain formation and in forward bias a dead zone is formed at the start of the transit region as shown in Fig. 5.7. The n^+ doping spike eliminates the depletion region as shown in Fig. 5.8. The thickness of the n^+ doping spike is kept lower than the injected electrons mean free path [51, 78].

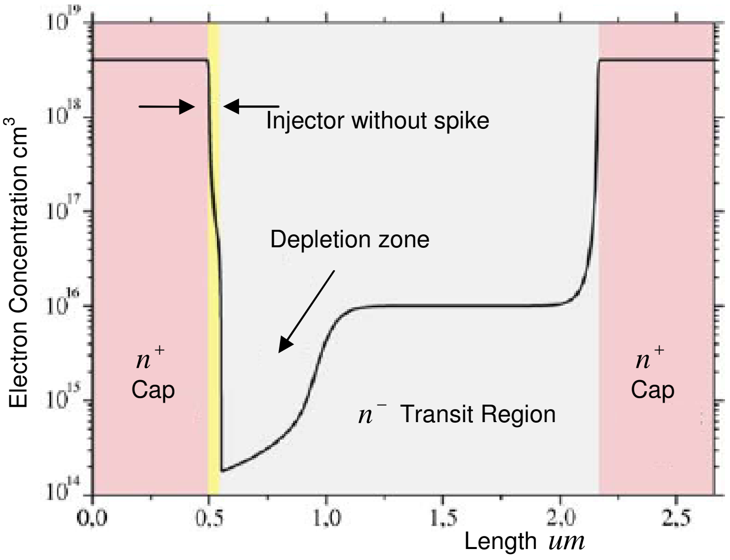

Fig. 5.7 Electron Concentration – without doping spike [10]

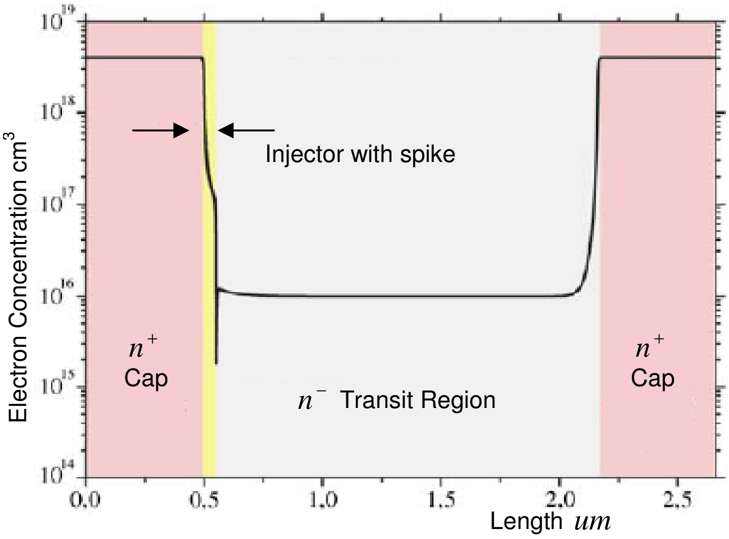

Fig. 5.8 Electron Concentration – with doping spike [10]

5.5 Drift Velocity Computation and Operation Mode Classification

In the Gunn diode, electron drift velocity in the transit region is dependent on factors such as injector barrier height, electric field and temperature [10, 11]. A small signal analysis is shown in Fig. 5.9 illustrating measured drift velocity against applied voltage at negative conductance frequency (f_{NCM} 77 GHz) for an active region length of 1.6 µm. The Gunn diode with injector achieved an asymmetric response and in forward bias the drift velocities were smaller due to the injector's hot electrons entering the active region, while in reverse bias the response was similar to a diode without injector. The graph represents operation in transit time mode for drift velocities of $v_o = 1.23x10^7 cm/s$. The experimental data indicated that the injector with Al fractions of 32% and 34% provided stable 77 GHz oscillations in the Quenched domain mode [10, 11].

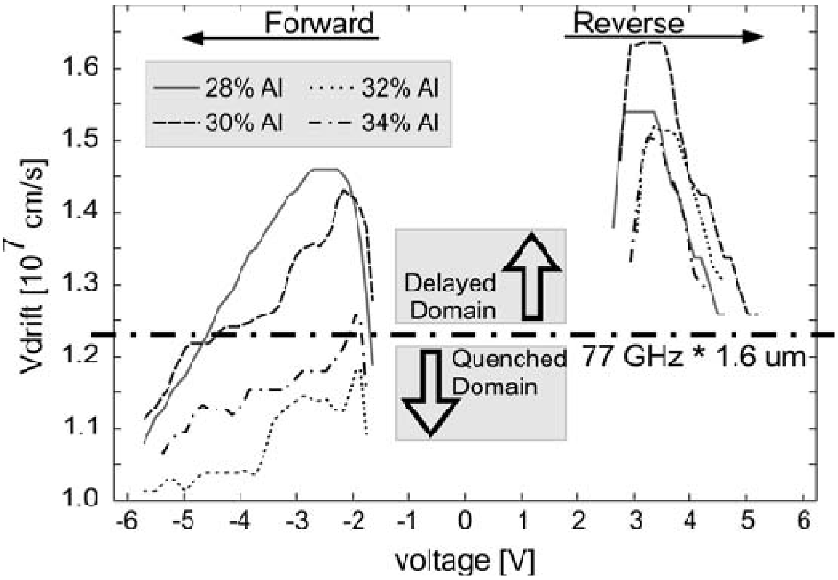

Fig. 5.9 **Diode with Injector [11]**

Fig. 5.10 shows electron occupation in the L-valley obtained from drift velocity data and plotted for different electric fields [10]. Due to its dynamic nature prediction of the electric field in the transit region is complicated and so data was obtained using SILVACO™ simulations [11]. The emphasis was on the effect of carrier concentration (n_Γ, n_L) and mobilities (μ_Γ, μ_L) on device operating frequency (f_{NCM}), which changed due to the change in ratio of n_Γ and n_L.

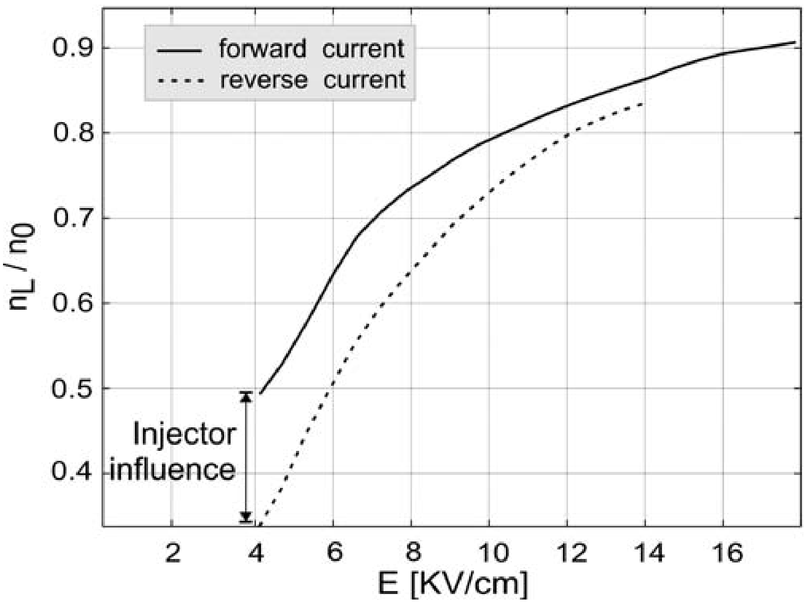

Fig. 5.10 **Electrons occupations in the L- valley [11]**

5.6 Conclusion

The Advanced GaAs Gunn Diodes with graded AlGaAs hot electron injector concept and theory was discussed in detail. It was shown that under forward bias electron energy increases by an amount equal to the AlGaAs-GaAs conduction band offset as the electron passes through the injector region. Thus by keeping the conduction band offset at the end of the AlGaAs injector close to the GaAs inter-valley separation, electrons will be injected directly into the satellite valley. Therefore, the device dead zone is effectively eliminated and the device was shown to have overcome the limitations of the conventional Gunn diode. Additionally, dead zone elimination was shown to be advantageous due to improvement in the device turn on voltage, increased device efficiency, reduction in phase noise and improved temperature stability characteristics. The concept of graded gap hot electron injector and AlGaAs-GaAs hot electron injector was presented.

Typical DC characteristics of Gunn Diodes with and without injector were compared. It was shown that the injector gives rise to asymmetrical I-V characteristics due to the Schottky like behaviour of the injector in reverse bias. The heterostructure graded gap Gunn diode’s high frequency investigations; effects of hot electron injector barrier height and carrier concentration in the doping spike were presented. Finally drift velocity computation and operation mode classification were discussed for an advances AlGaAs/GaAs hot electron injector Gunn diode.

Chapter 6 Gunn Diode Model developments

6.1 The SILVACO^{TM} TCAD Suite

SILVACO^{TM} is a software package which provides a Virtual Wafer Fabrication (VWF^{TM}) simulation environment in which two or three dimensional device simulations can be performed (using the ATLAS^{TM} simulation engine) [80]. It is physically-based and allows the electrical, optical, thermal characteristics of a semiconductor device to be simulated under given bias conditions to obtain DC, RF and time domain responses. The response of the model is simulated through definition of data on mesh points (nodes) throughout the volume (or area if 2D) of the structure and the subsequent solution of differential equations. The simulations are cost effective and quick in contrast to performing experiments and besides potentially yielding a predictive model for a given device, can provide insight into device operation and analysis of the underlying theoretical concepts. Data which is difficult to obtain from actual experiments can also be obtained using simulation. However, despite numerous advantages, these simulations are difficult to perform because they require thorough understanding of the device physics and knowledge of suitable physical model parameters.

In SILVACO^{TM}'s VWF^{TM} environment ATLAS^{TM} is the core tool for ATLAS^{TM} physically-based two or three dimensional device simulation. It determines the electrical behaviour of a structure created by DevEdit^{TM} and provides insight into the device's internal physical mechanisms. Fig. 6.1 shows the types of information which flow in and out of ATLAS^{TM} [81]. The two input files are the device structure and input text file containing structure and execution commands. During device simulations, ATLAS^{TM} creates three output files: The *Runtime output* file provides the simulation progress, error or warning messages. The *solution* file stores the solution variables data for the given conditions. The *log* file stores all terminal voltages and currents from the device analysis.

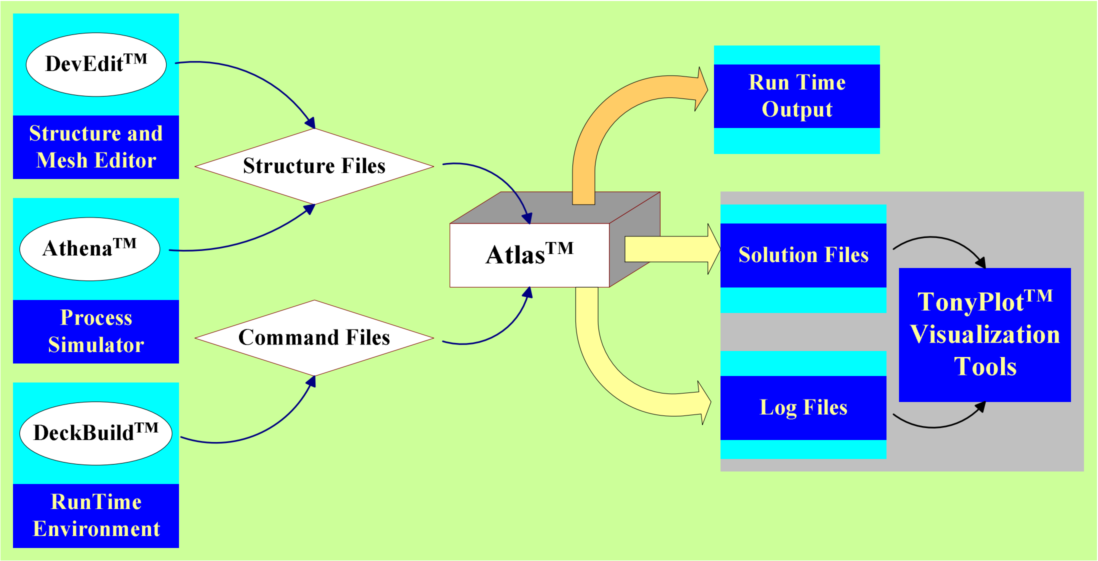

Fig. 6.1 ATLAS™ Input-Output hierarchy [81]

In the ATLAS™ program flow, the order in which statements are defined is crucial. There are five groups of statements which need to be specified in the order shown in Fig. 6.2 to ensure correct execution. After specifying the device structure in DevEdit™, the *material* and *model* statements are defined in DeckBuild™. The material statements are used to define basic material parameters relating to band structure, mobility, recombination and carrier statistics etc. The *model* statement specifies the inclusion of various physical mechanisms, models, and other parameters such as the global temperature for the simulation. The *method* statement is then used to set the numerical methods to calculate the solution under various bias conditions. Parameters in the *method* statement also set the tolerances for data convergence. Finally the results are extracted and presented using TonyPlot™ [81].

ATLAS™ uses its sub-engine 'Blaze' for heterostructure device simulations. Blaze is a general purpose 2D device simulator used for III-V materials and is invoked by default for heterostructures with a position dependent band structure. During simulations it modifies the charge transport equations to account for the effects of positionally dependent band structures [81].

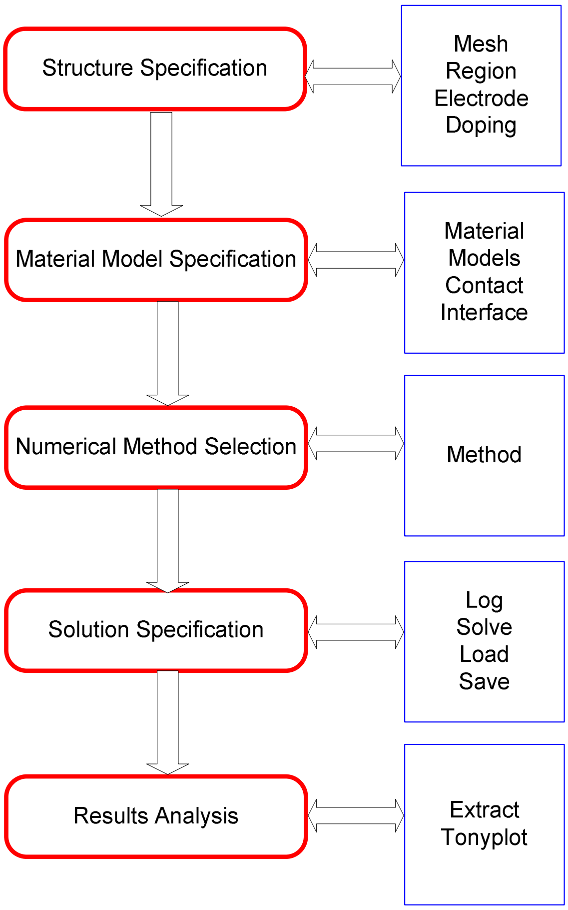

Fig. 6.2 **ATLAS™ command groups [81]**

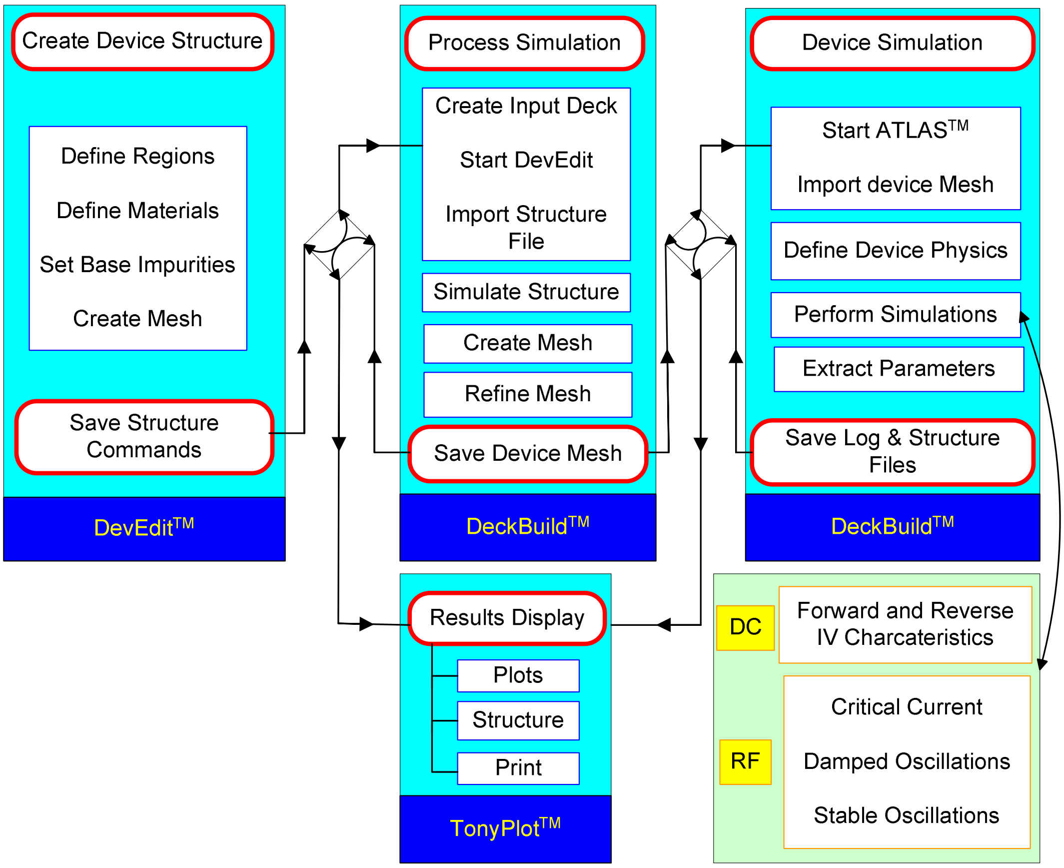

Fig. 6.3 **Gunn Diode model development process flow**

6.2 Development of the Simulation Model

The device structure was first defined in ‘DevEdit^{TM}’, which provides a simple Graphical User Interface (GUI) development environment [82]. A device structure file is then constructed and saved by ‘DevEdit^{TM}’. This is then opened in ‘DeckBuild^{TM}’ and simulated using ‘ATLAS^{TM}’ as illustrated in Fig. 6.3. Finally the results are plotted using ‘TonyPlot^{TM}’.

The 77GHz second harmonic graded gap injector Gunn diode epitaxial structure, 2D model, 2D model with heat sink, 3D rectangular model and 3D cylindrical model development is discussed below;

6.2.1 High Speed Heterostructure Graded Gap Injector Gunn Diode

A state of art GaAs Gunn diode with a step graded AlGaAs hot electron injector has been selected for modelling using SILVACO^{TM}. The typical device structure is shown in Fig. 6.4 and is similar to that described in chapter 5.

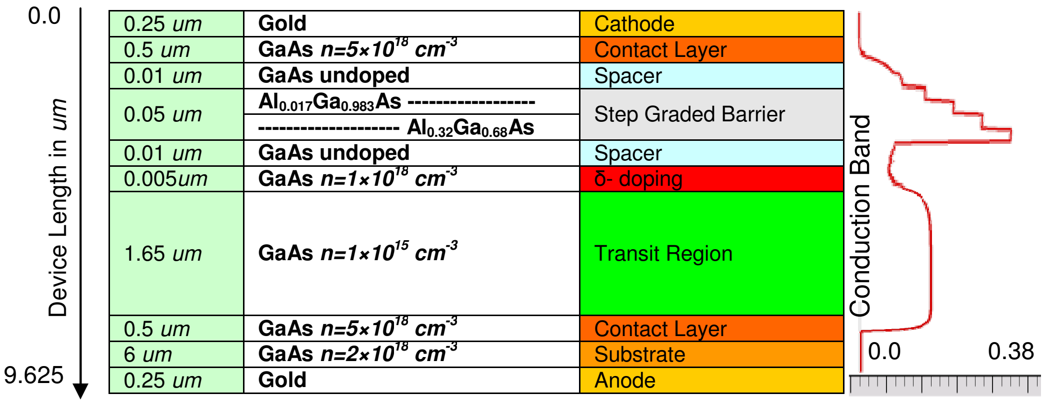

0.25 *um*	**Gold**	Cathode
0.5 *um*	**GaAs** $n=5\times10^{18}$ cm^{-3}	Contact Layer
0.01 *um*	**GaAs undoped**	Spacer
0.05 *um*	**$Al_{0.017}Ga_{0.983}As$ ------------------** **-------------------- $Al_{0.32}Ga_{0.68}As$**	Step Graded Barrier
0.01 *um*	**GaAs undoped**	Spacer
0.005*um*	**GaAs** $n=1\times10^{18}$ cm^{-3}	δ- doping
1.65 *um*	**GaAs** $n=1\times10^{15}$ cm^{-3}	Transit Region
0.5 *um*	**GaAs** $n=5\times10^{18}$ cm^{-3}	Contact Layer
6 *um*	**GaAs** $n=2\times10^{18}$ cm^{-3}	Substrate
0.25 *um*	**Gold**	Anode

Fig. 6.4 **77 GHz Gunn advanced step graded injector Gunn Diode structure**

6.2.2 Gunn Diode 2D Model

A 2D model of the structure was made in DevEdit^{TM} through definition of fourteen regions shown in Fig. 6.5 and 6.6. The regions were defined using the click and drag option provided by DevEdit^{TM}, before the individual material properties were defined for each region.

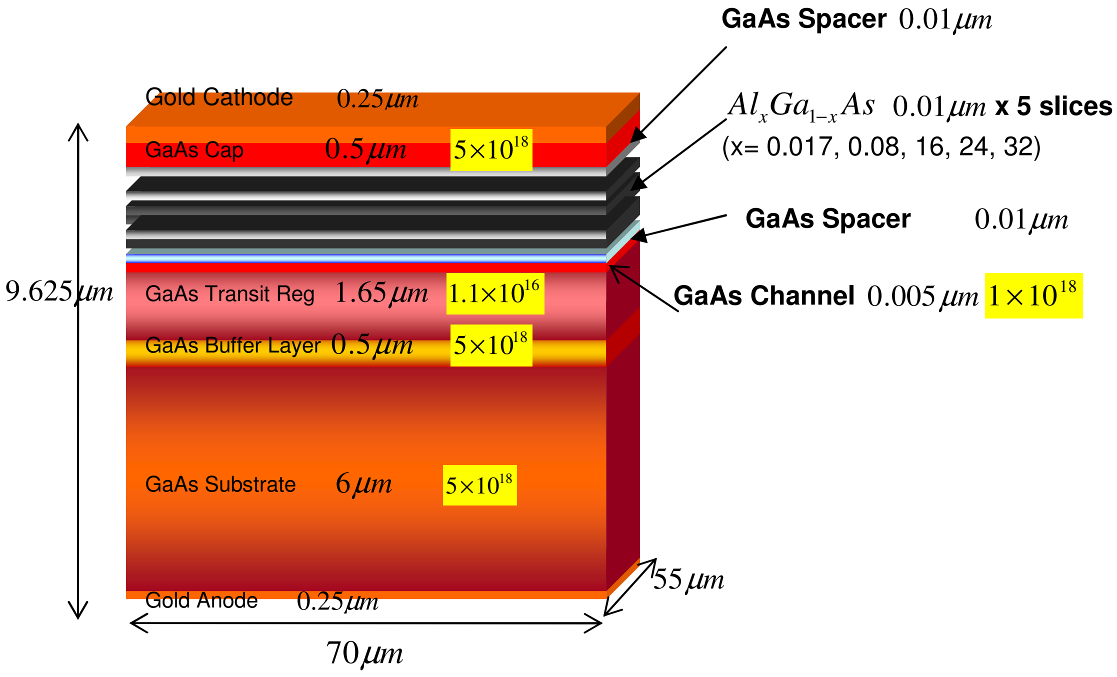

Fig. 6.5 **Graded Gap Heterostructure Gun Diode**

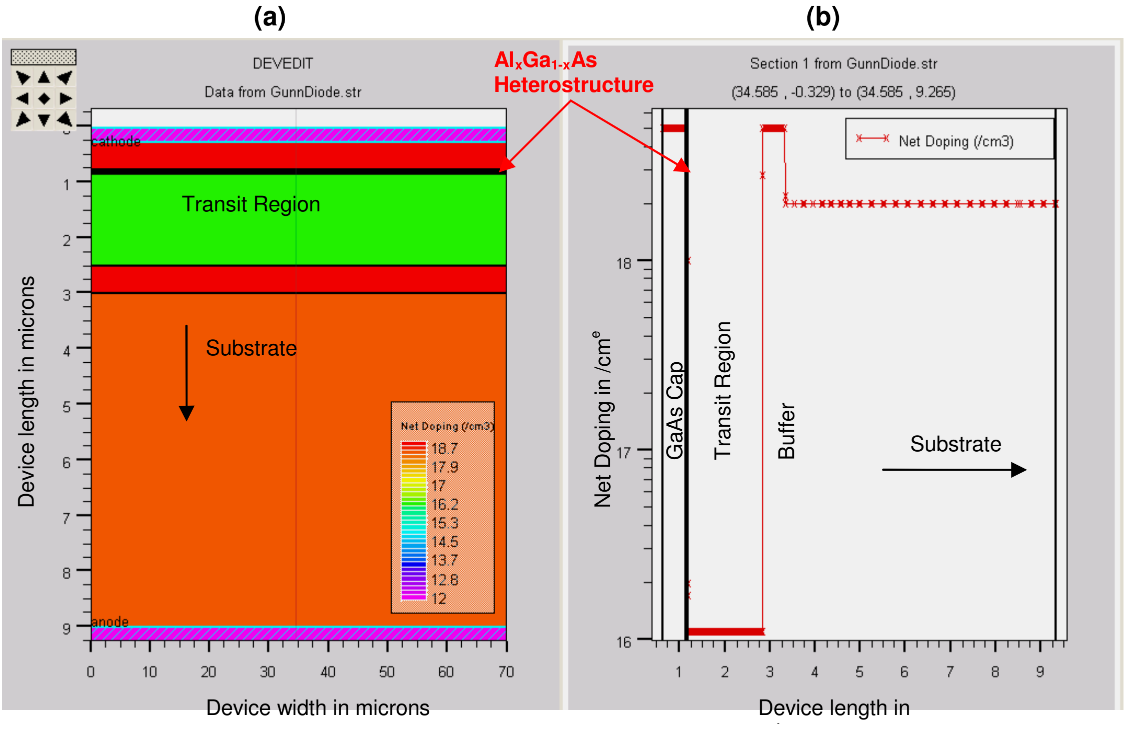
(a)

(b)

Fig. 6.6 **TonyPlot™ of modelled device structure showing impurity doping profile (a) Device planar view (b) Device cross section view**

Initially a default mesh was created throughout the model. An appropriate mesh density then needs to be identified as too dense a mesh results in unfeasibly slow device simulation and too coarse a mesh led to inaccurate simulation results. In view of the importance of mesh density, it was optimized using various options. In the beginning, the mesh *refine* option was used from the DevEdit^{TM} tool bar. Although a dense mesh was achieved the number of triangles exceeded 18,000 and as a result the DeckBuild^{TM} possessing time increased enormously. The mesh was then refined in selected regions such as all the AlGaAs regions, the doping spike and the transit region. Although this modified mesh provided adequate simulations results, impurity mixing in the small regions such as the doping spike and spacer were observed presumably due to lower number of triangles leading to overlapping of the regional interfaces. This problem was addressed by removing the mesh refine statement from the code and instead using mesh *constraint* [83]. The meshes created using the *refine* and *constraint* options are shown in Fig. 6.7 where it can be seen that the latter option provided an improved and denser mesh whilst allowing for an acceptable simulation time.

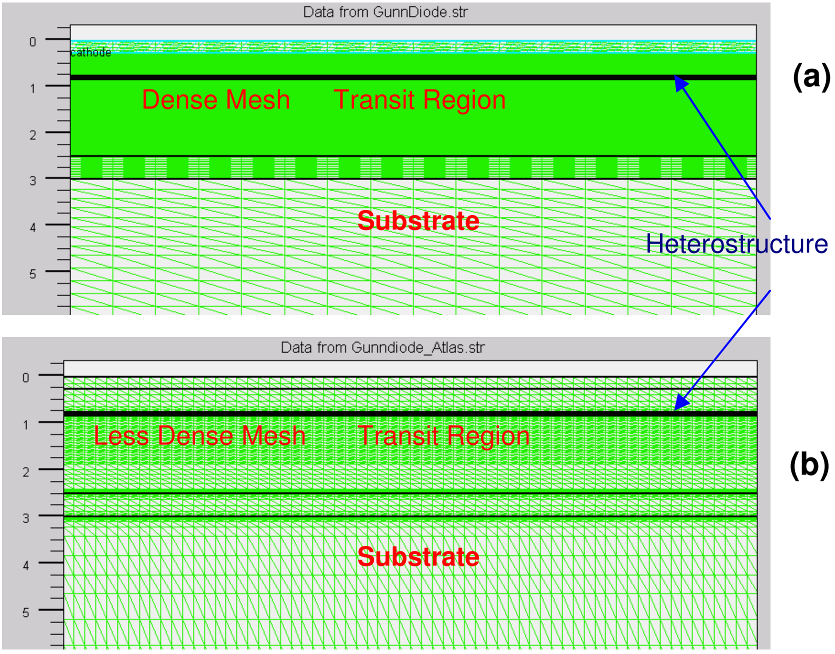

Fig. 6.7 Device structure with mesh density defined (a) using 'constraint' (b) using 'refine', plotted in TonyPlot^{TM}

The resulting conduction band diagram in the AlGaAs region for both meshes is shown in Fig. 6.8. It can be seen that the mesh with constraints applied provided a large number of triangles even in the smallest region, thus yielding a more realistic conduction band diagram.

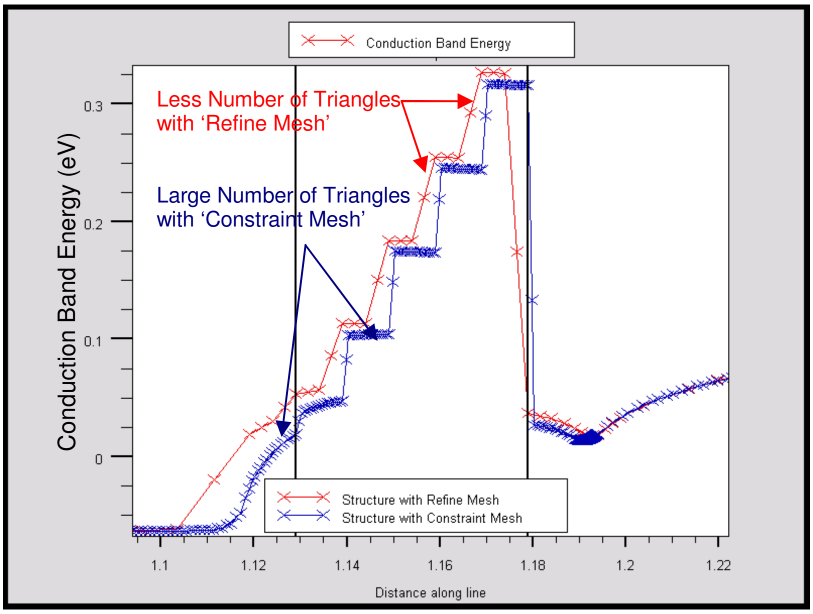

Fig. 6.8 Conduction band comparative data showing two models with course and dense meshing in the step-graded launcher

The device structure can also be defined in DeckBuild^{TM} through the ATLAS^{TM} command line. The command line codes were written to create 3D rectangular and cylindrical structures. The structures were created in an order of four distinct set of commands. The initial mesh was defined with a set of horizontal (x.mesh) and vertical (y.mesh) meshes with specific spacing between them. The mesh spacing was defined using parameter *spac*. After specifying meshes, the regions and materials were assigned. The electrodes and doping in the regions followed. Finally the structure was saved and simulated in DeckBuild^{TM}.

During initial model development, convergence issues were experienced which were attributed to meshes, material parameters and models definition. After improving models and material parameters, the convergence problem was narrowed down to number of meshes in regions such as the hot electron injector (AlGaAs launcher and doping spike regions) and the transit region. Subsequently, spacing between the meshes was reduced beyond SILVACO^{TM} recommended maximum number. It was achieved by using *spac,* which created a very dense mesh especially in the hot electron injector and the transit region. The number of meshes exceeded 100,000 against 18,000 limit imposed by the software. Despite greater number of meshes the memory allocation failure error message was not flagged and instead convergence issues were resolved. Thus for all further model developments including sub-micron transit region length models and with cylindrical geometry, ATLAS^{TM} command line was used to define modelled device structures.

6.2.3 2D Model with Heat Sink

Giga, a self heating simulator available in SILVACO^{TM}, was used to simulate the device's lattice heating effects. Giga was used with the definition of heat sinks at the cathode and anode respectively. Their dimensions were kept in accordance with a fabricated device for 77 GHz autonomous cruise control systems at e2v Technologies Plc. The device mesh structure with heat sinks is shown in Fig. 6.9.

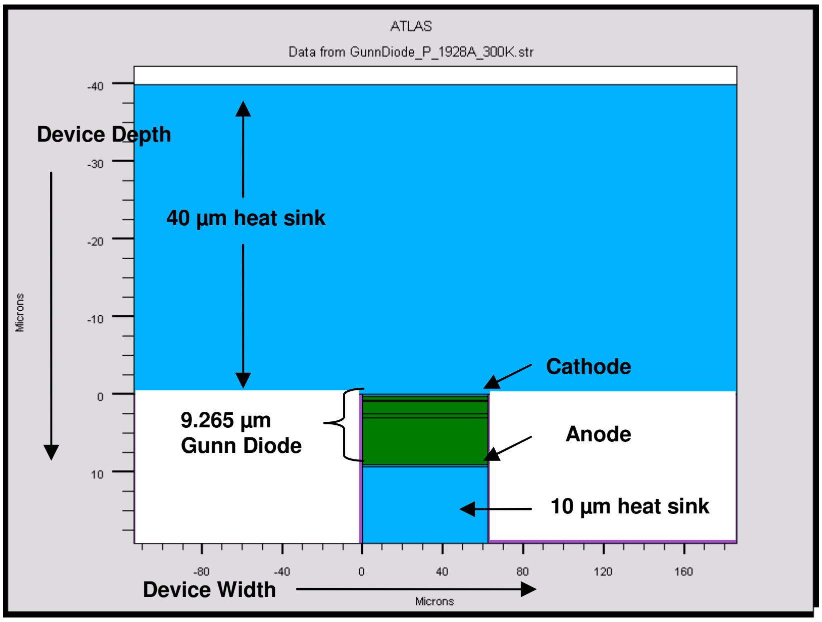

Fig. 6.9 **Modelled device structure with heat sinks**

The final DevEdit^{TM} structure file was then exported to DeckBuild^{TM}. The DeckBuild^{TM} code comprised of two sections: the device structure section and a coding section which defines the material parameters, model definition, methods and bias conditions. Bias was applied before the start of device simulation, which was achieved using ATLAS^{TM} by initializing the device under zero biased condition. The zero biased data obtained was then saved for subsequent I-V simulations. The device DC response was determined to study the device I-V characteristics. TonyPlot^{TM} was used to display the device simulation results. The log files and device structure files, created by DeckBuild^{TM}, were saved and subsequently plotted with TonyPlot^{TM} for analysis [82-84].

6.2.4 3D Rectangular Model Development

The 2D device structure was redefined in DeckBuild^{TM} with a third dimension. The 'z' dimension was defined while keeping the device area similar to the fabricated device. Fig. 6.10 – 6.11 shows the 3D device structure, where it can be seen that device layers are in the y-axis and its width in the z-axis. Blaze3D (a variant of Blaze2D which accounts for third dimension) was used to simulate the 3D device structure.

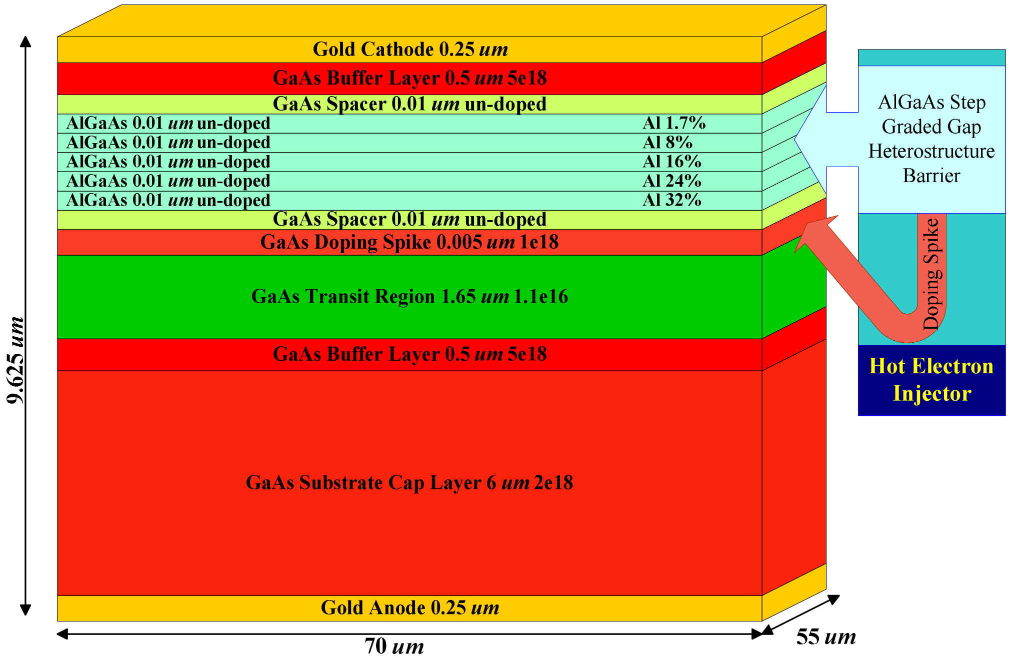

Fig. 6.10 3D rectangular model epitaxial structure

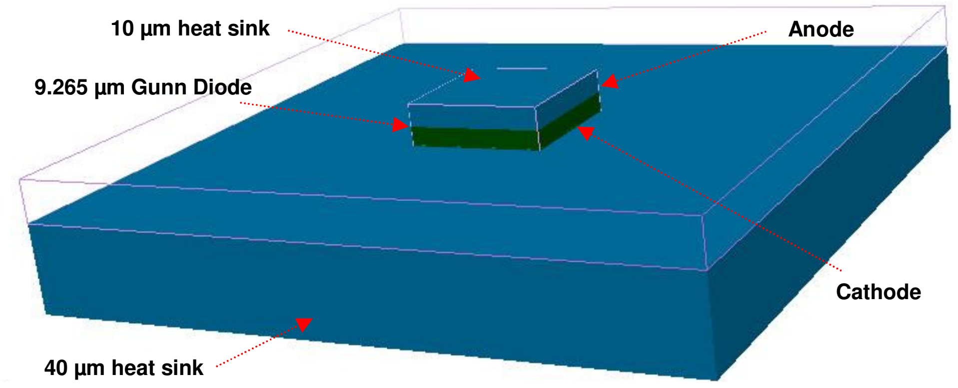

Fig. 6.11 **3D rectangular modelled device structure with heat sinks**

6.2.5 3D Cylindrical Model Development

A novel 3D cylindrical model structure has also been developed in DevEdit3D^{TM} to accurately reflect the cylindrical geometry of a fabricated device. This cylindrical model is shown in Fig. 6.12.

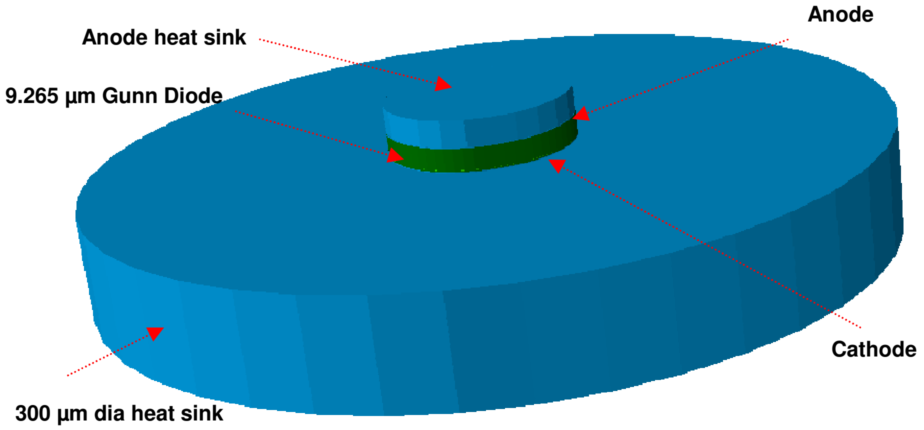

Fig. 6.12 **3D cylindrical modelled device structure with heat sinks**

6.3 Initial Device Solution

The initial solution for a given model, on which subsequent simulation iterations are based, is obtained at a bias condition of zero volts. This is because in ATLAS^{TM} the initial values for internal potential and carrier concentration are based on the device's doping profile. Through use of the *solve init* statement the initial response is calculated and saved as the device structure file shown in Fig. 6.13. This plot shows electron concentration through the device and on the left side a *display bar* shows the other options that are available for display in the device cross section view. By default the display bar only provides the doping concentration. However, with the addition of the *output* statement after the *models* statement in DeckBuild^{TM}, other options such as electric field, electron mobility, electron temperature, electron velocity, conduction band and valence band profile, and charge and current flow lines can also be plotted in the device cross section view.

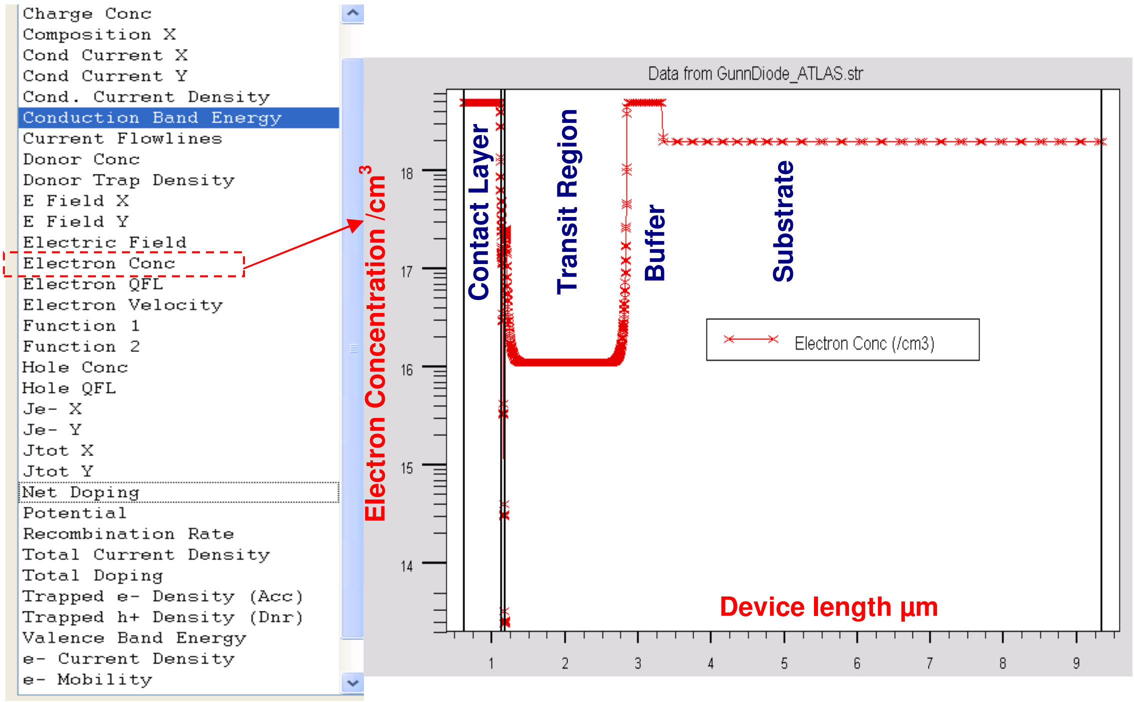

Fig. 6.13 **Device model structure cross section view plotted in TonyPlot^{TM}**

After determining initial device solution, DC simulations and device transient response was obtained as discussed below;

6.3.1 DC Simulation Results

The DC solution was obtained in DeckBuild^{TM} using the *solve* statement. The anode voltage was ramped from 0 to 4 volts with a step size of 0.1V. The file was then saved and plotted to provide the I-V curve shown in Fig. 6.14, which shows the start of the negative differential mobility region. The DC solution beyond 4V could not be achieved due to convergence problems that were later, resolved for transient simulations. However, it did provide the critical current at the onset of NDR.

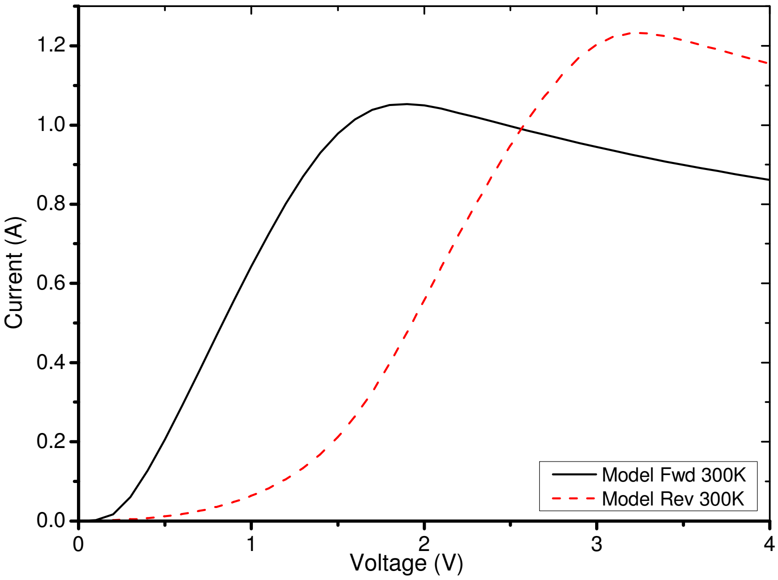

Fig. 6.14 Model forward-reverse asymmetrical I-V characteristics

During reverse bias simulations the anode voltage was ramped from 0 to -4V with a step size of -0.1V. The resulting I-V curve is also shown in Fig. 6.14 and has been plotted on the positive axis for better visualization.

The modelled device's asymmetrical I-V response indicates the successful incorporation of the injector and matches published data and the basic theory discussed previously.

6.3.2 Transient solutions

Transient solutions are used to obtain a time domain response such as determining the device oscillating frequency in biased condition. In the Gunn diode transient solutions for a linear ramp is obtained by specifying parameters such as *TSTART*, *RAMPTIME*, *TSTOP* and *TSTEP* as shown in Fig. 6.15 [81]. The *TSTART* specifies the linear ramp start time, *RAMPTIME* specifies the time that the linear ramp takes to achieve the final value, the solution is then stopped at *TSTOP* and the initial step size is specified by *TSTEP* shown in Fig. 6.15.

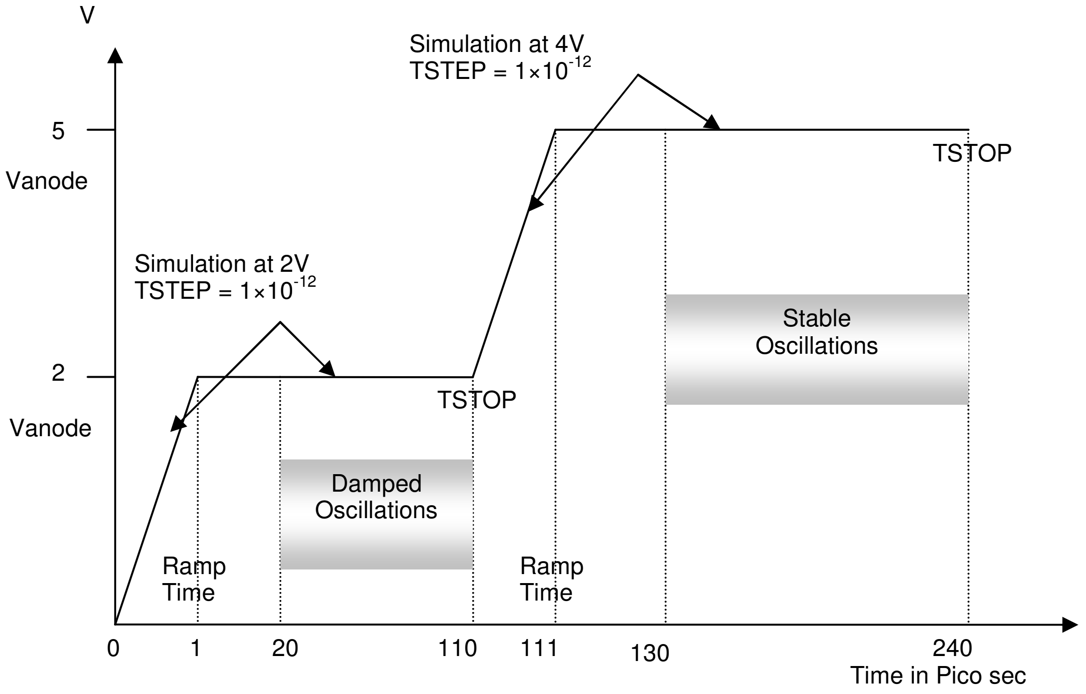

Fig. 6.15 **Device model transient voltage ramp in ATLAS™**

The transient response is saved in the *log* file and subsequently, *extract* statements are used to determine the maximum current value on y-axis and its corresponding voltage on the x-axis. Finally the I-V curve for the transient response is plotted using TonyPlot™.

6.3.3 Transient Response – free running oscillations

The 2D models with heat sinks and associated cavity time domain simulations are discussed in chapter 8. The transient response presented here is that of a 77 GHz second harmonic Gunn 2D model without using the self heating simulator, GIGA, and with no cavity. It was performed to extract the critical current, the damping and final oscillating frequencies as shown in Fig. 6.16 - 6.18. The model was simulated at 2V applied bias to determine the current at the onset of negative differential resistance. The extracted current plot in Amps is shown in

Fig. 6.16, which depends on the model width as discussed earlier. The first damping oscillating transient response is shown in Fig. 6.17 and shows that the domain is not fully formed resulting in the damping transient response which eventually died down. The damping transient response although yielding very high frequency resulting in a power that was very low. Therefore, it was concluded that at the onset of negative differential resistance the applied potential and hence the field is not enough to sustain the domain.

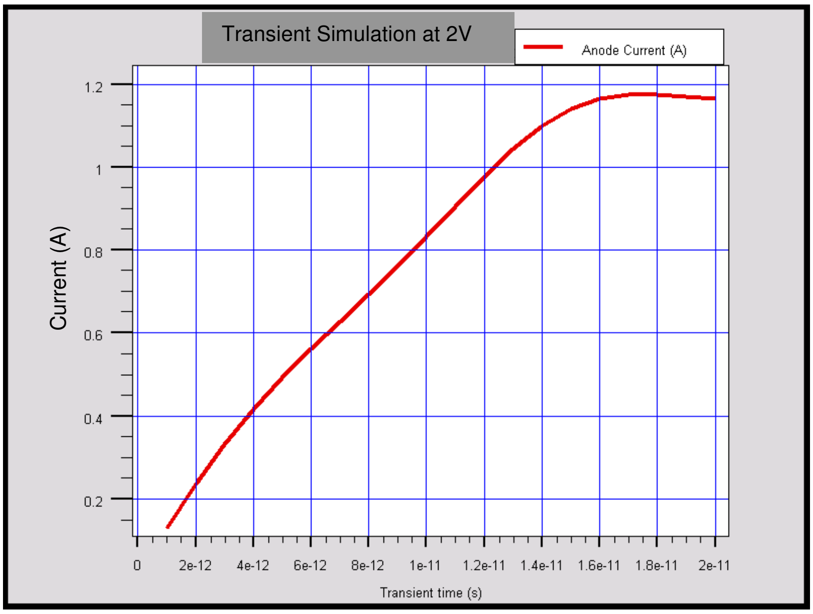

Fig. 6.16 **Transient response - critical current at 2V**

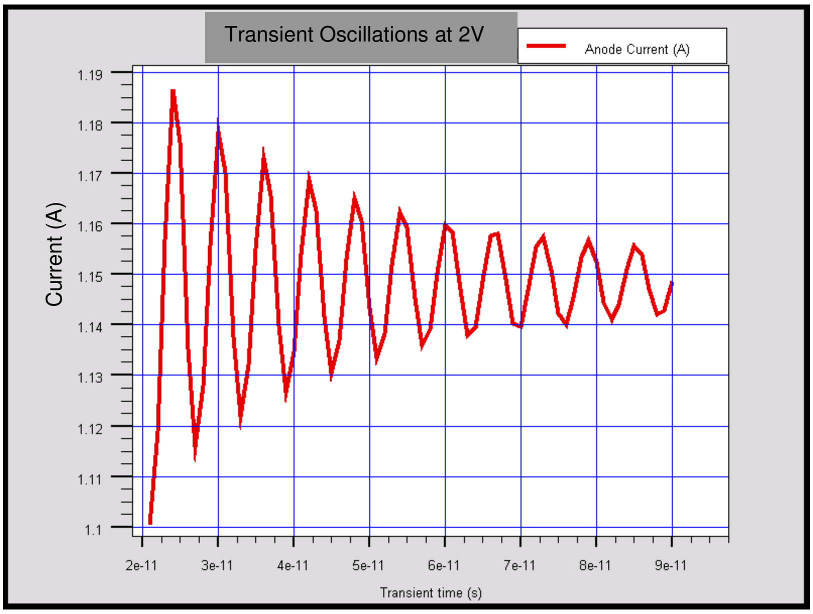

Fig. 6.17 **Transient response - damping frequency at 2V**

The applied bias was increased from 2 to 4 volts (representing a realistic device operating bias) and the transient response was determined as shown in Fig. 6.18. It can be seen that the domain is quenched during the RF cycle due to a decrease in terminal voltage below the sustaining voltage. A new domain at the cathode does not nucleate until the terminal voltage rises above the threshold value.

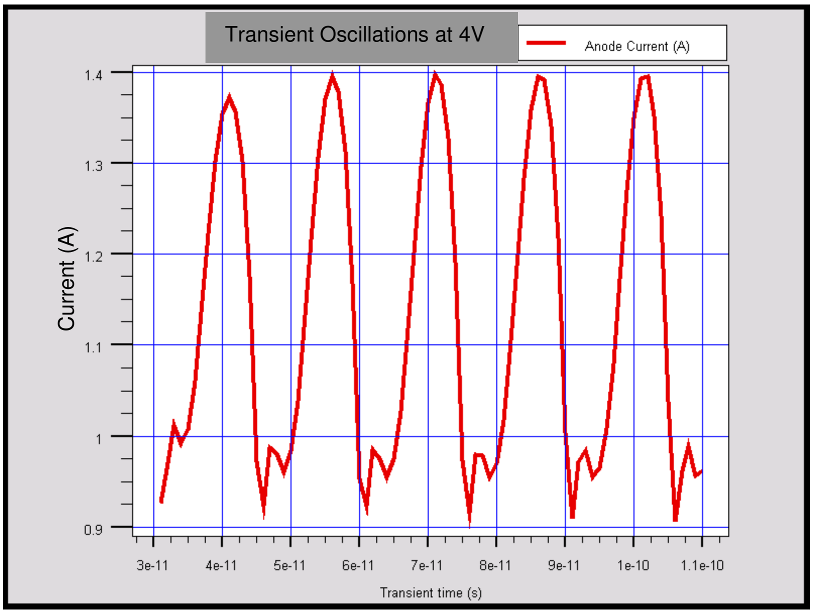

Fig. 6.18 **Transient response - stable oscillations at 4V**

6.4 Free-running frequency of oscillation

It has been shown [12] that weak oscillations will occur in a device biased at voltages below its turn on voltage and that these weak oscillations will be extremely noisy at low bias voltages due to the excitation of numerous modes within the transit region (and a reduction in the level of coherence). As the external bias is increased the level of coherence also increases due to the larger high-field domains reducing the overall internal electric field in the transit region and so preventing multiple modes propagating. In addition, as the external bias voltage increases the oscillation frequency decreases and the RF power increases. At the threshold (turn on) voltage, the RF power locks onto a single frequency defined by the resonant oscillator circuit and a highly coherent output is observed.

These effects are illustrated in Fig. 6.19 which shows the onset of oscillation, region of weak oscillation, and turn on voltage of two GaAs Gunn devices. The plot is taken from [12] and was produced using Monte Carlo simulations of the free running frequency of GaAs Gunn devices with and without hot-electron injection (it is noted that the power curve is based on measured values and that the simulations did not include consideration of an oscillator circuit). This shows that the free-running frequency of oscillation is reduced as the external field is increased, meaning that the oscillation frequency of the simulated time-domain response is typically expected to be higher than that measured from an oscillator circuit. It also shows that the capability of a device to support sustained oscillation can be established from simulation of the model at low bias voltages. The majority of the time-domain simulations were therefore carried out at two bias voltages: a low voltage (typically about 2 volts) to establish whether the device was capable of producing sustained oscillations and, where possible, a higher voltage (about 4 volts) to study the behaviour of the device under realistic operating conditions.

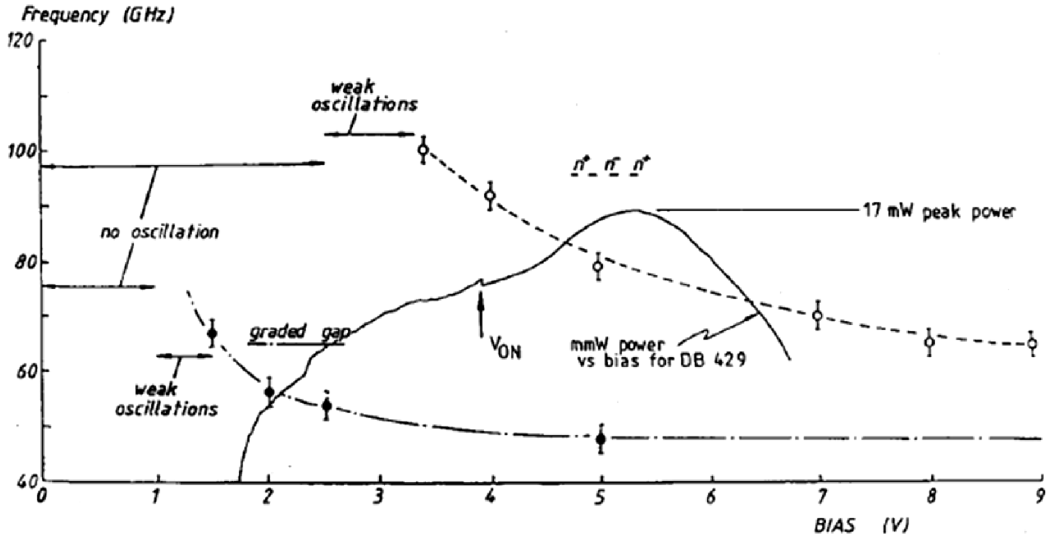

Fig. 6.19 Monte Carlo simulation results for GaAs Gunn diodes with and without hot electron injection. It is noted that the power curve is taken from measurements of a typical device with hot electron injection, and that an oscillator circuit was not included in the simulation [12].

6.5 Conclusion

A step-by-step process has been discussed to develop a physical model in SILVACO^{TM} VWF^{TM} environment using ATLAS^{TM} as the core tool. It was shown that in the ATLAS^{TM} program flow, the order in which statements are defined is crucial. The five groups of statements and their order was presented. Development of the physical model was presented for a state of art GaAs Gunn diode with a step graded AlGaAs hot electron injector. It includes 2D model, 2D model with heat sink, 3D rectangular model and a novel 3D cylindrical model developed for a 77GHz second harmonic graded gap injector Gunn diode.

It was shown that convergence issues were resolved by improving physical models, selecting correct material parameters and refining meshes in regions such as hot electron injector and transit region. The spacing between the meshes was reduced beyond SILVACO^{TM} recommended number by using *spac,* which created a very dense mesh. The number of meshes exceeded 100,000 against 18,000 limit imposed by the software. Despite greater number of meshes the memory allocation failure error message was not flagged. For all further model developments including sub-micron transit region length models and with cylindrical geometry, ATLAS^{TM} command line was used with *spac* defined.

The modelled device initial solution, DC simulations and transient responses were presented that are discussed in chapters 8 and 9. The modelled device's asymmetrical I-V response indicated the successful incorporation of the injector. The transient response presented is that of a 77 GHz second harmonic Gunn 2D model without using the self heating simulator, GIGA, and with no cavity. It was performed to extract the critical current, the damping and final oscillating frequencies. The model was simulated at 2V applied bias to determine the current at the onset of negative differential resistance. The first damping oscillating transient response, at 2V applied bias, showed that the domain was not fully formed resulting in the damping transient response which eventually died down. It was concluded that at the onset of negative differential resistance the applied potential and hence the field is not enough to sustain the domain. The applied bias was increased from 2 to 4 volts (representing a realistic device operating bias) and the transient response was determined. It was shown that the domain was quenched during the RF cycle due to a decrease in terminal voltage below the sustaining voltage.

Finally free running frequency of oscillation was discussed. It was shown that the free-running frequency of oscillation is reduced as the external field is increased, meaning that the oscillation frequency of the simulated time-domain response is typically expected to be higher than that measured from an oscillator circuit. It was also shown that the capability of a device to support sustained oscillation could be established from simulation of the model at low bias voltages.

Chapter 7 Physical Models

7.1 Physical Models Used for Device Simulation

The accuracy of the simulated response depends on the choice of material parameters and the selection of physical models (and their associated parameters) used. The material and model parameters used were therefore extensively researched from a variety of sources [3, 29, 65, 85, 86]. Where the platform did not allow sufficient flexibility to accurately account for the interdependency of parameters, appropriate C-language functions were written and incorporated through the in-built C-interpreter [81, 83].

The analytic function based on the work of Caughey and Thomas [87] is used for modelling field dependant mobility in the contact layers, spacer layers, AlGaAs launcher and also the transit region for field strengths below the negative differential mobility (NDM) threshold. For field strengths in the transit region above the NDM threshold, the Barnes NDM model [88] is used. The Shockley-Read-Hall (SRH) recombination model [89, 90] is applied in the nominally undoped $Al_xGa_{(1-x)}As$ barrier. The SRH concentration-dependent lifetime model [89] is used in the rest of the device to account for the varied silicon impurity concentrations.

For local temperature, self-heating, lattice heat flow and heatsinking effects, Giga [81], the ATLAS^{TM} non-isothermal device modeller module is used. This is based on the models suggested by Wachutka [91] and accounts for Joule heating along with heating and cooling due to carrier generation and recombination.

The models used for each material i.e. GaAs and AlGaAs are listed in table 7.1 and are discussed in detail [81]:

Material	**Physical Models**	
GaAs	Mobility	**Conmob** – (Concentration Based Mobility)
		Analytic – (Caughey Thomas)
		Fldmob evsatmod=1 b.elec=2 – (Field Dependent Mobility with NDR)
	Recombination	**Consrh** – (SRH Concentration-Dependent Lifetime model)
	Carrier Statistics and transport	**Boltzmann** – (Boltzmann Approximation) **Temperature=300** – (device lattice temperature at 0 bias)
AlGaAs	Recombination	**SRH** – (Shockley-Read-Hall)
	Mobility	**Fldmob evsatmod=0 b.elec=2** – (Field Dependent Mobility without NDR)
GaAs and AlGaAs	Carrier Statistics and transport	**Boltzmann** – (Boltzmann Approximation) **Temperature=300** – (device lattice temperature at 0 bias)
		hcte.el – (Hydrodynamic model for electrons)
	GIGA	**lat.temp** - (Lattice Heat Flow Equation) **e.taur.var** - (Electron energy relaxation time)
Heat Sinks	Anode and Cathode	**GIGA** - self heating simulator defined to simulate lattice heating effects as a function of applied voltage.

Table 7.1 Physical models summary

7.2 Mobility Models Used

In the Gunn diode, as in other electron carrier devices, the electrons are accelerated by the electric field. However, they lose momentum due to numerous microscopic scattering processes. These microscopic phenomena are lumped into macroscopic mobilities, which are included by the mobility and transport equations during device modelling. The mobility equations used for the Gunn diode model in the low and high electric field regions will be discussed individually.

The carriers are almost in equilibrium with the lattice at low field values and so the electron mobility v_{n0} has a characteristic low-field value. This low-field value depends on the phonon and impurity scattering that affects (decreasing its value). However, the carriers are no longer in equilibrium at high electric fields and are therefore subjected to a wider range of scattering processes. Therefore, at high electric fields the drift velocity no longer increases linearly and becomes saturated or decreases, which is termed as saturation velocity ($v_{sat}{}^{n}$). These effects must obviously be accounted for using the appropriate models [81]. ATLAS^{TM} and its sub-engine Blaze provide various low-field and high-field models that can be used depending on the device and its operation. The models used for the simulations will now be discussed.

7.2.1 Low field Mobility Models

Suitable low field models for the simulation were carefully selected. Five distinctive models and conditions are available in ATLAS^{TM} to define the low field electrical mobility in GaAs and AlGaAs [81]:

- The low-field mobility parameter 'MUN'(cm^2/V.s), can be defined from the ATLAS^{TM} lookup table. The value is defined in the mobility statement for each region.
- The concentration based mobility model 'CONMOB' can be used. The values for low field mobility at 300K are found from the ATLAS^{TM} look-up table for the doping concentration in each region.
- In order to relate the low field electron mobility with impurity concentration and temperature, the 'ANALYTIC' and 'ARORA', may be used.
- A carrier-carrier scattering model (CCSMOB), which relates the low field mobility to both carrier concentration and temperature can be used.

- Using the unified low field mobility model (KLAASSEN). This model relates the low field mobility to lattice, carrier-carrier, donor scattering, and temperature.

7.2.2 AlGaAs Default Low field Mobility Model

For the un-doped $Al_xGa_{1-x}As$ regions the *Constant Low Field Mobility* model was used which is independent of the doping concentration, carrier densities and electric field. The electron mobility values in this model are determined using the following formula:

$$v_{n0} = M_{UN}\left(\frac{T_L}{300}\right)^{-T_{MUN}} \quad \text{...(7.1)}$$

where T_L is the lattice temperature in degrees Kelvin, M_{UN} is the undoped mobility value in $cm^2/Vsec$ and T_{MUN} is the temperature dependent coefficient whose value is taken from the SILVACO^{TM} lookup table ($T_{MUN}=1.5$) [81]. These parameters are specified in the material statement as shown in table 7.2. The simulations were performed at $T_L = 300K$ which resulted in an electron mobility equal to the undoped mobility value (M_{UN}) defined for each Al concentration. The temperature dependent co-efficient T_{MUN} was ignored. The AlGaAs mobility values (M_{UN}), which were defined separately for each AlGaAs region due to dependability on the Al concentration, are shown in table 7.2 [81].

$Al_xGa_{1-x}As$ Region	**Statement Code**
x=0.017	mobility region=11 mun=4700
x=0.08	mobility region=10 mun=4300
x=0.16	mobility region=9 mun=3400
x=0.24	mobility region=8 mun=2400
x=0.32	mobility region=7 mun=800

Table 7.2 Mobility values for $Al_xGa_{1-x}As$ regions [52]

7.2.3 GaAs Concentration Dependent Low Field Mobility Model

For a doped GaAs region the electron mobility depends on the impurity levels in each region alongwith the operating temperature. The Concentration Based Mobility *conmob* was therefore defined for all GaAs regions. The SILVACO^{TM} default library has built in values for all GaAs concentration values at 300*K*. And this default data was used during the simulations. To take into account temperature effects on the electron mobility the *analytic* model was used which allowed the temperature to be varied from 77 to 450*K*.

7.2.4 GaAs Analytic Low Field Mobility Model

The Caughey Thomas *Analytic Low Field Mobility* model [87] was used for the GaAs regions. The model was used to specify doping and temperature dependent low field mobilities using the following equation:

$$v_{n0} = M_{CAUG}^{U1N}\left(\frac{T_L}{300}\right)^{\alpha_{CAUG}} + \frac{M_{CAUG}^{U2N}\left(\frac{T_L}{300}\right)^{\beta_{CAUG}} - M_{CAUG}^{U1N}\left(\frac{T_L}{300}\right)^{\alpha_{CAUG}}}{1+\left(\frac{T_L}{300}\right)^{\Gamma_{CAUG}}\cdot\left(\frac{N}{N_{CAUG}^{CRITN}}\right)^{\Delta_{CAUG}}} \quad \textit{cm}^2\textit{/V.sec}\ldots(7.2)$$

A description of the parameters used in equation 7.2 along with their values is shown in table 7.3. The model is activated by defining both *conmob* and *analytic* in the *models* statement.

The default mobility values for M_{CAUG}^{U1N} and M_{CAUG}^{U2N} were used for all GaAs regions except the transit region, where the parameters were defined to achieve the 6300 *cm^2/V.sec* [88], which was achieved through iterative simulations. Optimised values for the mobilities at highest and lowest Al concentrations were found as $M_{CAUG}^{U1N}=940$ and $M_{CAUG}^{U1N}=8685$ respectively, which were used for subsequent simulations. The temperature dependent fitting parameters α_{CAUG}, β_{CAUG} and Γ_{CAUG} were defined using the C-interpreter function. The default value for Δ_{CAUG} was kept as 1 to account for the increasing concentration effect on the electron mobility [81].

Parameter	Description	Value	Units
M_{CAUG}^{U1N}	Mobility at highest concentration value, depends on impurity doping	-	*cm²/Vsec*
M_{CAUG}^{U2N}	Mobility at lowest concentration. Depends on impurity doping	-	*cm²/Vsec*
α_{CAUG}	Temperature dependent fitting parameters	0	Arbitrary
β_{CAUG}	Temperature dependent fitting parameters	0	Arbitrary
Γ_{CAUG}	Temperature dependent fitting parameters	0	Arbitrary
Δ_{CAUG}	Temperature dependent fitting parameters	1	Arbitrary
N_{CAUG}^{CRITN}	Caughey Thomas critical concentration level	2.8×10^{16}	cm^{-3}
N	Impurity concentration defined for individual region	-	cm^{-3}
T_L	Temperature	300	K

Table 7.3 Caughey Thomas Analytic Low Field mobility model parameters (300K) [87]

7.2.5 Parallel Electric Field Dependent Mobility Model

Two types of electric field dependent mobility (*fldmob*) models are available in ATLAS^{TM}. The models are named as the *Standard Mobility* model and *Negative Differential Mobility* model, both of which contain appropriate default parameter values for different materials. The models are defined by specifying *evsatmod* along with the *fldmob* in the models statement. The *evsatmod* specifies which parallel field dependent mobility model should be used for electrons, which are defined as [81]:

- evsatmod=0 allows the application of standard Mobility model
- evsatmod=1 implements the GaAs negative differential mobility saturation model.

- evsatmod=2 implements the simplified field dependent velocity model. The standard electric field based mobility model is applied and the temperature dependent mobility is not used.

The standard mobility model was used for AlGaAs step graded heterostructure region. The standard mobility model is defined in terms of electron saturation velocity, which is a function of applied electric field. The model is implemented in ATLAS^{TM} using the following Caughey Thomas expression, which provides a smooth transition between low-field and high field behaviour [87]:

$$v_n(E) = v_{n0}\left[\frac{1}{1+\left(\frac{v_n E}{v_{satn}}\right)^{\beta n}}\right]^{1/\beta n} \quad \text{...(7.3)}$$

where, v_{satn} is the electron saturation velocity, βn is a constant whose value for both AlGaAs / GaAs and was taken as 1 from the SILVACO^{TM} reference tables. The low field electron mobility, v_{n0}, is determined from equations 7.1 and 7.2 for AlGaAs and GaAs respectively. A similar equation for holes is also available but has not been used, since holes do not play any role in the simulations due to n^+ dopant use.

The Barnes Negative Differential Mobility model [88] was used in the transit region at high electric filed. The electron saturation velocity, as a function of electric field, is given by:

$$v_n(E) = \frac{v_{n0} + \frac{v_{satn}}{E}\left(\frac{E}{E_{CRIT}^{N}}\right)^{\Gamma_N}}{1+\left(\frac{E}{E_{CRIT}^{N}}\right)^{\Gamma_N}} \quad \text{...(7.4)}$$

where v_{satn} is the electron saturation velocity, v_{n0} is the low field electron mobility, E_{CRIT}^{N} is the critical electric field in V/cm, Γ_N is a constant equal to 2 for GaAs and E is the electric field. The critical electric field for GaAs was defined as $E_{CRIT}^{N} = 3.4\times10^{3}$.

It should be noted here that for both standard and negative differential mobility models, an empirical temperature dependent saturation velocity for GaAs is implemented as:

$$v_{satn} = 11.3\times10^{6} - 1.2\times10^{4} T_L \quad cm/s \text{ ……………………..…………(7.5)}$$

where, T_L is the temperature in degree Kelvin. For the device model simulated at *300K,* a GaAs saturation velocity value of $7.7\times10^{6} cm/s$ was used during device simulations.

7.3 Carrier Generation – Recombination Models

The processes responsible for carrier generation and recombination fall under following six main categories:

- Phonon transitions
- Photon transitions
- Auger transitions
- Surface recombination
- Impact ionization
- Tunnelling

In ATLAS^{TM} this six generation-recombination mechanisms are represented using different models. For Gunn diode modelling, the Shockley-Read-Hall (SRH) recombination (phonon Transition) and SRH Concentration-Dependent Lifetime (Photon Transition) models have been used for AlGaAs and GaAs regions respectively as listed in table 7.1.

7.3.1 Shockley-Read-Hall (SRH) Recombination

Phonon transition within a semiconductor is due to a trap or defect within its forbidden gap. The theory of phonon transition was discovered first by Shockley and Read [89], and then later by Hall [90]. The Shockley-Read-Hall (SRH) recombination model was used for the AlGaAs regions and implemented as:

$$R_{SRH} = \frac{pn - n_{ie}^{2}}{\tau_{P0}\left[n + n_{ie}\exp\left(\frac{\mathrm{E}_{TRAP}}{kT_L}\right)\right] + \tau_{N0}\left[p + n_{ie}\exp\left(\frac{-\mathrm{E}_{TRAP}}{kT_L}\right)\right]} \quad \text{........(7.6)}$$

where τ_{N0} and τ_{P0} are the electron and hole life times, which were defined for each individual $\mathrm{Al_xGa_{1-x}As}$ region. The values were calculated using the virtual crystal approximation formula for both GaAs and AlAs. The values for these materials were taken from the SILVACO^{TM} reference tables. E_{TRAP} indicates the trap energy and intrinsic Fermi level difference in electron volts. Its default value $(ETRAP = 0)$ was used to correspond to efficient recombination of one trap layer present in the material. T_L is the lattice temperature in degrees Kelvin. The model was activated by defining *srh* in the model statement for the AlGaAs region.

7.3.2 SRH Concentration-Dependent Lifetime model

The concentration based SRH model was used for the GaAs regions due to the different impurity concentration level in each. The modified SRH model with carrier life time as a function of doping concentration is implemented in ATLAS^{TM} [81, 92] as follows:

$$R_{SRH} = \frac{pn - n_{ie}^{2}}{\tau_{P}\left[n + n_{ie}\exp\left(\frac{\mathrm{E}_{TRAP}}{kT_L}\right)\right] + \tau_{n}\left[p + n_{ie}\exp\left(\frac{-\mathrm{E}_{TRAP}}{kT_L}\right)\right]} \quad \text{.......... (7.7)}$$

where

$$\tau_P = \frac{\tau_{P0}}{AP + BP\left(\frac{N_{total}}{N_{SRH}^{P}}\right) + CN\left(\frac{N_{total}}{N_{SRH}^{P}}\right)^{EP}} \quad \text{...(7.8)}$$

$$\tau_n = \frac{\tau_{N0}}{AN + BN\left(\frac{N_{total}}{N_{SRH}^{N}}\right) + CN\left(\frac{N_{total}}{N_{SRH}^{N}}\right)^{EN}} \quad \text{...(7.9)}$$

Here, *N* is the carrier concentration level and the constant values *AN, BN* were taken from the SILVACO^{TM} reference tables. N_{SRH}^{N} and N_{SRH}^{P} are the SRH concentration levels for electrons and holes respectively. N_{total} is the total carrier concentration level. τ_{N0} and τ_{P0} are the electron and hole life times as discussed earlier. Most of these parameters are well defined for GaAs in the SILVACO^{TM} default library at 300K. And so the default values were used in the model [81].

7.4 Carrier Statistics and Transport

Within a semiconductor the thermal equilibrium of electrons at temperature T_L obeys Fermi-Dirac statistics. The electron occupation probability for a given energy, $f(\mathrm{E})$, is given as [81]:

$$f(\mathrm{E}) = \frac{1}{1+\exp\left(\dfrac{\mathrm{E}-\mathrm{E}_F}{KT_L}\right)} \quad \text{..(7.10)}$$

If $\mathrm{E}-\mathrm{E}_F >> KT_L$ (non-degeneracy) then the equation can be approximated as:

$$f(\mathrm{E}) = \exp\left(\frac{\mathrm{E}_F-\mathrm{E}}{KT_L}\right) \quad \text{..(7.11)}$$

The above approximation is known as the Boltzmann statistic. The Boltzmann approximation simplifies the calculations whilst yielding satisfactory results. It was used in the model that minimized convergence issues as compared to the Fermi-Dirac statistics. In ATLAS^{TM} the use of the Boltzmann statistic has been set at its default implementation [81].

The transport models, Drift Diffusion, energy balance and hydrodynamic models available in ATLAS^{TM} are discussed. In the Gunn diode model the carriers were selected as electrons. The electrons equations are presented only.

7.4.1 Drift Diffusion Model

The Drift Diffusion model is used as default in ATLAS^{TM} to model carrier transport or current density. It applies approximations and simplifications to the Boltzmann Transport Equation. It does not introduce any independent variable in addition to electrostatic potential and the electron concentration. This model although simple, ignores non-local transport effects such as velocity overshoot and diffusion due to carrier temperature. Resultantly, its accuracy decreases for sub micron devices. The current density $\vec{J}$ for electrons (n) is given as;

$$\overrightarrow{J_n} = q\mu_n n\vec{E} + qD_n\nabla n \qquad \text{...(7.12)}$$

where μ_n is the electron mobility, $\vec{E}$ is the local electric field in V/cm, D is the diffusion coefficient, which is calculated using Einstein's relationship as;

$$D_n = \frac{kT}{q}\mu_n \qquad \text{..(7.13)}$$

7.4.2 The Energy Balance and Hydrodynamic Transport Models

In ATLAS^{TM}, the energy balance and hydrodynamic transport models are available as current density non-local models. These models uses additional coupling of the current density to the carrier temperature. The Energy Balance Transport Model is derived from the Boltzmann Transport Equation using Stratton derivation [93, 94]. It is simplified by applying some assumptions into the hydrodynamic model [95-97].

Three energy balance transport equations for electrons comprising of energy balance equation, current density and energy flux are as follows;

$$\nabla.\vec{S}_n = \frac{1}{q}\vec{J}_n.\vec{E} - W_n - \frac{3k}{2}\frac{\delta}{\delta t}\left(\lambda_n^* n T_n\right) \qquad \text{...................................(7.14)}$$

$$\overrightarrow{J_n} = qD_n\nabla n - q\mu_n n\nabla\psi + qnD_n^T\nabla.T_n \qquad \text{....................................(7.15)}$$

$$\overrightarrow{S_n} = -K_{Bn}\vec{\nabla}Tn - \left(\frac{k\delta_n}{q}\right)\vec{J}_n T_n \qquad \text{..(7.16)}$$

The energy balance transport equations simplify into the hydrodynamic transport equations by substituting $\lambda_n^* = 1$ and $\delta_n = \frac{5}{2}$. The hydrodynamic transport equations are given as;

$$\nabla.\vec{S}_n = \frac{1}{q}\vec{J}_n.\vec{E} - W_n - \frac{3k}{2}\frac{\delta}{\delta t}\left(nT_n\right) \tag{7.17}$$

$$\overrightarrow{J_n} = qD_n \nabla n - q\mu_n n \nabla \psi + qnD_n^T \nabla T_n \tag{7.18}$$

$$\overrightarrow{S_n} = -K_{Bn}\vec{\nabla}T_n - \left(\frac{k}{q}.\frac{5}{2}\right)\vec{J}_n T_n \tag{7.19}$$

where,

$\overrightarrow{S_n}$ is the electron energy flux density

D_n is the thermal diffusion coefficient (equation 7.13)

W_n is the energy density loss rates for electrons (equation 7.29)

K_{Bn} is the thermal conductivity of electrons given as;

$$K_{Bn} = qn\mu_n \left(\frac{k}{q}\right)^2 T_n \tag{7.20}$$

The hydrodynamic model provides realistic results and better convergence. It was implemented in the Gunn diode model using parameter *hcte.el* on the models statement.

7.5 GIGA$^{\text{TM}}$ – Self Heating Simulator

Lattice heat flow and general thermal environment simulation in the model has been implemented using GIGA$^{\text{TM}}$, a self heating simulator, which extends ATLAS$^{\text{TM}}$ capabilities in the DeckBuild$^{\text{TM}}$ environment. GIGA$^{\text{TM}}$ is based on the models suggested by Wachutka [91], which precisely accounts for the Joule heating and heating and cooling due to carrier generation and recombination. Ambient temperature conditions, realistic heat-sinks and thermal impedances are also accounted for. Additionally, all the material and transport parameters defined for each region are made lattice temperature dependent throughout the model.

Statement	**Parameter**	**Details**
material	hc.comp	Heat Capacity model
	tcon.power	Thermal conductivity model
models	lat.temp	Lattice Heat Flow Equation
	e.taur.var	Electron energy relaxation time
thermcontact	ext.temper	Heat sink temperature
		Heat sink electrodes are defined with dimensions

Table 7.4 GIGA^{TM} – self heating simulator parameters

7.5.1 The Lattice Heat Flow Equation

GIGA^{TM} adds the following lattice heat flow equation to the primary equations that are solved by ATLAS^{TM}:

$$C\frac{\partial T}{\partial t} = \nabla\left(\kappa\nabla T_L\right) + H \quad \text{...(7.21)}$$

where,

C is the heat capacitance per volume

κ is the thermal conductivity

H is the heat generation

T_L is the local lattice temperature

The heat capacitance can also be defined as $C = \rho C_p$, where ρ is the density of material and C_p is the specific heat. The lattice heat flow equation is included during simulation by defining *lat.temp* parameter on the *models* statement.

7.5.2 Heat Capacity

The temperature dependent heat capacity for defined regions in a structure is modelled as [98];

$$C(T_L) = \rho \left[C_{300} + C_1 \frac{\left(\frac{T_L}{300}\right)^{\beta} - 1}{\left(\frac{T_L}{300}\right)^{\beta} + \frac{C_1}{C_{300}}} \right] \text{ (J/cm}^3\text{/K)} \quad \ldots\ldots\ldots\ldots\ldots\ldots\ldots(7.22)$$

where,

$C(T_L)$ is the temperature dependent heat capacity (J/cm^3/K)

ρ is the mass density (g/cm^3)

C_{300} is the specific value for heat at 300K (J/K Kg)

C_1 is the material dependent specific value for heat (J/K Kg)

β is the material dependent fitting parameter

The values of ρ, C_{300}, C_1, and β for both GaAs and AlAs are listed in table 7.5 [86]. They were defined using the C-interpreter functions. The temperature dependent heat capacity for each region was modelled by specifying the parameter *hc.comp* on the *material* statement.

Parameter	**Material**		**Units**
	GaAs	AlAs	
ρ	5.32	3.76	g/cm^3
C_{300}	322	441	J/K Kg
C_1	50	50	J/K Kg
β	1.6	1.2	-

Table 7.5 Heat Capacity parameters

In case of ternary compound ($Al_xGa_{1-x}As$), $C(T_L)$ is calculated by linear interpolation.

7.5.3 Thermal Conductivity

The value of thermal conductivity, κ, for each region is defined by specifying the parameter *tcon.power* on the *material* statement. It uses the following equation;

$$\kappa(T) = \frac{(T_C.CONST)}{\left(\frac{T}{300}\right)^{T_C.NPOW}} \text{ (W/cm.K)} \quad \ldots\ldots\ldots\ldots\ldots\ldots\ldots\ldots\ldots\ldots\ldots\ldots\ldots \quad (7.23)$$

where,

κ is the thermal conductivity

T is the lattice temperature

$T_C.CONST$ is the thermal conductivity at 300K

$T_C.NPOW$ is the fitting parameter

The value of thermal conductivity at 300K ($T_C.CONST$) and fitting parameter ($T_C.NPOW$) are defined using the C-interpreter functions as listed in table 7.6 [34, 85, 86].

Parameter	**Material**		**Units**
	GaAs	AlAs	
$T_C.CONST$	0.46	0.8	W/cm.K
$T_C.NPOW$	1.25	1.37	-

Table 7.6 Thermal Conductivity parameters

In case of ternary compound ($Al_xGa_{1-x}As$), $T_C.CONST$ and $T_C.NPOW$ are calculated as;

$$T_C.CONST^{AlGaAs} = \frac{1}{\left(\frac{1-x.com}{T_C.CONST^{AlAs}} + \frac{x.com}{T_C.CONST^{GaAs}} + \frac{(1-x)\times x}{C^{bowing}}\right)} \text{ (W/cm) ...... (7.24)}$$

$$T_C NPOW^{AlGaAs} = (1-x.com)\times T_C NPOW^{GaAs} + x.com \times T_C NPOW^{AlAs} \text{ (.K) .... (7.25)}$$

where,

$x.com$ is the composition fraction

C^{bowing} is the bowing factor (W/cm.K)

The bowing factor (C^{bowing}) compensates sudden change of thermal conductivity due to changing composition fraction ($x.com$). The $T_C.NPOW$ parameter is calculated by linear interpolation using Vegards law since experimental data other than 300K is currently not available [86].

7.5.4 Heat Generation

In GIGA^{TM}, the heat generation term *H* from equation 7.21 is set to zero for insulators. For conductors it is given as;

$$H = \frac{(divV)^2}{\rho} \text{ (J/cm}^3\text{/K) .... (7.26)}$$

where,

V is the voltage in mV/K

ρ is the mass density in g/cm^3

In Gunn diode model *hcte.el* is specified on the *models* statement. It uses hydrodynamic model for electrons only since holes do not play any role in the carrier transport effects. The heat generation 'H' is given as;

$$H = W_n + E_g U + \vec{J}_p.\vec{E} \text{ (J/cm}^3\text{/K) .... (7.27)}$$

where,

E_gU is the recombination heat power

W_n is the Joule heating term

$\vec{J}_p.\vec{E}$ is the Peltier Thomson Heat power

The recombination heat power (E_gU) is the product of band gap energy and the net generation-recombination rate U . The net generation-recombination rate is defined as;

$$U = R_{SRH} + R_n^A + R_p^A - G_n - G_p \quad (/\text{cm}^3.\text{s}) \;\ldots\ldots\ldots\ldots\ldots\ldots\ldots\ldots\ldots\ldots.. \;(7.28)$$

where,

R_{SRH} is the SRH recombination rate (equation 7.6 and 7.7)

R_n^A, R_p^A are the Auger recombination rates

G_n, G_p are the impact ionization rates

The carriers are heated due to lattice temperature increase and they exchange energy with the lattice using recombination and regeneration processes (equation 7.28). Both these effects are taken into account by the Joule heating term W_n which is defined as the energy density loss rate.

The energy density loss rate for electrons is given as;

$$W_n = \frac{3}{2} n \frac{k\left(T_n - T_L\right)}{taurn.el} + \frac{3}{2} kT_n R_{SRH} + E_g\left(G_n - R_n^A\right) \quad (/\text{cm}^3.\text{s}) \;\ldots\ldots\ldots.. \;(7.29)$$

where,

$taurn.el$ is the electron energy relaxation time.

7.5.5 Electron Energy Relaxation Time

In ATLAS$^{\text{TM}}$ no temperature dependent electron energy relaxation model is available. The electron energy dependent model was used instead. It is activated by using *e.taur.var* on the *models* statement. The model parameters listed in table 7.7 [85] are defined on the *material* statement. The electron energy W_n^{energy} is given as;

$$W_n^{energy} = \frac{3}{2} kT_n \text{ (eV)} \quad \text{………………………………………………..….. (7.30)}$$

The electron energy relaxation time is determined by quadratically varying values with respect to electron energy W_n^{energy}, by using following relations;

$$\tau_e = taurn.el = \begin{cases} TRE.T1, W_n^{energy} < TRE.W1 \\ TRE.T2, W_n^{energy} = TRE.W2 \\ TRE.T3, W_n^{energy} > TRE.W3 \end{cases} \text{ (eV)} \quad \text{……………….. (7.31)}$$

Parameter	Value	Units
$TRE.T1$	0.5	ps
$TRE.T2$	1.24	ps
$TRE.T3$	1.74	ps
$TRE.W1$	0.06	eV
$TRE.W2$	0.3	eV
$TRE.W3$	4.5	eV

Table 7.7 Electron energy relaxation time parameters

7.5.6 Thermal Boundary Conditions

In ATLAS^{TM}, the thermal boundary condition provides total energy flux after the lattice heat flow equation is solved. It is given by;

$$J_{boundary}^{thermal} = \frac{1}{R_{thermal}} (T_L - Temp) \quad \text{………..…………………………..….... (7.31)}$$

where,

T_L is the lattice temperature

$Temp$ is the temperature defined on the thermcontact statement

$R_{thermal}$ is the thermal resistance given as;

$$R_{thermal} = \frac{1}{Alpha} \quad \ldots\ldots\ldots\ldots\ldots\ldots\ldots\ldots\ldots\ldots \text{(7.31)}$$

The parameter $Alpha$ is defined on the *thermcontact* statement. The *thermcontact* statement also defines the position of the thermal contact (heat sink) and temperature $Temp$. In the Gunn diode model two thermal boundary conditions were defined for Cathode and anode heat sinks respectively. The parameter $Alpha = 2.5$ was defined.

7.6 C-Interpreter Functions

Some of the physical models used in ATLAS^{TM} can be modified using the built-in C-language interpreter. C-interpreter functions are particularly useful to precisely define material parameters not available in ATLAS^{TM} reference tables. The C-interpreter functions containing analytic model descriptions which were written are listed in table 7.8.

Function	Model	Description
f.bandcomp	Band Gap	Composition based band gap. f.bandcomp parameter is defined in the material statement.
f.vsatn	Saturation Velocity	Composition and temperature dependent saturation velocity. f.vsatn parameter is defined in the material statement.
f.munsat	Mobility	Determines the temp dependent mobility. Set by fldmob evsatmod=0. f.enmun parameter is defined in the material statement.
f.enmun	Mobility	Determines temperature dependent low field mobility. f.enmun parameter is defined in the mobility statement.
f.tcap	GIGA	Thermal capacity in Giga. f.tcap parameter is defined in the material statement.
f.tcond	GIGA	Thermal conductivity in Giga. f.tcond parameter is defined in the material statement.

Table 7.8 C-Interpreter Functions used in model development

7.7 Conclusion

The accuracy of the simulated response depends on the choice of material parameters and the selection of physical models (and their associated parameters) used. The material and model parameters used were therefore extensively researched from a variety of sources. They have been presented and discussed, which were carefully selected for each layer depending on the material and carrier concentration in the region. It included Mobility models, Carrier Generation-recombination models, Carrier Statistics and Transport models and GIGA^{TM} Self Heating Simulator. It was shown that the analytic function based on the work of Caughey and Thomas is used for modelling field dependant mobility in the contact layers, spacer layers, AlGaAs launcher and also the transit region for field strengths below the negative differential mobility (NDM) threshold. For field strengths in the transit region above the NDM threshold, the Barnes NDM model is used. The Shockley-Read-Hall (SRH) recombination model is applied in the nominally undoped $Al_xGa_{(1-x)}As$ barrier. The SRH concentration-dependent lifetime model is used in the rest of the device to account for the varied silicon impurity concentrations.

The ATLAS^{TM} non-isothermal device modeller module, Giga, used for local temperature, self-heating, lattice heat flow and heatsinking effects have been discussed. It is based on the models suggested by Wachutka and accounts for Joule heating along with heating and cooling due to carrier generation and recombination. Finally, it was shown that where the platform did not allow sufficient flexibility to accurately account for the interdependency of parameters, appropriate C-language functions were written and incorporated through the in-built C-interpreter.

Chapter 8 Gunn diode Results: DC Analysis

8.1 Introduction

The simulated DC characteristics of the model are presented in this chapter. They were used to study hot electron injection doping spike. The doping spike carrier concentration optimum value was determined using a modelled-measured approach.

In order to examine the accuracy of the developed model a comparison to measured data needs to be made. A large amount of data from production and engineering testing carried out at e2v Technologies Plc was made available for this purpose. The available data included the characteristics of 77 GHz (1.65 µm transit region device) devices with a range of epitaxial structures which were measured over a range of temperatures. Also available was data from a new 125 GHz second harmonic device and 94 GHz fundamental device. A relatively constant I-V current is

The Gunn diodes epitaxially grown at The University of Manchester were processed / packaged at e2v technologies Plc. They were die-packaged and etched to current (nominally 750-1200mA) to reduce heat generation and get better heat sinking. Resultantly, relatively constant current levels were achieved in the I-V relationships despite reducing device transit region length and increasing its doping.

8.2 Advanced Step Graded Gunn Diode Modelled–Measured Results

The advanced 77 GHz second harmonic GaAs Gunn diodes discussed here incorporate a step-graded AlGaAs hot-electron launcher, and are commercially manufactured in volume by e2v Technologies (UK) Plc. for use in 77GHz automotive Autonomous Cruise Control (ACC) systems. Tight specifications are placed on parameters such as RF output power, applied voltage controlled frequency tuning range and the oscillation frequency’s temperature dependence.

These parameters are all highly dependant on hot-electron injector composition, especially carrier concentration in the injector's doping spike [2, 3].

The hot electron injector effectiveness was evaluated using the 77 GHz model. The doping spike carrier concentration, DC I-V characteristics and doping spike effects on I-V curves are discussed below.

8.2.1 Doping Spike Carrier Concentration

The hot electron injector, situated between the n^+ cathode contact layer and the n^- transit region, consists of two main components: a graded AlGaAs launcher and a doping spike which is required to modify the forward-bias downstream electric field in the transit region. As shown in fig. 8.1, in its absence a depletion region is formed behind the launcher which prevents the nucleation of high-field domains. With the increase of applied potential, the negative-field gradient rises and as a result the depletion region grows forming a dead zone. The dead zone at the start of transit region reduces the performance of the launcher. The dead zone eventually diminishes as the applied voltage is increased.

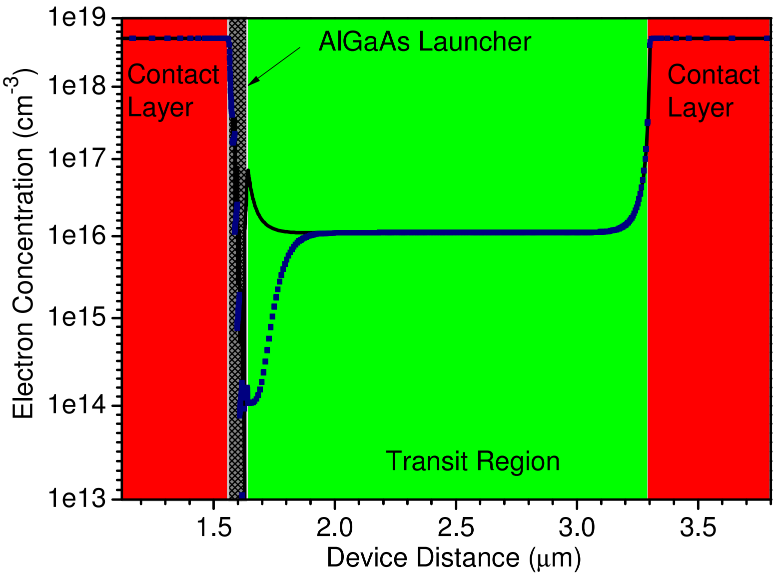

Fig. 8.1 The effects of the doping spike (cc 1×10^{18} cm^{-3}) on electron concentration in the transit region (——; spike present, -----; spike absent)

The device model with n^+ doping spike (cc $1\times10^{18}\,cm^{-3}$) resulted in the positive electric field gradient, which keeps the electron concentration throughout the transit region as shown in Fig. 8.1. Concomitantly it eliminated the depletion region, thereby ensuring the elimination of the dead zone and leading to high efficiency of the hot electron injector. This compares well to previous simulations results obtained and published by another group using SILVACO^{TM} [10]. This greatly increased confidence in the developed model.

8.2.2 DC I-V Characteristics of 77 GHz second Harmonic GaAs Gunn

A comparison of the simulated I-V characteristics and measured data at temperature 300K is shown in Fig. 8.2. The measured results are from a manufactured device, and supplied by 'e2v Technologies Plc'. It can clearly be seen that the simulated I-V characteristics in both forward and reverse bias match well to those of an actual device thus validating the use of physical models selected for the simulations. It is noted that in forward bias the simulated response beyond three volts shows greater negative differential resistance than the measured data. The higher negative differential is probably due to the ideal heat sinks higher efficiency and lower resistance values used in the simulation.

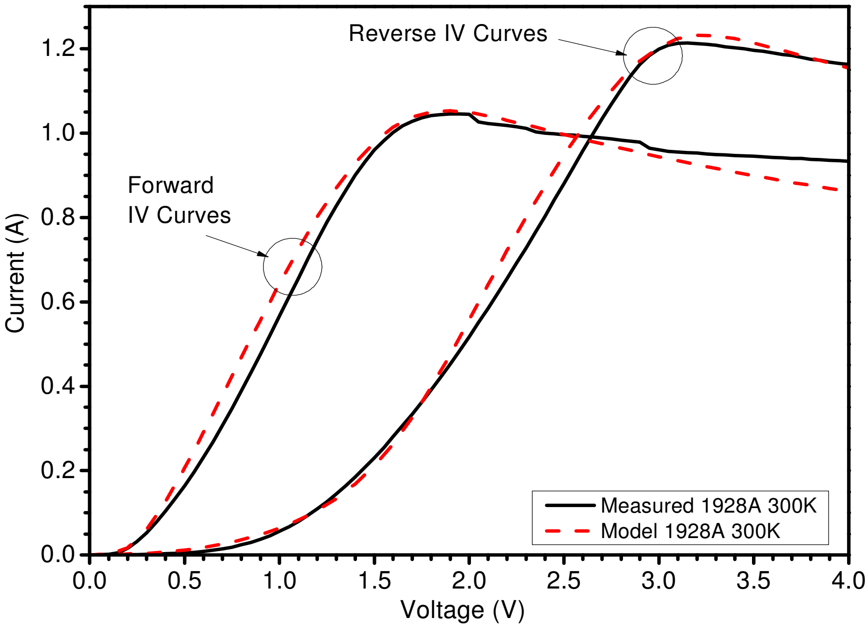

Fig. 8.2 **Modelled and measured forward - reverse I-V curves.**

8.3 Doping Spike Effects

To compliment experimental data and investigate the relationship between doping spike carrier concentration and I_{asym}, the model was simulated with varying carrier concentration ($2\times10^{18}cm^{-3}$, $1\times10^{18}cm^{-3}$, $7.5\times10^{17}cm^{-3}$, and $5\times10^{17}cm^{-3}$) shown in Fig. 8.3. It can be seen that as the doping spike carrier concentration decreases the injector performance degrades and as a result the asymmetry increases. Since the injector does not play any role being at the end of the transit region during reverse bias condition, similar reverse I-V curve could be seen in the Fig. 8.4.

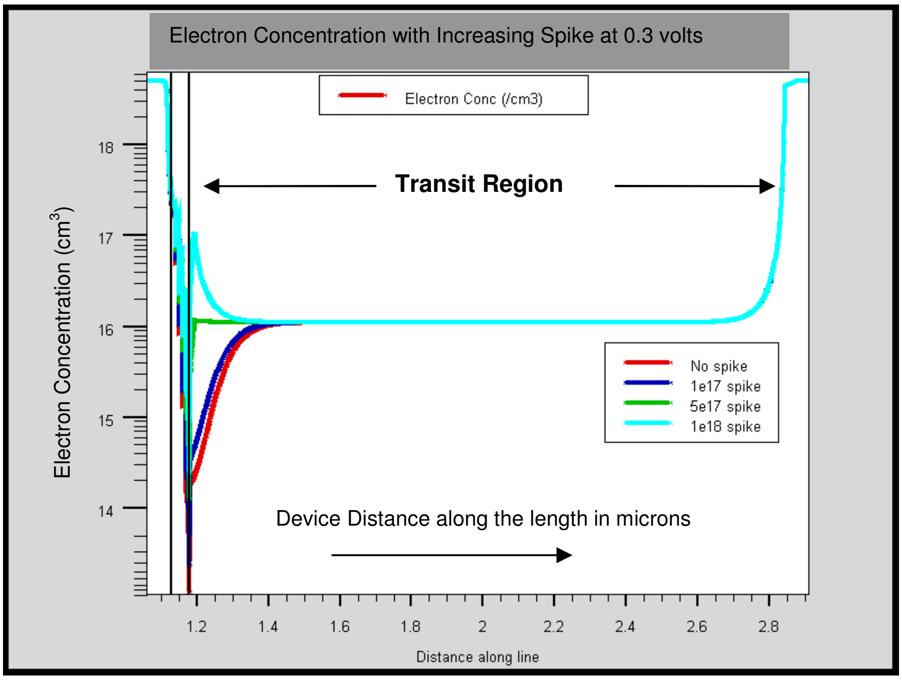

Fig. 8.3 **Electron concentration with changing doping spike carrier concentration (cc)**

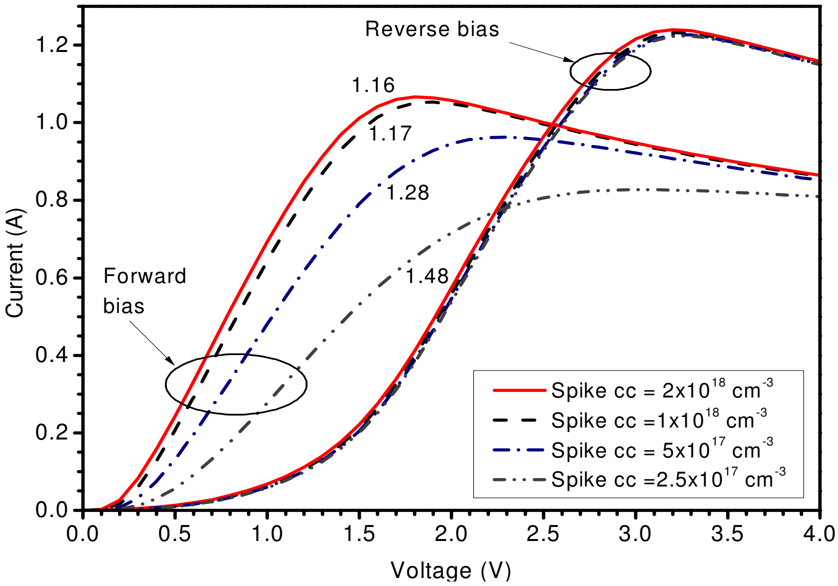

Fig. 8.4 **Effects of variation in doping spike carrier concentration on simulated I-V characteristics (numbers next to forward bias curves represent calculated asymmetry values)**

Fig. 8.5 shows the I_{asym} plotted verses doping spike carrier concentration. It can be seen that although I_{asym} decreases as the carrier concentration increases, which agrees with the trend noted for the experimental data, there is a small discrepancy between the absolute measured and simulated values. However qualitatively, it shows the same trend and is remarkably reproduced. This discrepancy was the result of inaccurate representation of the electric field and current flow through the device inherent to the method used for scaling the 2D model to obtain the correct device area. This has a much greater effect when modelling the Gunn diode which is a 'field driven' device, than with voltage or current driven devices for which SILVACO^{TM} was originally intended. These results were published [99]. Cylindrical device geometry was defined to take into account cylindrical geometry of the manufactured device.

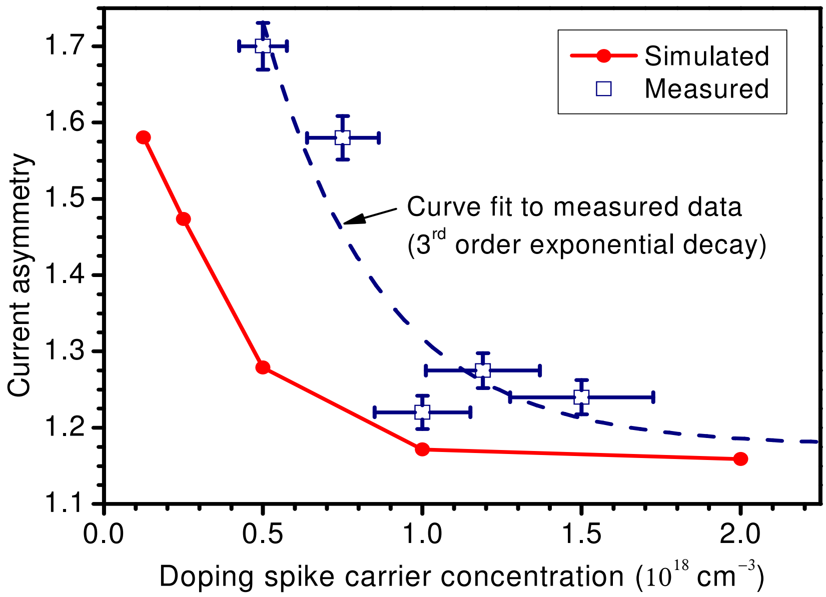

Fig. 8.5 **Simulated and measured asymmetry values versus doping spike carrier concentration**

A full 3D cylindrical model was developed and results compared to that of a 2D model. This computationally expensive (tens times than a 2D model) full 3D cylindrical model [100] was developed using SILVACO^{TM} ATLAS^{TM} version 5.12.1 in order to ensure that the modelled electric field across the device realistically represented that in an actual device [100]. However, due to the improved meshing capabilities of the since released version 5.12.32 of SILVACO^{TM} ATLAS^{TM}, a cylindrical device geometry can now be defined and applied to a 2D model. After verification that a 2D model using the new meshing technique produced similar results to the full 3D model, the method was adopted and a large reduction in computational time obtained for subsequent simulations.

8.4 Measured 77 GHz Devices Data Comparison with Modelled Devices

In order to further investigate the accuracy of the model, its simulated response was compared to the measured results from devices with slightly different epitaxial structures (the main differences are the doping spike carrier concentrations) shown in table 8.1. Ambient temperature variation is also included in both simulated and measured data.

Wafer Name	**Doping Spike Carrier Concentration (cm^{-3})**	**Transit Region Length (µm)**	**Transit Region Carrier Concentration (cm^{-3})**
VMBE 1928A	1×10^{18}	1.65	1.1×10^{16}
VMBE 1900	5×10^{17}	1.65	1.1×10^{16}
VMBE 1909	7.5×10^{17}	1.65	1.1×10^{16}

Table 8.1 Measured devices with slightly different epitaxial structures – doping spike carrier concentration variation

The results for each epitaxial structure will now be discussed.

8.4.1 Doping Spike Carrier Concentration 1×10^{16} cm^{-3} Modelled Device Results (VMBE 1928A)

The forward and reverse I-V curves of a measured device (VMBE 1928A) and modelled device 1928A are shown in Fig. 8.6. Doping spike with carrier concentration 1×10^{18} cm^{-3} was used in both the modelled and measured devices. Both modelled and measured data compared very well. The difference in modelled forward I-V curve, showing higher negative differential resistivity, at around 3V and onwards is thought due to the heat sinks higher efficiency.

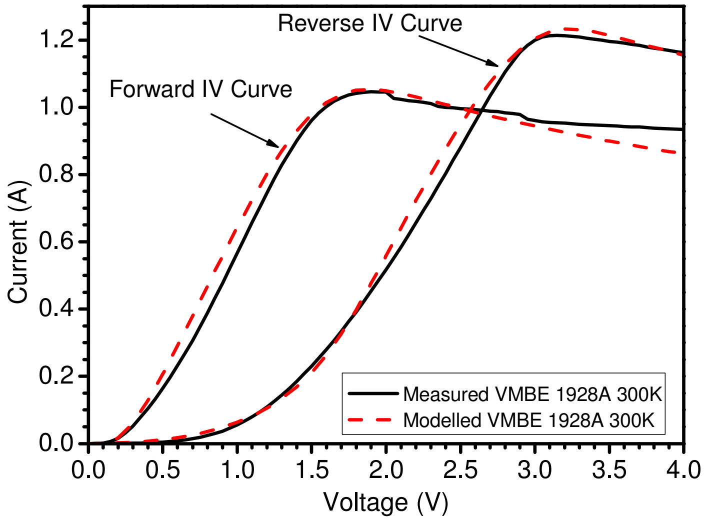

Fig. 8.6 **VMBE 1928A Modelled and measured forward - reverse I-V curves**

Modelled and measured temperature curves for VMBE 1928A devices are shown in Fig. 8.7. The I-V curves were plotted for an ambient temperature of 300K and 323K respectively. Upon increasing the temperature to 323K the injector effectiveness is reduced and as a result the modelled device's current saturated at a lower value which is in agreement with published theoretical data. The effects of ambient temperature variation on the simulated and measured results resulted in a close match. This further validates the developed model and use of the GIGA simulator.

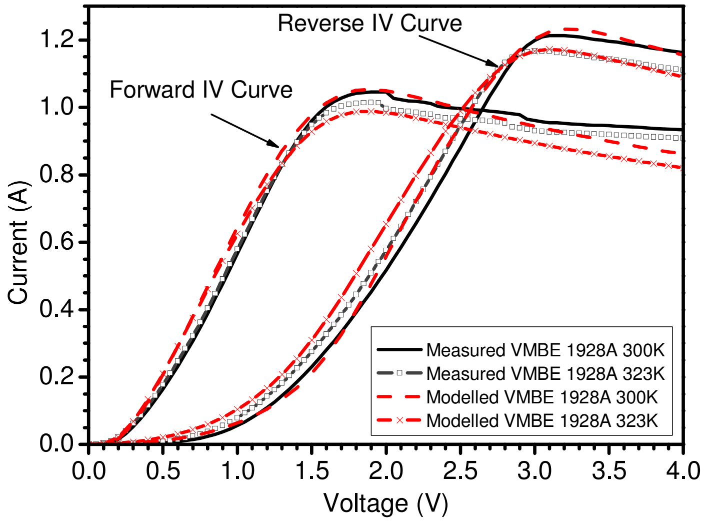

Fig. 8.7 **VMBE 1928A Temperature forward - reverse I-V curves**

8.4.2 Doping Spike Carrier Concentration 5×10^{17} cm^{-3} Modelled Device Results (VMBE 1900)

The spike doping carrier concentration was reduced from 1×10^{18} cm^{-3} to 5×10^{17} cm^{-3}. Both simulated and measured devices yielded the asymmetrical response shown in Fig. 8.8. A good match can be seen between the modelled and measured data especially in reverse bias conditions. Again the forward I-V curve showing more negative differential resistance is attributed to the higher efficiency of the ideal heat sinks used in the modelled device.

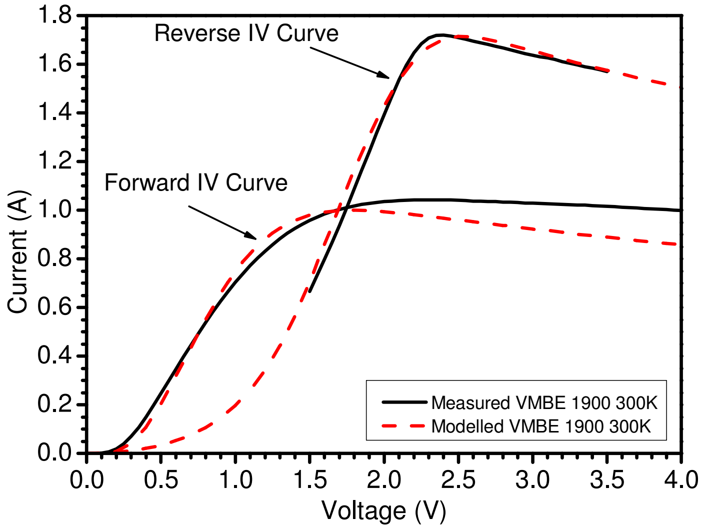

Fig. 8.8 **VMBE 1900 Modelled and measured forward - reverse I-V curves**

Fig. 8.9 shows the temperature simulation for VMBE 1900 with reduced spike carrier concentration. Again the modelled reverse I-V curve matched closely to the measured data.

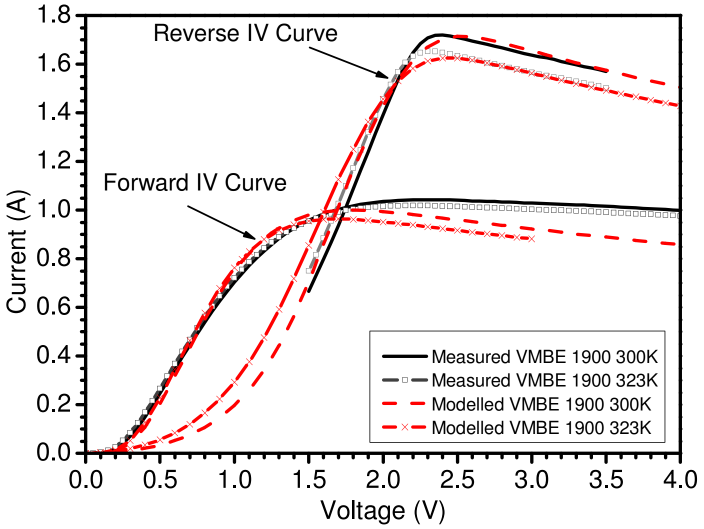

Fig. 8.9 **VMBE 1900 Temperature forward - reverse I-V curves**

8.4.3 Doping Spike Carrier Concentration 7.5×10^{17} cm^{-3} Modelled Device Results (VMBE 1909)

The spike doping carrier concentration was increased from 5×10^{17} cm^{-3} to 7.5×10^{17} cm^{-3}. Both simulated and measured devices yet again yielded the asymmetrical response shown in Fig. 8.10. A good match can be seen between the modelled and measured data especially in forward bias conditions.

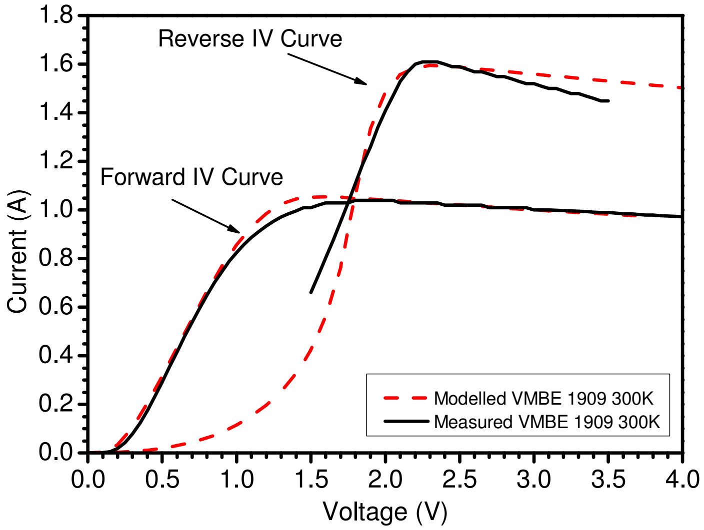

Fig. 8.10 **VMBE 1909 Modelled and measured forward - reverse I-V curves**

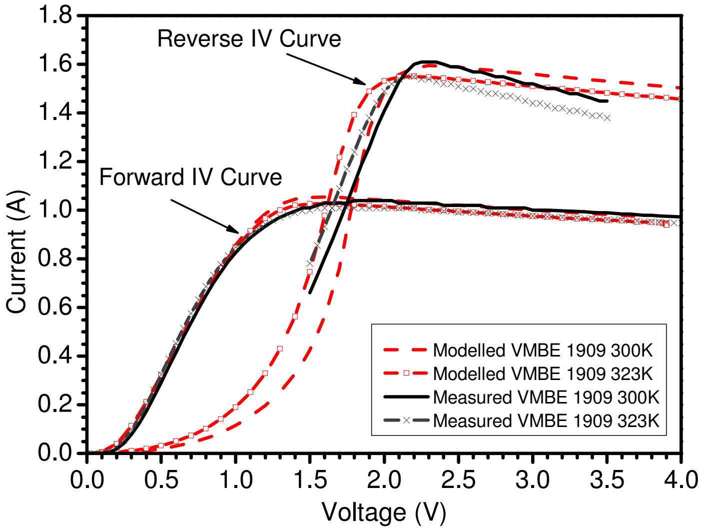

Fig. 8.11 **VMBE 1909 Temperature forward - reverse I-V curves**

Modelled and measured temperature curves for VMBE 1909 devices are shown in Fig. 8.11. The effects of ambient temperature variation on the simulated and measured results resulted in a close match, especially in forward bias conditions.

Although it differs slightly in the reverse I-V curves but the onset of Negative Differential Resistance (NDR) and bias region where device provides NDR remains similar. This further validates the developed model and use of the GIGA^{TM} simulator.

Fig. 8.12 shows the I_{asym} plotted verses doping spike carrier concentration for three discussed devices including 1928A, 1900 and 1909. Both measured and modelled devices provided decreasing current asymmetry values with the increase in doping spike carrier concentration. The decrease in carrier concentration is in accordance with the theory and indicates the increase in injector efficiency. A close match between measured and modelled results is due to simulating cylindrical geometry for the modelled devices. The cylindrical geometry correctly simulated the electric field effects in the modelled devices.

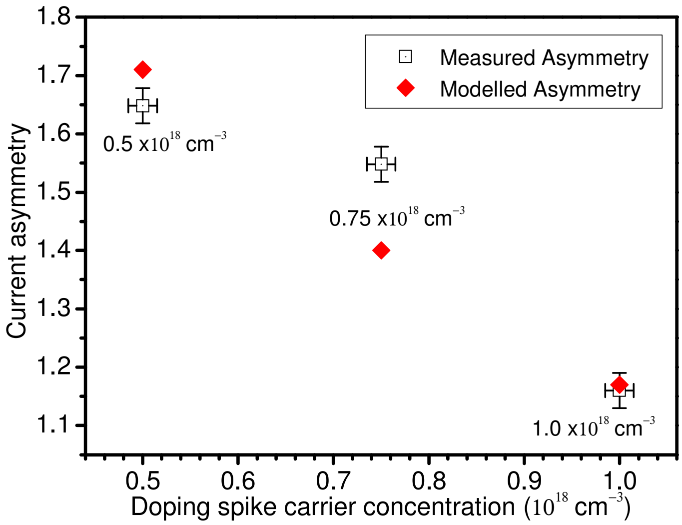

Fig. 8.12 Simulated and measured asymmetry values versus doping spike carrier concentration.

The hot electron injector highest efficiency was achieved with doping spike carrier concentration 1×10^{18} cm^{-3}. Its efficiency reduced by decreasing doping spike carrier concentration. However, increasing carrier concentration had minimal effect. Therefore, doping spike carrier concentration 1×10^{18} cm^{-3} was used in both modelled and fabricated devices.

8.5 Higher Frequency Measured–Modelled DC I-V Characteristics

The entries listed in table 8.2 mostly correspond to material previously grown for experimental studies in the development of D-band GaAs Gunn devices: as such sample devices had already been fabricated and tested, with measured data available. This is with the exception of XMBE189 (0.4 µm transit region length) which was produced to test whether GaAs based Gunn oscillators operating at sub-millimetre waves can be realized. It can be seen in table 8.2, that as the transit region length was decreased, the length – carrier concentration product, $L.N_D$, was kept approximately constant.

Wafer Name	Doping Spike Carrier Concentration (cm^{-3})	Transit Region Length (µm)	Transit Region Carrier Concentration (cm^{-3})
VMBE1901	1×10^{18}	1.65µm	1.1×10^{16}
VMBE1950	1×10^{18}	1.1µm	2×10^{16}
VMBE1897	1×10^{18}	0.9µm	2.5×10^{16}
VMBE1898	1×10^{18}	0.7µm	3.5×10^{16}
XMBE189	1×10^{18}	0.4µm	5.4×10^{16}

Table 8.2 Measured devices with slightly different epitaxial structures – transit region length and its carrier concentration variation

The simulated DC characteristics for each device (table 8.2) are presented and compared with measured results [101]. Ambient temperature variation is also included in both simulated and measured data. These devices were die-packaged and etched to current (nominally 750-1200mA) to reduce heat generation and achieve better heat sinking

8.5.1 1.65 µm Transit Region Device DC Results (VMBE 1901 – 77 GHz Device)

The forward and reverse I-V curves of a measured device (VMBE 1901) and modelled device 1901 are shown in Fig. 8.13. A doping spike with carrier concentration 1×10^{18} cm^{-3} was present in both the modelled and measured devices. The complete reverse bias curve for a measured device could not be obtained from e2v Technologies Plc. However, the available measured data compared reasonably with the device model.

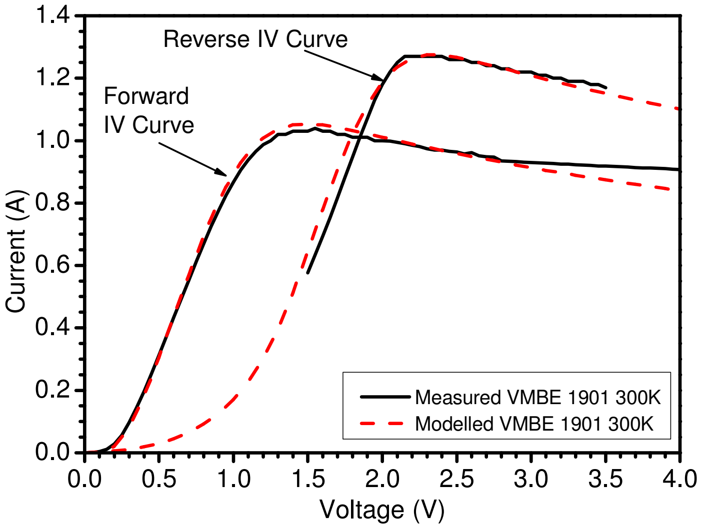

Fig. 8.13 VMBE 1901 Forward and reverse I-V curves for a 70-80 GHz 2nd harmonic device at 300K

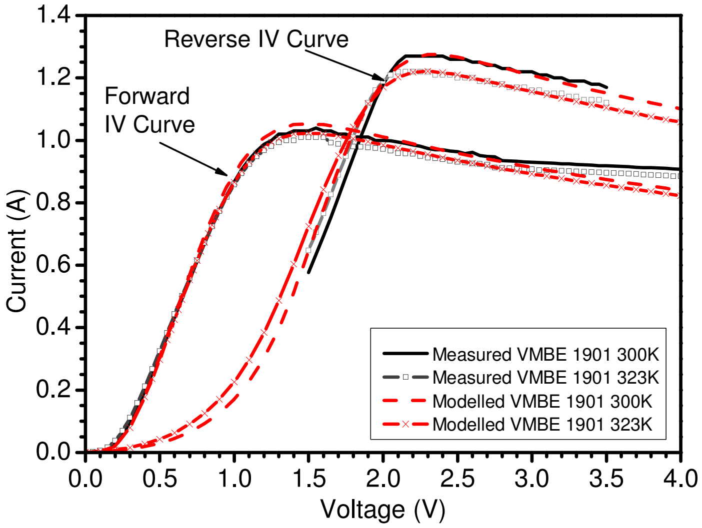

Fig. 8.14 VMBE 1901 Temperature forward and reverse I-V curves

Modelled and measured temperature curves for VMBE 1901 devices are shown in Fig. 8.14. The I-V curves were plotted for an ambient temperature of 300K and 323K respectively. Upon increasing the temperature to 323K the injector effectiveness reduced and as a result the modelled device's current saturated at a lower value which is in agreement with published theoretical data. The effects of ambient temperature variation on the simulated and measured results resulted in a close match. This further validates the developed model and use of the GIGA^{TM} simulator.

8.5.2 1.1 µm Transit Region Device DC Results (VMBE 1950 - 125GHz Device)

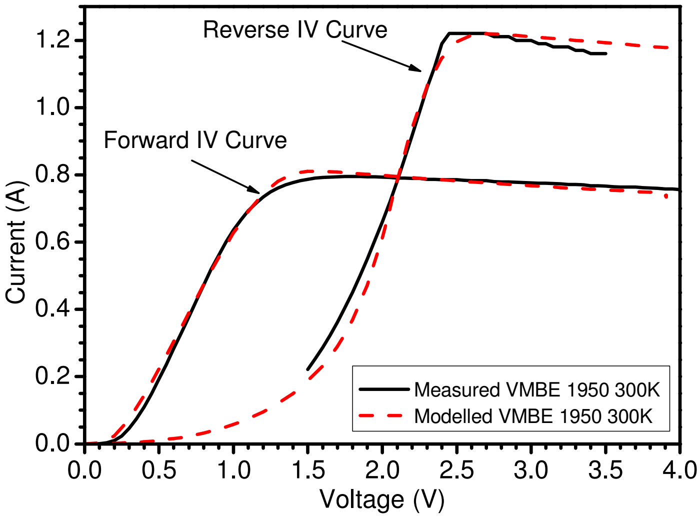

Fig. 8.15 **VMBE 1950 Forward and reverse I-V curves for a 62.5GHz fundamental, 125GHz 2nd harmonic device at 300K**

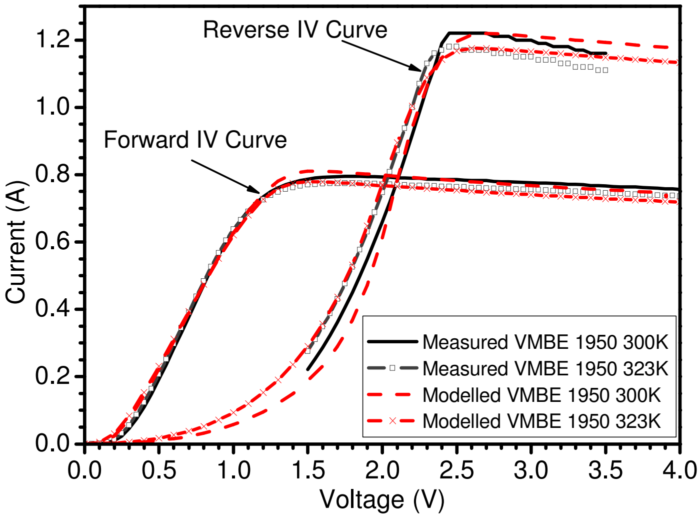

Fig. 8.16 **VMBE 1950 Temperature forward and reverse I-V curves**

125 GHz device comprised of a modified device structure. To model and compare the new structure (VMBE 1950), the modelled 77 GHz structure's transit region was modified by reducing its length from 1.65 µm to 1.1 µm and its doping was increased from 1.1×10^{16} cm^{-3} to 2×10^{16} cm^{-3}. The measured and modelled data is shown in Fig. 8.15. A good match can be seen between the modelled and measured data especially in forward bias low voltage conditions. The forward and reverse I-V curves showing more negative differential resistance is attributed to the higher efficiency of heat sinks used in the modelled device.

125 GHz device model was simulated at increasing temperature. The results indicated similar characteristics as were achieved for 77 GHz devices. The temperature effects on the barrier effectiveness and current saturation correlated to the published theory.

After successful development of a model for 125 GHz second harmonic device the modelling work was extended to develop models for higher frequency devices. Further models developed included VMBE 1897, VMBE 1898 and XMBE 189.

8.5.3 0.9 µm Transit Region Device DC Results (VMBE 1897- 125 GHz Device)

VMBE 1897 device comprised of a sub-micron transit region length device structure. To model and compare the new structure (VMBE 1897), the modelled 77 GHz structure's transit region was modified by reducing its length from 1.65 µm to 0.9 µm and its doping was increased from 1.1e16 cm^{-3} to 2.5e16 cm^{-3}. The modelled and measured DC I-V curves again yielded a close match (Fig. 8.17).

The measured modelled results at increasing temperature provided a close match (Fig. 8.18). The results indicated similar characteristics as were achieved for larger transit region devices. The temperature effects on the barrier effectiveness and current saturation correlated to the published theory.

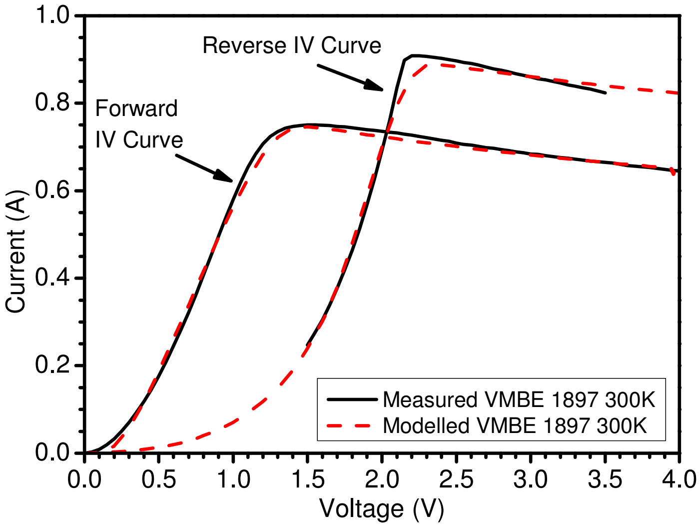

Fig. 8.17 **VMBE 1897 Forward and reverse I-V curves for a 62.5 GHz fundamental, 125GHz 2nd harmonic device at 300K**

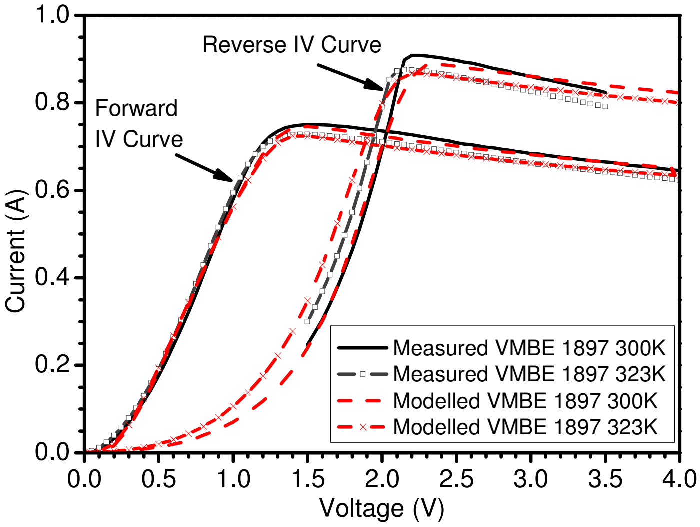

Fig. 8.18 **VMBE 1897 Temperature forward and reverse I-V curves**

8.5.4 0.7 µm transit region device DC results (VMBE 1898 - 100GHz device)

The simulated and measured forward and reverse bias I-V characteristics of a device with a 100 GHz fundamental frequency are shown in Fig. 8.19 where again, an extremely strong match can be seen especially in the forward I-V curves.

The measured modelled results at increasing temperature provided a close match (Fig. 8.20). The results indicated similar characteristics as were achieved for lower frequency devices. The temperature effects on the barrier effectiveness and current saturation correlated to the published theory.

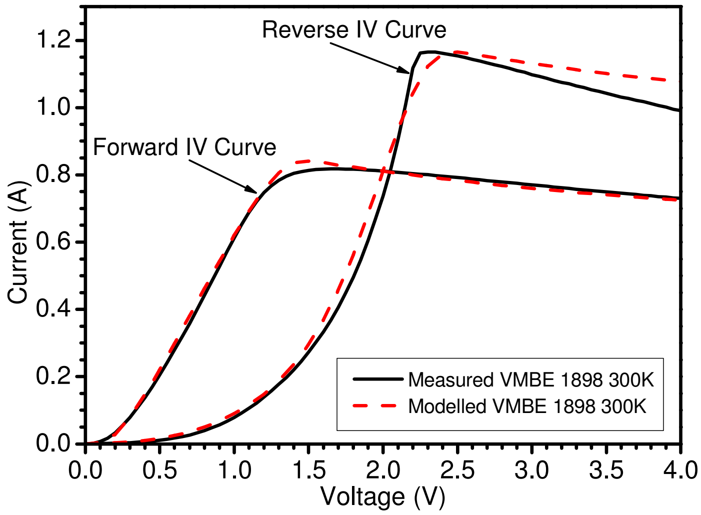

Fig. 8.19 **VMBE 1898 Forward and reverse I-V curves for a 100 GHz fundamental device at 300K**

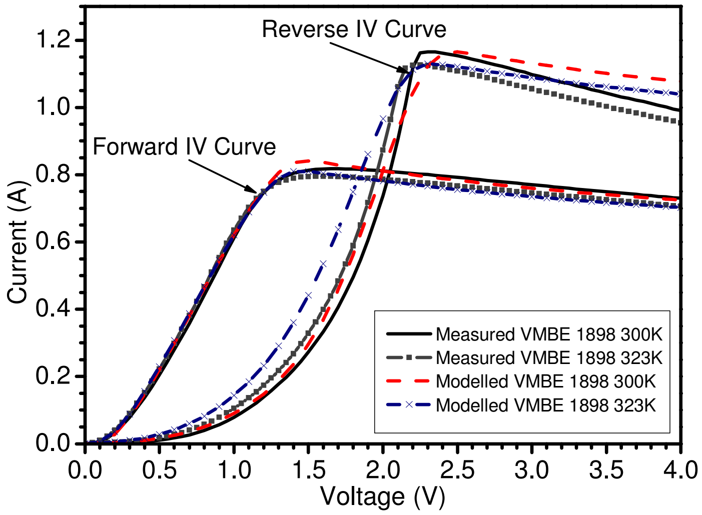

Fig. 8.20 **VMBE 1898 Temperature forward and reverse I-V curves**

8.5.5 0.4 µm Transit Region Device DC Results (XMBE 189 – 200 GHz Device)

Having gained sufficient experience and confidence in the models developed up to 100 GHz fundamental frequency, the model was then extended to higher frequency devices (~ 200GHz), thereby addressing experimentally unreached limits of operation for GaAs-based Gunn devices. Extensive modelling points out to a transit region of 0.4 µm as providing the most promising asymmetric I-V curves for a 200 GHz fundamental device as shown in Fig. 8.21. After successive iterations simulation suggested that the optimal transit region carrier concentration level was 5.4 x10^{16} cm^{-3} and spike carrier concentration level was 1x10^{18} cm^{-3} (Fig. 8.21) The device epitaxial structure was grown as discussed before.

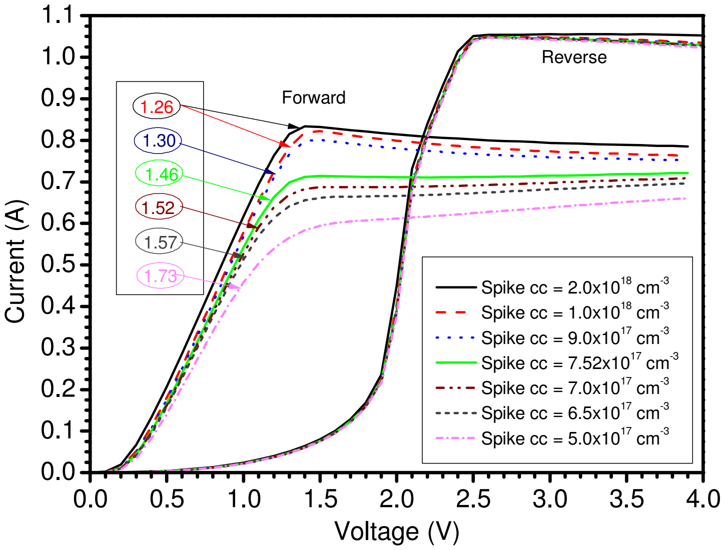

Fig. 8.21 XMBE 189 Modelled forward and reverse I-V curves. Effects of variation in doping spike carrier concentration (cc) on simulated I-V characteristics (numbers next to forward bias curves represent calculated asymmetry values). Transit region carrier concentration was 5.4 x10^{16} cm^{-3}.

The device I-V measurements have provided an asymmetric response (Fig. 8.22). Thus a 200 GHz fundamental device has been made for the first time from a GaAs/AlGaAs material system. It is achieved through predictive modelling and by sequentially extending device's operating frequency while studying its underlying principles. The time-domain responses are presented in the next chapter.

The measured modelled results at increasing temperature provided a close match (Fig. 8.23). The results indicated similar characteristics as were achieved for lower frequency devices.

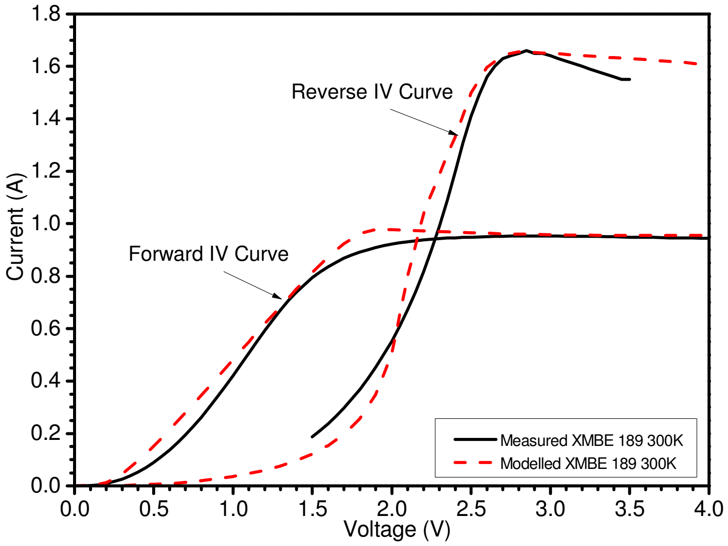

Fig. 8.22 **XMBE 189 Modelled forward and reverse I-V curves for a 200 GHz fundamental device at 300K**

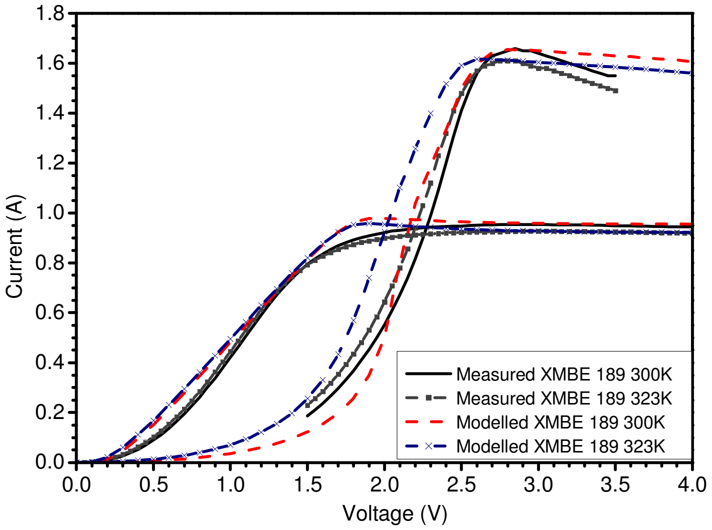

Fig. 8.23 **XMBE 189 Temperature forward and reverse I-V curves**

8.6 Conclusion

The simulated DC I-V characteristics have been presented of a 2D physical model developed using SILVACO^{TM} for a GaAs Gunn diode with a step graded AlGaAs hot electron injector. They were used to study relationship between I_{asym} and doping spike carrier concentration. The doping spike carrier concentration optimum value $1x10^{18}$ cm^{-3} was determined using modelled-measured approach.

Giga, a self heating simulator available in SILVACO^{TM}, was used to simulate the device's lattice heating effects. It was used with the definition of heat sinks at the cathode and anode respectively.

The developed model comparison with measured data was shown. The measured data over a range of temperatures included the DC characteristics of 77 GHz (1.65 µm transit region device) devices with a range of epitaxial structures, 125 GHz second harmonic device, ~100 GHz fundamental device and ~200 GHz fundamental device. A good match between measured and simulated I-V curves validates the choice of physical models and parameters used.

It was shown that the Gunn diodes were die-packaged and etched to current (nominally 750-1200mA) to reduce heat generation and achieve better heat sinking. Resultantly, relatively constant current levels were achieved in the I-V relationships despite reducing device transit region length and increasing its doping.

Chapter 9 Gunn diode Results: Time-domain analysis

9.1 Time-Domain (Transient) Solutions

Transient solutions were used to obtain a time dependent response such as determining the device oscillating frequency in biased condition. These solutions provided modelled device time-domain responses. The time-domain simulations helped to analyse modelled device RF characteristics. The RF characteristics such as output power and oscillation frequency are highly dependant on interactions between the device and the resonant circuit in which it is mounted.

Wafer Name	Target frequency (GHz, Harmonic)	Transit Region Length (µm)	Transit Region Carrier Concentration (cm^{-3})
VMBE1901	70-80GHz, 2nd harmonic	1.65 µm	1.1×10^{16}
VMBE1950	62.5GHz, Fundamental / 125GHz, 2nd harmonic	1.1 µm	2×10^{16}
VMBE1897	62.5GHz, Fundamental / 125GHz, 2nd harmonic	0.9 µm	2.5×10^{16}
VMBE1898	100GHz, Fundamental	0.7 µm	3.5×10^{16}
XMBE189	NA	0.4 µm	5.4×10^{16}

Table 9.1 Measured devices with slightly different epitaxial structures – transit region length and its carrier concentration variation

9.2 Time-Domain Analysis of various Epitaxial Structures

The results of the time-domain simulations for each device listed in table 9.1 are presented. These simulations were performed with the terminal impedance set to 50Ω with the sole intention of establishing the limits of transit region length capable of supporting a steady-state (non-decaying) oscillation. This free-running frequency is reduced when the device is embedded in a practical resonant circuit: a full discussion of this concept was explained in chapter 3. The simulated oscillation frequencies are therefore not expected to precisely match those measured (which are defined by oscillator design), but to be slightly higher. In addition, the RF power (calculated from the average bias voltage and the current oscillation) cannot be expected to match that of a specific oscillator. Nevertheless, these simulations allowed performing large-signal device characterizations and comparing to measured results [102].

9.2.1 1.65 µm Transit Region Device Results (VMBE1901)

It can be seen that in Fig. 9.1, the simulated time-domain response for the device with a 2.2V external bias, although sinusoidal in nature at a frequency of approximately 45 GHz, appears to be extremely noisy. At a higher external bias of 3.2V, the free-running oscillation in the time-domain response (Fig. 9.2) is now at the lower frequency of 40 GHz, does not exhibit the noise seen at a 2.2V external bias, and also exhibits a much higher peak-to-peak value (which increases from 12 mA to 50 mA). This is in complete agreement with the explanation given in chapter 6 section 6.4 regarding the behaviour of a free-running Gunn device as the bias voltage is increased.

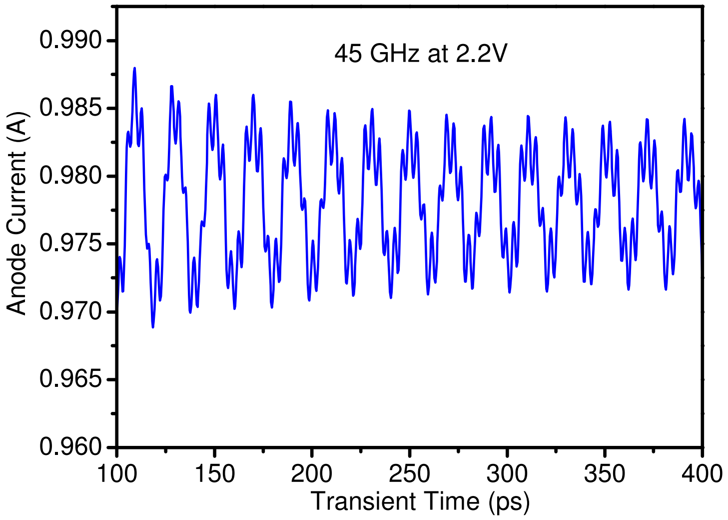

Fig. 9.1 The simulated fundamental frequency time-domain response of a device fabricated from VMBE1901 (1.65 µm transit length) under a 2.2V external bias

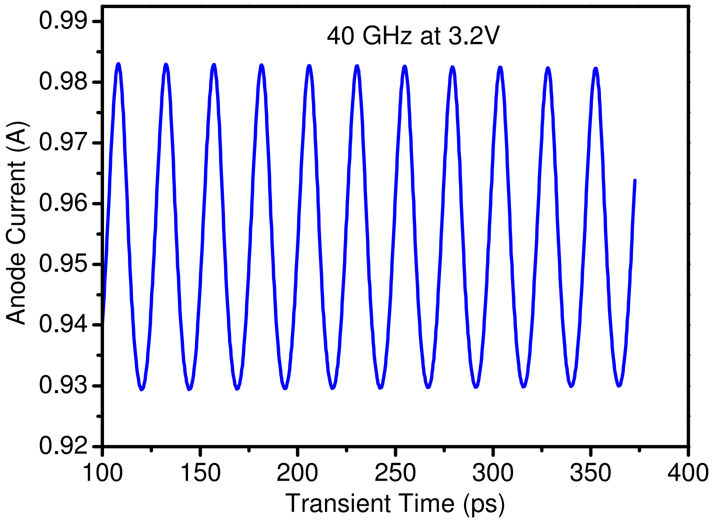

Fig. 9.2 The simulated fundamental frequency time-domain response of a device fabricated from VMBE1901 (1.65 µm transit length) under a 3.2 V external bias.

9.2.2 1.1 µm Transit Region Device Results (VMBE1950)

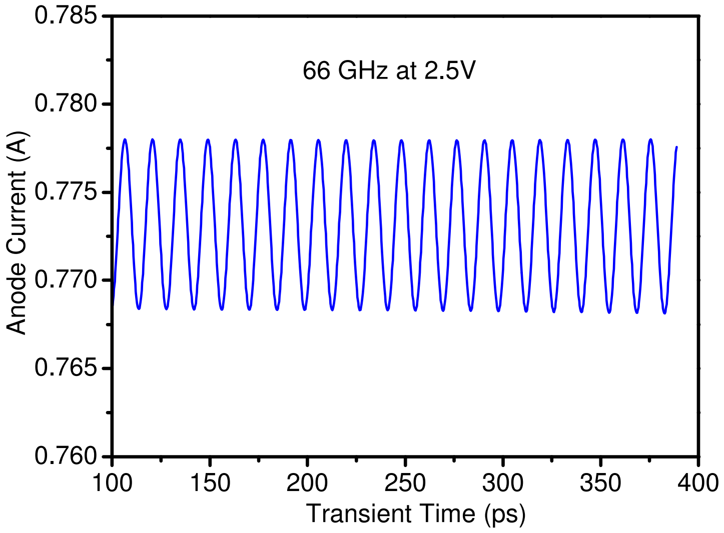

Fig. 9.3 The simulated fundamental frequency time-domain response of a device fabricated from VMBE1950 (1.1 µm transit length) at an external bias of 2.5V, temperature 300K.

The time-domain response obtained and given in Fig. 9.3, shows a fundamental free-running frequency of approximately 66 GHz. The fabricated device has been shown to provide around 130 mW at 62 GHz operating in fundamental mode, and 40 mW at 121.5 GHz in a second harmonic oscillator: the latter is the highest reported power for a GaAs device at this frequency [103]. The results of the time-domain simulations are therefore inline with those expected from measured results. It is noted here that although the time-domain simulations of the device were performed with an external bias of 2.5 V, unlike the result for the 1.65 µm device at the same bias voltage, the trace shows no noise. This is thought to be due to the shortened transit region leading to a higher applied field across the device and so the formation of stronger oscillations for the same applied external bias.

9.2.3 0.9 µm Transit Region Device Results (VMBE1897)

The time-domain simulations showed stable free running fundamental frequency oscillations at 79 GHz as shown in Fig. 9.4. A fabricated device with this epitaxial structure and geometry provided a maximum fundamental frequency power of 80-90 mW at 63 GHz, and around 10 mW at 123 GHz in a second harmonic oscillator. The results are therefore again inline with theory and with those obtained through measurement of a fabricated device.

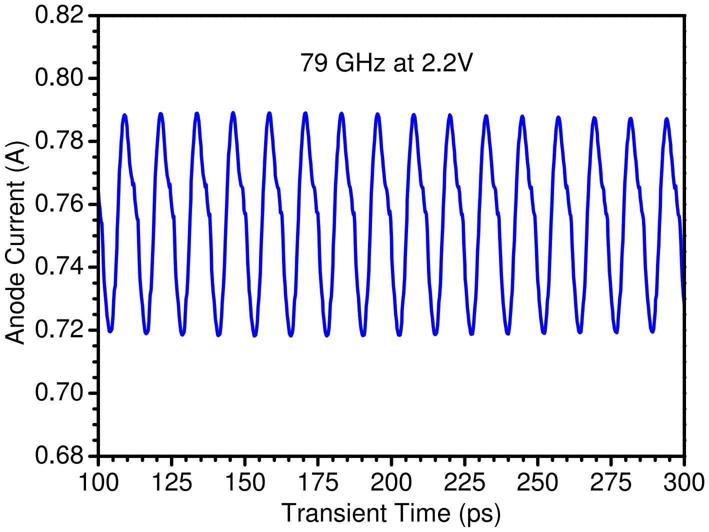

Fig. 9.4 The simulated fundamental frequency time-domain response of a device fabricated from VMBE1897 (0.9 µm transit length) at an external bias of 2.2V, temperature 300K.

9.2.4 0.7 µm Transit Region Device Results (VMBE1898)

The time-domain simulation results in Fig. 9.5, show stable oscillation at 106 GHz. The manufactured device yielded a maximum fundamental power of ~22 mW at 94 GHz (that rolled off rapidly with frequency), the highest ever reported for a GaAs Gunn device at this frequency: the device has not yet been tested at second-harmonic and so no data is available. Again the time-domain solutions are in agreement with the measured data.

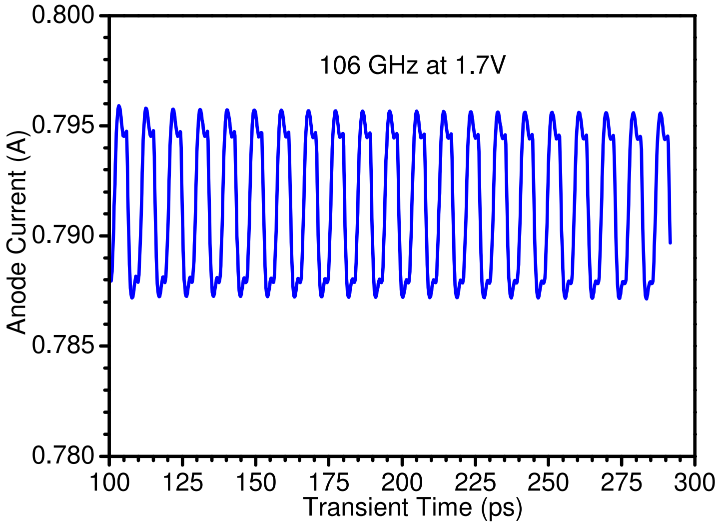

Fig. 9.5 **The simulated fundamental frequency time-domain response of a device fabricated from VMBE1898 (0.7 µm transit length) at an external bias of 1.7V, temperature 300K.**

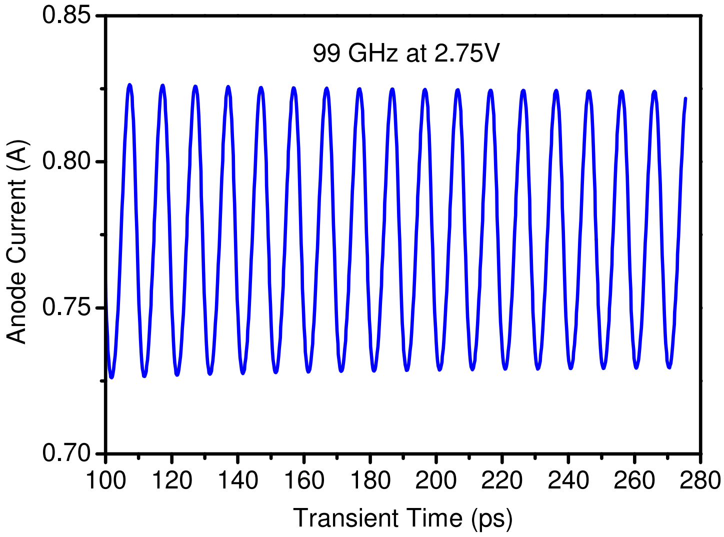

Fig. 9.6 **The simulated fundamental frequency time-domain response of a device fabricated from VMBE1898 (0.7 µm transit length) at an external bias of 2.75 V, temperature 300K.**

A second time domain simulation was performed for this model at a higher external bias voltage of 2.75V. A drop in the oscillation frequency to 99 GHz (Fig. 9.6) was observed along with an increase in the peak-to-peak current oscillation from about 7.5 mA to about 100 mA. In addition, the oscillation observed was sinusoidal in nature and did not exhibit the deformation at the peaks observed in Fig. 9.5 [104]. This again is in agreement with the expected behaviour for a device outlined in chapter 6 section 6.4.

9.2.5 0.4 µm – 0.6 µm Transit Region Device Results (XMBE189)

Having gained sufficient confidence in the models with transit regions down to 0.7 µm from the excellent agreement between simulated and measured results, the model was then extended to devices with even shorter transit regions. Extensive DC modelling coupled with empirical data and device theory initially pointed to a transit region of 0.4 µm as the minimum capable of supporting stable oscillation [102]. It is noted that time-domain simulations were not available at the time due to issues with computational solution convergence. After successive iterations simulation suggested that the optimal transit region carrier concentration level was 5.4 x10^{16} cm^{-3} and spike carrier concentration level was 1x10^{18} cm^{-3}.

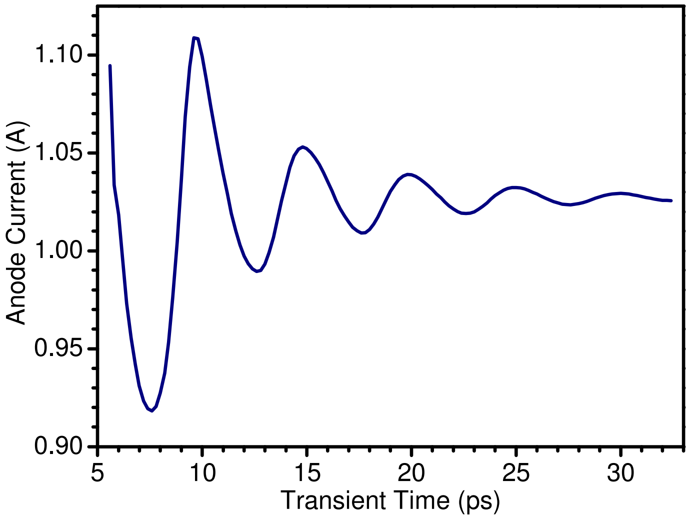

Fig. 9.7 The simulated fundamental frequency time-domain response of a device fabricated from XMBE189 (0.4 µm transit length) at an external bias of 3.5V, temperature 300K.

The material was gown and devices fabricated and tested. The modelled and measured DC I-V curves again matched very well as discussed in chapter 8. However, although showing a negative differential resistance region in the forward bias DC I-V characteristic, the fabricated device did not oscillate, presumably due to the energy relaxation time of electrons in the GaAs being larger than that required to support sustained oscillation in the device. This was later confirmed with time-domain simulations of the device, the results of which are shown in Fig. 9.7 where a decaying oscillation is observed. Subsequent investigation showed that the shortest transit region length capable of supporting sustained oscillation in this type of GaAs device is approximately 0.7 µm.

9.3 Time-Domain Response with a Resonant Cavity

The accurate physical modelling of Gunn diodes requires them to be mounted in an oscillator circuit. The circuit provides DC power, and couples out the generated RF power. Taking into account a particular oscillator in order to compare modelled/measured results is challenging due to the interaction between the diode and the circuit. The results presented here are for a model that accurately computes the behaviour of an advanced Gunn diode mounted in a cavity. The resonant cavity comprised of lumped-element LC parallel circuit, resistive loss R is in series with the L.

Following previous successful development of physical models using SILVACO^{TM} to predict the DC characteristics and time domain analysis of graded gap Gunn diodes given its epitaxial structure and physical geometry, the modelling work was extended to produce time-domain response of sub-micrometer transit length device (0.7 µm transit region length) mounted in a resonant cavity. The time-domain response allowed analyzing dipole domain formation and transit region scaling effects on it.

9.3.1 Dipole Domain Formation

The dipole domains are nucleated in the transferred electron devices due to doping inhomogeneities [9, 58]. The dipole nucleates from the cathode, grows to a stable size and drift towards the anode. The dipole consists of an accumulation and a depletion region with an associated electric field gradient. The electric fields builds after the domain reaches the anode and a new dipole is formed. The dipole domains cyclic formation results in current oscillations. This effect is successfully modelled. Its formation in half cycle in the transit region (Fig. 9.8) is in agreement with [9, 58], which nucleate at the cathode, grows in size and drifts towards the anode.

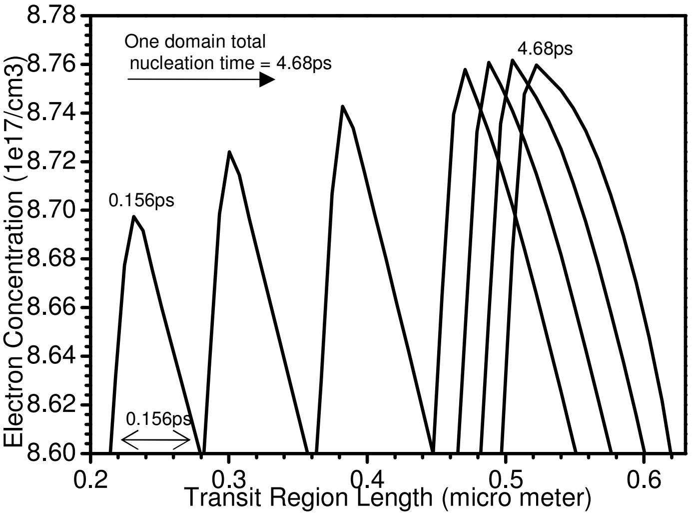

Fig. 9.8 Spatial dipole domain profiles in the transit region, for a 0.7 µm transit length device. These are plotted at an applied bias of 3V at time, starting at 0.156ps, in one oscillation period T=4.68 ps. The domain first grows to a maximum size and then drifts to the anode before it collapses there and a new domain nucleates.

The dipole domain formation is shown in appendix C. The two dipole domain formation cycles illustrates the complete RF cycle i.e. for one period whereas half period is shown by one dipole domain cycle (Fig.9.8). The dipole domain formation is cyclic and it repeats as a function of time to provide steady state RF oscillations. In appendix C, the figure shows the increased carrier concentration in the transit region as a function of time which shows nucleation, travel and finally collapse of the dipole domain. In a complete cycle a total of 72 graphs were saved and plotted in the TonyPlot^{TM}. The graphs were saved after every 0.158ps during time domain simulations. It took 9.36ps for the domain to complete a RF cycle, thereby providing 106.8 GHz ($f = \frac{1}{t} = \frac{1}{9.36} \simeq 107 GHz$). It is in agreement with theoretical calculations, discussed in chapter 4 and chapter seven section 7.2.5, ($f = \frac{v}{l} = \frac{7.6\times10^4}{0.7\times10^{-6}} \sim 108 GHz$). The results are also in agreement with experimental measurements.

9.3.2 Modelled Device with Resonant Cavity Time-Domain Results

The modelled device has a predicted fundamental power of 55 mW at 94 GHz at an applied bias of 3V (Fig. 9.9) when resistive losses of 0.9 Ohms were taken into account (from matching of the DC I-V curves). The manufactured device, on the other hand, delivered fundamental power of 22 mW at 94 GHz (applied bias 3V) and 21 mW at 96 GHz (applied bias 2.5V). These are the highest powers ever reported for a GaAs Gunn operating in fundamental mode at these frequencies. The modelled output power could be matched to the experimentally observed ones when the resistive losses were increased by 1.1 Ohms to 1.8 Ohms. The higher modelled values are due to the ideal high quality factor Q cavity assumed in the model, which clearly shows that more power can be extracted from these devices by minimizing waveguide losses and device package parasitic.

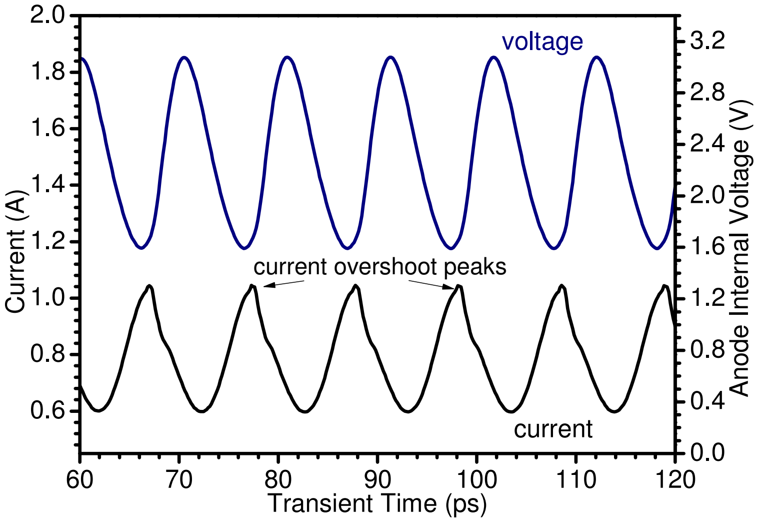

Fig. 9.9 Time-domain stable oscillation at 3 V with C_{diode} = 0.158 pF. The lumped-element LC parallel circuit values are L= 3.16 pH and C= 0.403 pF. The main loss R=0.9 Ohms is in series with the L. The current overshoot peaks are in agreement with [9] which are due to electron experiencing energy and momentum inertial effects at high frequencies.

9.4 Conclusion

The results of the time-domain simulations for 77 GHz (1.65 µm transit region device) devices with a range of epitaxial structures, 125 GHz second harmonic device, ~100 GHz fundamental device and ~200 GHz fundamental device have been presented. These simulations established the limits of transit region length capable of supporting a steady-state (non-decaying) oscillation. These simulations allowed performing large-signal device characterizations and comparing to measured results.

It was shown that that the shortest transit region length capable of supporting sustained oscillation in GaAs device is approximately 0.7 µm (~100 GHz fundamental device).

The modelling work was extended to produce time-domain response of sub-micrometer transit length device (0.7 µm transit region length) mounted in a resonant cavity. The resonant cavity designed in SILVACO^{TM} was presented that comprised of lumped-element LC parallel circuit, resistive loss R is in series with the L. The time-domain response allowed analyzing dipole domain formation and transit region scaling effects on it.

It was shown that the dipole domains are nucleated in the transferred electron devices due to doping inhomogeneities. Its formation in the transit region was shown to be in agreement with published literature, which nucleates at the cathode, grows in size and drifts towards the anode. In a 0.7 µm transit region length device the two dipole cycles completed one RF time period thereby providing ~107 GHz which was shown to be in agreement with theory and measured results.

Chapter 10 Conclusion and future work

10.1 Conclusions

The ever increasing demand for THz devices and the huge market potential for THz systems have led to an enormous amount of research in the area for a number of years. Of all solid state millimetre wave oscillators, Gunn diodes have the potential to be built into low cost, high-frequency and high output power sources. These sources will 'power' future systems in the Terahertz (THz) region. This region of the electromagnetic spectrum has attracted enormous attention due to emerging applications in the field. These applications, including automotive Autonomous Cruise Control (ACC), millimetre-wave imaging systems, missile guidance, smart munitions and millimetre-wave radar systems have made the requirement for physically-based models using model-experiment approach a pressing need.

It was shown that a combination of Gunn and mixer diodes will make ideal power source for future THz systems using a two-stage module with the initial frequency source provided by the high frequency Gunn diodes. The output from these diodes is then coupled into a multiplier module. The multiplier provides higher frequencies by the generation of harmonics of the input signal by means of a non-linear element. The non-linear element is provided by a Schottky diode Varactor with low RC time constants to increase efficiency.

Design considerations of the microstrip and multiplier block were presented. The semiconductor materials for such a complete device including modelling, design and testing; focusing in depth on the Gunn diode module and Schottky diode were also discussed.

A Gunn diode physical model has been developed using state of art software SILVACO^{TM}. Thorough understanding of device physics was achieved to develop the model. The model development included device physical structure building, material properties specification, physical models definition and using appropriate biasing conditions.

The physical models (and their associated parameters) used have been presented and discussed. They were carefully selected for each layer, which depended on the material and carrier concentration in the region. It included Mobility models, Carrier Generation-recombination models, Carrier Statistics and Transport models and GIGA^{TM} Self Heating Simulator. The analytic function based on the work of Caughey and Thomas is used for modelling field dependant mobility in the contact layers, spacer layers, AlGaAs launcher and also the transit region for field strengths below the negative differential mobility (NDM) threshold. For field strengths in the transit region above the NDM threshold, the Barnes NDM model is used. The Shockley-Read-Hall (SRH) recombination model is applied in the nominally undoped $Al_xGa_{(1-x)}As$ barrier. The SRH concentration-dependent lifetime model is used in the rest of the device to account for the various silicon impurity concentrations. The hydrodynamic model which provides realistic results and better convergence was implemented in the Gunn diode model to solve energy balance transport equations. Finally, it is shown that where the platform did not allow sufficient flexibility to accurately account for the interdependency of parameters, appropriate C-language functions were written and incorporated through the in-built C-interpreter

GIGA^{TM}, a self heating simulator available in SILVACO^{TM}, was used to simulate the device local temperature, self-heating, lattice heat flow and heatsinking effects. It was used with the definition of heat sinks at the cathode and anode respectively. This is based on the models suggested by Wachutka and accounts for Joule heating along with heating and cooling due to carrier generation and recombination. The Wachutka models were discussed in detail.

A precise and accurate physical model was developed for determining device performance of an advanced graded gap GaAs-AlGaAs Gunn diode. The initial goal of the work was to reproduce experimental performances of a Gunn diode commercially manufactured by e2v Technologies Plc. used in second harmonic in 77 GHz ACC systems.

The simulations have confirmed basic device theory and measured data in that the current asymmetry (I_{asym}), can be used to evaluate injector performance, and in particular, doping spike carrier concentrations. The doping spike carrier concentration optimum value $1\times10^{18}cm^{-3}$ was determined using modelled-measured approach.

The model DC characteristics comparison with measured data was presented over a range of temperatures. The measured data included the DC characteristics of 77 GHz (1.65 µm transit region device) devices with a range of epitaxial structures, 125 GHz second harmonic device, ~100 GHz fundamental device and ~200 GHz fundamental device. A good match between measured and simulated I-V curves validates the choice of physical models and parameters used.

The results of the time-domain simulations for 77 GHz (1.65 µm transit region device) devices with a range of epitaxial structures, 125 GHz second harmonic device, ~100 GHz fundamental device and ~200 GHz fundamental device were presented. These simulations established the limits of transit region length capable of supporting a steady-state (non-decaying) oscillation. These simulations allowed performing large-signal device characterizations and comparing to measured results. It was shown that that the shortest transit region length capable of supporting sustained oscillation in GaAs device is approximately 0.7 µm (~100 GHz fundamental device).

The modelling work was extended to produce time-domain response of sub-micrometer transit length device (0.7 µm transit region length) mounted in a resonant cavity. The resonant cavity designed in SILVACO^{TM} was presented which comprised of lumped-element LC parallel circuit, resistive loss R in series with the L. The time-domain response allowed analyzing dipole domain formation and transit region scaling effects on it.

10.2 Directions for Future Research

It was shown that the oscillator circuit effectively determines the oscillation frequency and so in turn affects both the dynamics of the high-field domain within the device’s transit region and therefore the dynamic reactance of the device itself. It may not be accurate to simply extract a small-signal s-parameter model of the Gunn device from the SILVACO^{TM} model and use this in conjunction with the HFSS^{TM} model of the oscillator (i.e. terminate the diode port in the HFSS^{TM} simulation with a SILVACO^{TM} generated s-parameter matrix). This would not enable the effects of the oscillator circuit to be taken into account when computing a device’s time-domain response.

Two novel approaches are proposed to merge SILVACO^{TM} and HFSS^{TM} models. It would aid in the development high power THz sources using multipliers. The techniques include the lumped element model for SILVACO^{TM} and taking into account Gunn diode domain growth and propagation in the HFSS^{TM} model. These are discussed next.

10.2.1 Lumped Element Model for SILVACO^{TM}

The equivalent frequency-domain behaviour of a second harmonic oscillator circuit is simulated using HFSS^{TM} at the fundamental oscillation frequency and the equivalent circuit parameters at this frequency extracted: this can then be used to define a suitable circuit model for inclusion in the SILVACO^{TM} simulations. From simulation of the same HFSS^{TM} model at second harmonic frequencies, the values of the equivalent circuit elements at this frequency can be extracted and used in a lumped element equivalent circuit model to estimate the conversion efficiency to second harmonic. This will allow estimation of the second harmonic output power for a device mounted in the oscillator. This will ultimately enable the effects of both variations in the semiconductor device and the oscillator geometry to be evaluated simultaneously.

10.2.2 Taking into account Gunn Diode Domain Growth and Propagation

In order to account for the dynamic nature of the depletion region when simulating the electromagnetic (EM) behaviour of the oscillator circuit (leading to degradation in accuracy of the model as a whole) the growth of the high-field domain will need to be adequately represented within the EM model. A proposed technique to achieve this is to approximate the continuous process of domain growth and propagation in the HFSS^{TM} model by treating it as a sequence of discrete stages, each with an individual HFSS^{TM} model in which the length and/or the position of the dielectric region is altered. The size, position and material properties of the depletion region would again be estimated from an initial SILVACO^{TM} result. A time-varying series of equivalent circuit parameters could then be extracted, and using curve fitting, continuous functions approximated for each of the oscillator circuit spice model parameters. Although initially seeming labour intensive, this process could be simplified through exploitation of the parametric sweep functionality of HFSS^{TM}. Suitable code would then be written to update the values of the equivalent spice circuit model used to represent the oscillator circuit in the SILVACO^{TM} time-domain simulations, as the oscillation cycle progresses.

Appendix – A

Gunn diode models and material parameters

SILVACO^{TM} code for a 0.7µm transit region length Gunn Diode model is presented. The statements with hash (**#**) are the remarks which are ignored during simulation code execution. A line continuation operator '\' shows that code continues in the next line. The C-Interpreter file path is arbitrary.

```
go atlas
title "Gunn Diode model VMBE 1898 – 0.7µm transit region length "
set setpath=C:/Silvaco_PhD/00-Simulations/C-Interpreter

# SECTION 1: Mesh input

mesh auto cylindrical

x.mesh loc=0.0 spac=9.75
x.mesh loc=9.75 spac=9.75
x.mesh loc=19.5 spac=5.0
x.mesh loc=28.2 spac=5.0
x.mesh loc=37.0 spac=10.0
x.mesh loc=46.1 spac=10.0

y.mesh loc=0.0 spac=5.0
y.mesh loc=10.00 spac=1.0
y.mesh loc=10.250 spac=0.125
y.mesh loc=10.750 spac=0.05
y.mesh loc=10.7550 spac=0.001
y.mesh loc=10.7650 spac=0.005
y.mesh loc=10.7750 spac=0.005
y.mesh loc=10.7850 spac=0.005
y.mesh loc=10.7950 spac=0.005
y.mesh loc=10.8050 spac=0.005
y.mesh loc=10.8150 spac=0.005
y.mesh loc=10.82000 spac=0.005
y.mesh loc=11.52000 spac=0.01
y.mesh loc=12.02000 spac=0.1
y.mesh loc=20.02000 spac=0.5
y.mesh loc=20.27000 spac=0.125
```

```
y.mesh loc=22.27000 spac=0.25

# SECTION 2: Structure Specification (regions, electrodes and delta doping)

        # Regions
region num=1 name=air material=air x.min=0.0 x.max=19.5 y.min=10.000 y.max=22.2700
region num=2 name=contact_c material=GaAs x.min=19.5 x.max=28.2 y.min=10.2500 \
        y.max=10.7500
region num=3 name=spacer material=GaAs x.min=19.5 x.max=28.2 y.min=10.7500 \
        y.max=10.7550
region num=4 name=AlGaAs_1.7 material=AlGaAs x.comp=0.017 x.min=19.5 x.max=28.2 \
        y.min=10.75500 y.max=10.76500
region num=5 name=AlGaAs_8 material=AlGaAs x.comp=0.08 x.min=19.5 x.max=28.2 \
        y.min=10.76500 y.max=10.77500
region num=6 name=AlGaAs_16 material=AlGaAs x.comp=0.16 x.min=19.5 x.max=28.2 \
        y.min=10.77500 y.max=10.78500
region num=7 name=AlGaAs_24 material=AlGaAs x.comp=0.24 x.min=19.5 x.max=28.2 \
        y.min=10.78500 y.max=10.79500
region num=8 name=AlGaAs_32 material=AlGaAs x.comp=0.32 x.min=19.5 x.max=28.2 \
        y.min=10.79500 y.max=10.80500
region num=9 name=spacer material=GaAs x.min=19.5 x.max=28.2 y.min=10.80500 \
        y.max=10.81500
region num=10 name=spike material=GaAs x.min=19.5 x.max=28.2 y.min=10.81500 \
        y.max=10.82000
region num=11 name=transit material=GaAs x.min=19.5 x.max=28.2 y.min=10.82000 \
        y.max=11.52000
region num=12 name=contact_amaterial=GaAs x.min=19.5 x.max=28.2 y.min=11.52000 \
        y.max=12.02000
region num=13 name=substrate material=GaAs x.min=19.5 x.max=28.2 y.min=12.02000 \
        y.max=20.02000
region num=14 name=air material=air x.min=28.2 x.max=46.1 y.min=10.000 y.max=22.2700

        # Electrodes
elec num=1 name=anode material=Gold x.min=19.5 x.max=28.2 y.min=20.02 y.max=20.27
elec num=2 name=cathode material=Gold x.min=19.5 x.max=28.2 y.min=10.0 y.max=10.25
elec num=3 name=anode material=Gold x.min=19.5 x.max=28.2 y.min=20.27 y.max=22.27
elec num=4 name=cathode material=Gold x.min=0.0 x.max=46.1 y.min= 0.0 y.max=10.00

        # Delta doping
doping uniform n.type conc=5e18 Region=2
doping uniform n.type conc=1e18 Region=10
doping uniform n.type conc=3.5e16 Region=11
```

```
doping uniform n.type conc=5e18 Region=12
doping uniform n.type conc=2e18 Region=13

# SECTION 3: Material Parameters Definitions

        # Regional and Band Parameters (band gap)
material name=AlGaAs_1.7 eg300=1.445199 permittivity=13.1507 nc300=6.83e17 \
         nv300=1.30e19
material name=AlGaAs_8 eg300=1.52376 permittivity=12.968 nc300=1.60e18 nv300=1.33e19
material name=AlGaAs_16 eg300=1.62352 permittivity=12.736 nc300=2.77e18 nv300=1.37e19
material name=AlGaAs_24 eg300=1.72328 permittivity=12.504 nc300=3.93e18 nv300=1.41e19
material name=AlGaAs_32 eg300=1.82304 permittivity=12.272 nc300=5.10e18 nv300=1.46e19

        # Recombination Parameters (SRH)
material name=AlGaAs_1.7 taun0=4.93e-9 taup0=2e-8 NSRHN=4.92e16 NSRHP=4.92e16
material name=AlGaAs_8 taun0=4.68e-9 taup0=2e-8 NSRHN=4.60e16 NSRHP=4.60e16
material name=AlGaAs_16 taun0=4.36e-9 taup0=2e-8 NSRHN=4.20e16 NSRHP=4.20e16
material name=AlGaAs_24 taun0=4.04e-9 taup0=2e-8 NSRHN=3.80e16 NSRHP=3.80e16
material name=AlGaAs_32 taun0=3.72e-9 taup0=2e-8 NSRHN=3.40e16 NSRHP=3.40e16

        # Mobility Parameters (caughey Thomas)
mobility name=substrate mu1n.caug=800 alphan.caug=-0.9 betan.caug=-2.2 \
        gamman.caug=-3.1 deltan.caug=0.5 ncritn.caug=1e17 mu2n.caug=2300
mobility name=Contact_A mu1n.caug=800 alphan.caug=-0.9 betan.caug=-2.2 \
        gamman.caug=3.1 deltan.caug=0.5 ncritn.caug=1e17 mu2n.caug=1350
mobility name=Transit mu1n.caug=800 alphan.caug=-0.9 betan.caug=-2.2 \
        gamman.caug=-3.1 deltan.caug=0.5 ncritn.caug=1e17 mu2n.caug=6300
mobility name=Spike mu1n.caug=800 alphan.caug=-0.9 betan.caug=-2.2 \
        gamman.caug=-3.1 deltan.caug=0.5 ncritn.caug=1e17 mu2n.caug=2650
mobility name=Contact_C mu1n.caug=800 alphan.caug=-0.9 betan.caug=-2.2 \
        gamman.caug=3.1 deltan.caug=0.5 ncritn.caug=1e17 mu2n.caug=1350
mobility material=GaAs betan=1
mobility material=AlGaAs gamman=2

        #Giga – Self Heating Simulator Model Parameters
## k(T) = (tc.const) / [(T/300)]^tc.npow
material tcon.power
material f.tcond="$setpath/tcond.lib"

        # C Interpreter Functions

material material=AlGaAs f.bandcomp="$setpath/bandcompAl.lib"
```

```
material material=GaAs f.bandcomp="$setpath/bandcomp.lib"
material material=AlGaAs f.vsatn="$setpath/vsatn_7e6.lib"
material material=GaAs f.vsatn="$setpath/vsatn_7e6.lib"
mobility material=AlGaAs f.enmun="$setpath/enmun.lib"
material material=GaAs f.munsat="$setpath/munsat_GaAs.lib"
material material=AlGaAs f.munsat="$setpath/munsat.lib"

        #Thermal Contacts for GIGA™
thermcontact number=1 name=Anode    ext.temper=300
thermcontact number=2 name=Cathode ext.temper=300

# SECTION 3: Models Definitions
models material=GaAs consrh conmob analytic fldmob evsatmod=1 b.elec=2
models material=AlGaAs srh fldmob evsatmod=0 mobtem.simpl b.elec=2
models lat.temp joule.heat gr.heat
models material=AlGaAs cubic35
models hcte.el boltzmann temperature=300 print

# SECTION 4: Initial solution
        # Method
method carriers=1 electrons
output e.field e.mobility e.temp e.velocity con.band val.band charge flowlines devdeg
method block newton itlimit=100 trap atrap=0.5 maxtrap=10 vsatmod.inc=0.001

        # Contacts
contact all neutral
#contact name=anode neutral resistance=0.9 inductance=3.16e-12 capacitance=0.403e-12 \
#           resonant
contact name=anode neutral resistance=0.9
contact name=cathode neutral

solve init
solve
save outfile=1898_P_0pt7Transit_298Ka.str

# SECTION 5a: DC I-V Simulations – Forward bias
log outf=1898_P_0pt7Transit_298K.log
solve vanode=0.0  vstep=0.1 vfinal=4.0 name=anode
save outfile=1898_P_0pt7Transit_Final_298K.str

log off
quit
```

```
# SECTION 5b: DC I-V Simulations – Reverse bias
log outf=1898_N_0pt7Transit_298K.log
solve vanode=0.0  vstep=-0.1 vfinal=-4.0 name=anode
save outfile=1898_N_0pt7Transit_Final_298K.str

log off
quit

# SECTION 5c: Time Domain Simulations

solve init

save outfile=1898_ATLAST_HS.str

log outfile=1898_Trans_1_HS.log
solve vanode=2.5 ramptime=2.7e-11 tstop=2.7e-11 dt=1e-12
save outfile=1898_Trans_1_HS.str

        # Extract I-V Characteristic above which the Negative Resistance begins
extract name="1898_Trans_HS.dat" curve(vint."anode", i."anode") outf="1898_Trans_HS.dat"
extract name="Icrit" max(i."anode")
extract name="UMax" max(vint."anode")
extract name="Ucrit" x.val from curve(vint."anode", i."anode") where y.val=$Icrit
extract name="Ecrit" $Ucrit/7e-5

        # Time Domain Simulation at 2.5V Constant External Bias
log outfile=1898_Trans_2_HS.log
solve tstop=12e-11 dt=2e-11 outfile=1898_Trans_2_x0 master
log off

extract the oscillation frequency by measuring the time for 4 periods
extract init inf="1898_Trans_2_HS.log"
extract name="v_ave" ave(vint."anode")
extract name="t1" x.val from curve(time, vint."anode") where y.val=$"v_ave"
extract name="t2" x.val from curve(time, vint."anode") where y.val=$"v_ave" and val.occno=7
extract name="delta" ($"t2" - $"t1") / 3
extract name="f@2pt5V" 1 / $"delta"

        # Ramp-up to 3.0 V External Bias
load inf=1898_Trans_1_HS.str master
solve previous
solve vanode=3 ramptime=2.7e-11 tstop=2.7e-11 dt=1e-12
```

```
save outfile=1898_Trans_3_HS.str

        # Time Domain Simulation at 3.0V Constant External Bias
log outfile=1898_Trans_3_HS.log
solve tstop=12e-11 dt=2e-11 outfile=1898_Trans_3_x0 master
log off

extract init inf="1898_Trans_3_HS.log"
extract name="v_ave" ave(vint."anode")
extract name="t1" x.val from curve(time,vint."anode") where y.val=$"v_ave"
extract name="t2" x.val from curve(time,vint."anode") where y.val=$"v_ave" and val.occno=7
extract name="delta" ($"t2" - $"t1") / 3
extract name="f@3V" 1 / $"delta"

quit
```

Appendix – B

Schottky Diode – SILVACO^{TM} code

SILVACO^{TM} code for a 14µm diameter Schottky diode is presented. The statements with hash (**#**) are the remarks which are ignored during simulation code execution. A line continuation operator '\' shows that code continues in the next line. The C-Interpreter file path is arbitrary..

SILVACO^{TM} DeckBuild^{TM} code

```
go atlas
title "Schottky 4 multipliers 14um diameter"

# SECTION 1: Mesh input

mesh width = 120 auto
x.mesh  loc=0.0 spac=0.5
x.mesh  loc=1.5 spac=0.5
x.mesh  loc=2.0 spac=0.25
x.mesh  loc=2.5 spac=0.5
x.mesh  loc=2.994 spac=0.01
x.mesh  loc=2.995 spac=0.01
x.mesh  loc=3.0 spac=0.01
x.mesh  loc=3.5 spac=0.25
x.mesh  loc=5.25 spac=0.15

y.mesh loc=-0.0605 spac=0.1
y.mesh loc=-0.033 spac=0.001
y.mesh loc=0.0 spac=0.001
y.mesh loc=0.35 spac=0.01
y.mesh loc=3.35 spac=0.2
y.mesh loc=6.35 spac=1.2
y.mesh loc=14.35 spac=2.0

# SECTION 2: Structure Specification (regions, electrodes and delta doping)

        # Regions

region num=1 name="Cap" material=InGaAs y.min=-0.0605 y.max=-0.033 x.comp=0.2
```

```
region num=2 name="Cap1" graded material=InGaAs y.min=-0.033 y.max=0.0 compx.top=0.2 \
        compx.bottom=0.9999
region num=3 name="Supply" material=GaAs y.min=0.0 y.max=0.35 x.min=0.0 x.max=3.00
region num=4 name="Supply1" material=GaAs y.min=0.0 y.max=0.35 x.min=3.5 x.max=5.25
region num=5 name="Channel" material=GaAs y.min=0.35 y.max=3.35
region num=6 name="Buffer" material=GaAs y.min=3.35 y.max=6.35
region num=7 name="Subs" material=GaAs y.min=6.35 y.max=14.35
region num=8    material=Air y.min=-0.0605 y.max=0.0 x.min=2.995 x.max=5.25
region num=9    material=Air y.min=0.0 y.max=0.35 x.min=2.995 x.max=3.50

        # Electrodes

elec  num=2 name=anode material=gold x.min=3.5 x.max=5.25 y.min=0.0 y.max=0.0
elec  num=1 name=cathode material=gold x.min=0.0 x.max=2.994 y.min=-0.0605 y.max=-0.0605

        # Delta Doping

Doping uniform n.type conc=5e18 region=1
Doping uniform n.type conc=5e18 region=2
Doping uniform n.type conc=1.8e17 region=3
Doping uniform n.type conc=1.8e17 region=4
Doping uniform n.type conc=5e18 region=5

# SECTION 3: Material Parameters Definitions
## The physical parameters for InGaAs are defined in the following sub-sections. Default
## parameters are selected for GaAs

        # Regional and Band Parameters (band gap)

material material=InGaAs f.bandcomp="C:/SILVACO_PhD/C-Interpreter/bandcomp_InGaAs.lib"
material region=2 align=0.34
material region=3 align=0.36

        # Recombination Parameters (SRH)

material material=InGaAs taun0=3e-10 taup0=1e-8 NSRHN=9e17 NSRHP=8e17

        # Saturation Velocities and Auger Recombination Parameters

material material=InGaAs vsatn=7.67e6 vsatp=6.01e6
material material=InGaAs f.vsatn="C:/SILVACO_PhD/C-Interpreter/vsat_InGa.lib"
material material=InGaAs augn=2e-27
```

```
          # Mobility Parameters (caughey Thomas)

mobility material=InGaAs mu1n.caug=2000 mu2n.caug=12000 mu1p.caug=050 mu2p.caug=400\
          ncritn.caug=6.4e17 ncritp.caug=7.4e17
mobility material=InGaAs alphan.caug=0 alphap.caug=0 betan.caug=0 betap.caug=0 \
          gamman.caug=0 gammap.caug=0 deltan.caug=0 deltap.caug=0
mobility material=InGaAs f.enmun="C:/SILVACO_PhD/C-Interpreter/enmun_In.lib"
material material=InGaAs f.munsat="C:/SILVACO_PhD/C-Interpreter/munsat_In.lib"

# SECTION 3: Models Definitions

models fldmob auger consrh fermidirac temperature=300 print

# SECTION 4: Initial Solution

output e.field e.mobility e.temp e.velocity con.band val.band charge flowlines

          # Contacts

contact name=anode  workfunc=4.815
contact name=cathode

method block newton itlimit=100 trap atrap=0.5 maxtrap=10 vsatmod.inc=0.001
solve init
save outf=Schottky_Ohmic-Cap_Rev-14um-DIA.str

# SECTION 4: AC solution for plotting a C-V curve

solve vanode=0

log outf=AC_Schottky_14um-DIA.log  s.param inport=anode outport=anode y.param
solve vanode=0.0 vstep=-0.05 vfinal=-10.0  name=anode ac freq=1e9 fstep=10e9 nfsteps=9
save outf=AC_Schottky_Ohmic-ve14um-DIA.str

logoff

tonyplot AC_Schottky_14um-DIA.log

quit
```

Appendix – C

Dipole Domain Formation

1. One dipole formation showing the transit region electron concentration, zoomed between 16.4 and 16.9 cm^{-3}.

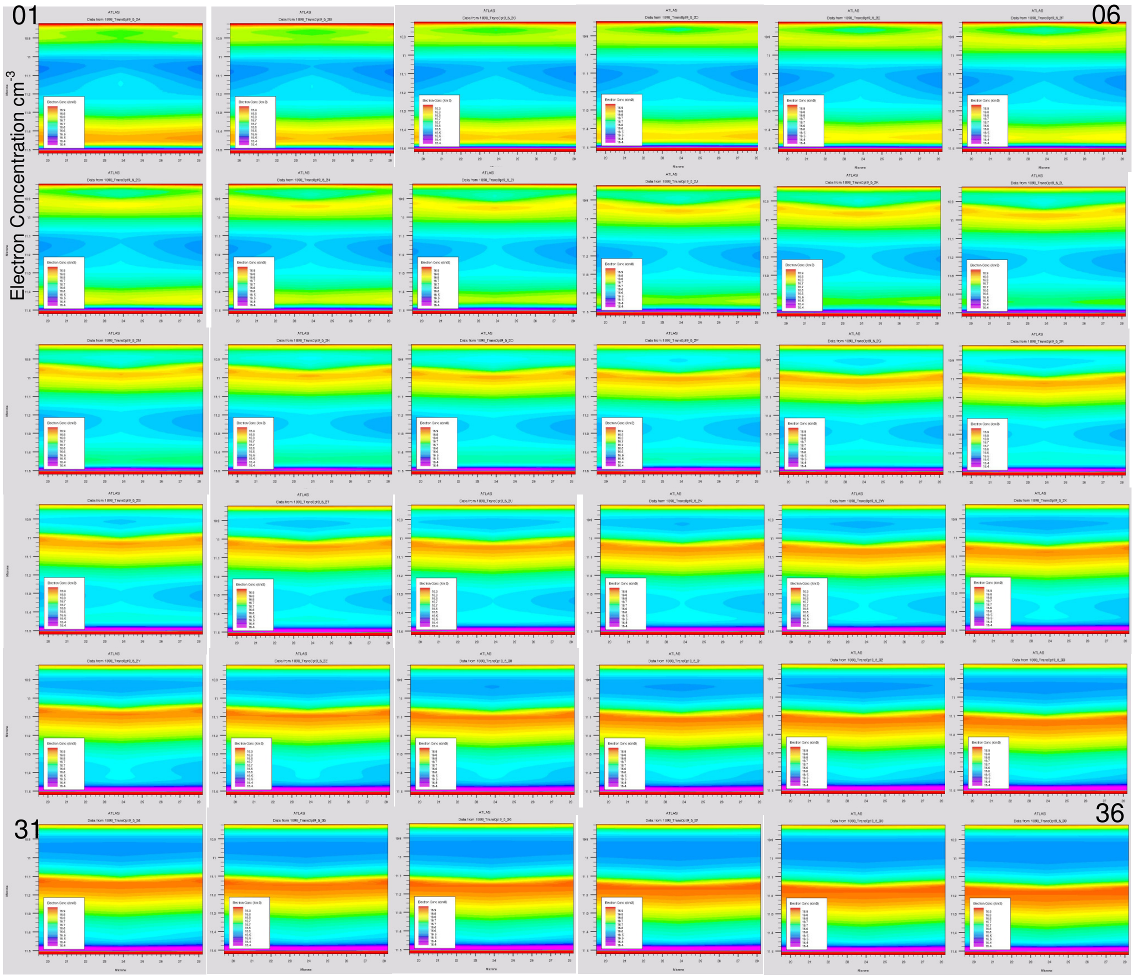

2. Two dipoles showing the transit region electron concentration, zoomed between 16.4 and 16.9 cm^{-3}.

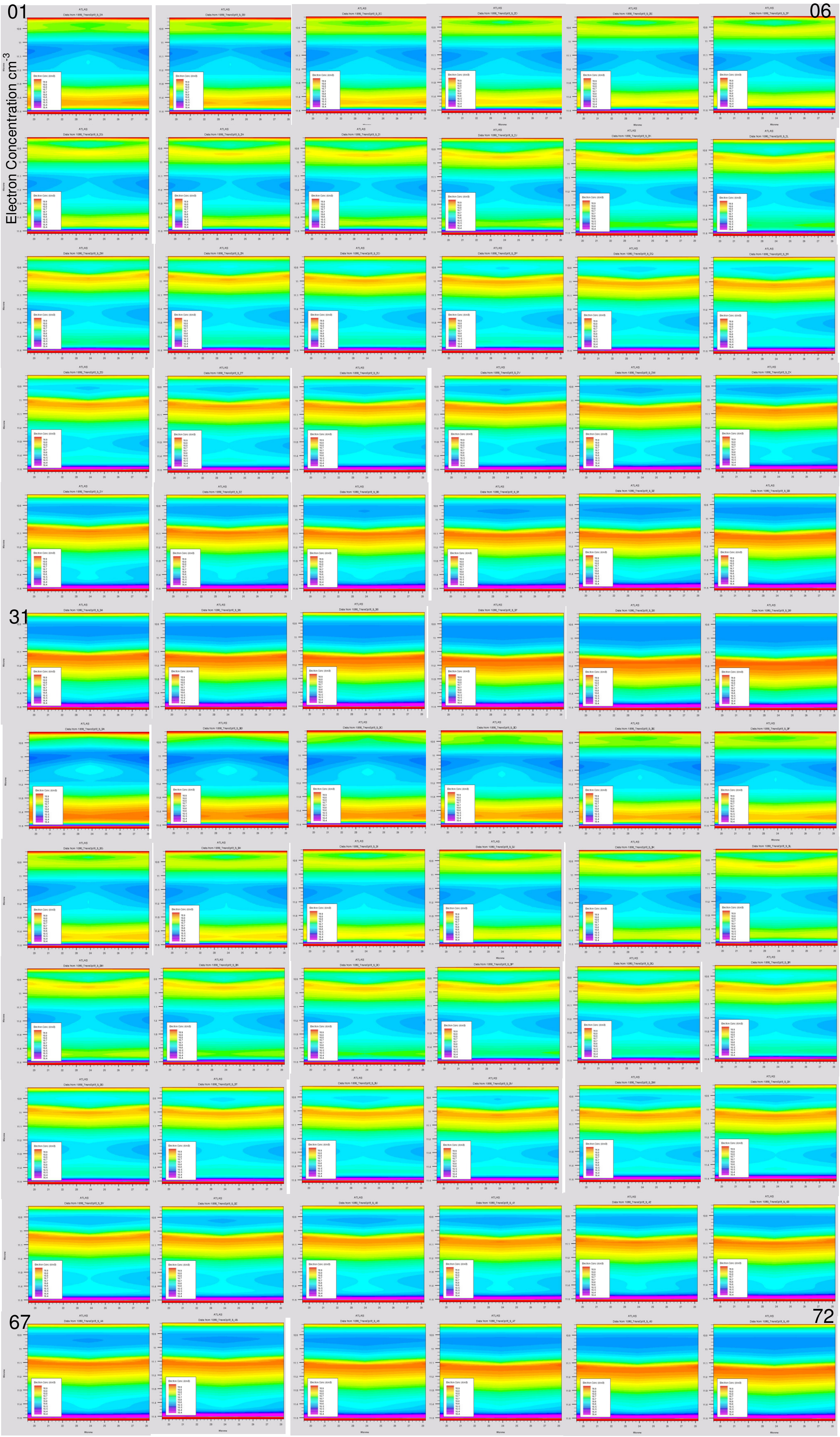
01
06
Electron Concentration cm -3
31
67
72

References

1. Sze, S.M., *High Speed Devices*. 1990: New York ; Chichester : Wiley.
2. Hobson, G.S., *The Gunn effect.* 1974. **Oxford : Clarendon Press**.
3. Sze, S.M., *Semiconductor Devices Physics and Technology*. 2nd edition 2002, New York: NY Willey.
4. Montanari, S., *Fabrication and Characterization of planar Gunn Diodes for Monolithic Microwave Integrated Circuits*, in *RWTH*. 2005, University of Aachen.
5. Townsend, S.M., *AlGaAs/GaAs Graded Gap Gunn Diodes for Autonomous Intelligent Cruise Control Radar Applications*, in *EEE, M&N Group*. 1999, UMIST: Manchester.
6. Gallerano, G.P. *Overview of Terahertz Radiation Sources*. in *Proceedings of the 2004 FEL Conference*. 2004.
7. *Electronic Warfare and Radar Systems Engineering Handbook*. 2 ed. 1997, Washington, D.C. 20361: Avionics Department. 1-298.
8. Shur, M. *Terahertz technology: Devices and applications*. in *Proceedings of ESSDERC 2005: 35th European Solid-State Device Research Conference*. 2005.
9. Tait, G.B. and Krowne, C.M., *Efficient transferred electron device simulation method for microwave and millimeter wave cad applications.* Solid-State Electronics, 1987. **30**(10): p. 1025-1036.
10. Forster, A.A., *Hot electron injector Gunn diode for advanced driver assistance systems.* Applied physics. A, Materials science & processing, 2007. **87**(3): p. 545-58.
11. Montanari, S.S., *High frequency investigation of graded gap injectors for GaAs Gunn diodes.* Solid-state electronics, 2005. **49**(2): p. 245-50.
12. Couch, N.N.R., *High-performance, graded AlGaAs injector, GaAs Gunn diodes at 94 GHz.* IEEE electron device letters, 1989. **10**(7): p. 288-90.
13. N. Farrington, Carr, M., Sly, J. L., and Missous, M., *Development of an on-wafer test for rapid evaluation of doping spike carrier concentration levels in commercially manufactured GaAs Gunn diodes for automotive radar applications*. in *Interational Conferance on Compound Semiconductor Manufacturing Technology (CSManTech'08)*. 2008. Chicago, USA.
14. Phillips, T.T.G., *Submillimeter astronomy [heterodyne spectroscopy].* Proceedings of the IEEE, 1992. **80**(11): p. 1662-78.
15. Tonouchi, M., *Cutting-edge terahertz technology*, in *Nat Photon*. 2007. p. 97-105.
16. Siegel, P.H., *Terahertz technology.* IEEE transactions on microwave theory and techniques, 2002. **50**(3): p. 910-28.
17. Siegel, P.H. *THz applications for outer and inner space*. in *17th International Zurich Symposium on Electromagnetic Compatibility*. 2006.
18. Carr, G., et al., *High-power terahertz radiation from relativistic electrons.* Nature, 2002. **420**(6912): p. 153-156.
19. Anwar, A. *Staying the course in the GaAs industry*. in *International Conference on Compound Semiconductor Manufacturing Technology.* 2005.

20. Gunn, J., *Microwave Oscillations of Current in III-V Semiconductors.* Solid State Communications, 1963. **1**(4): p. 88-91.
21. Esaki, L., *New Phenomenon in Narrow Germanium p-n Junctions.* Physical Review, 1958. **109**(2): p. 603.
22. Chang, L., Esaki L., and Tsu, R., *Resonant Tunneling in Semiconductor Double Barriers.* Applied physics letters, 1974. **24**(12): p. 593-595.
23. Read, W., *A proposed high-frequency, negative-resistance diode.* The Bell system technical journal, 1958. **37**(2): p. 401-446.
24. Ruegg, H.W., *A proposed punch-through microwave negative-resistance diode.* Electron Devices, IEEE Transactions on, 1968. **15**(8): p. 577-585.
25. Okabe, T., et al., *Bulk oscillation by tunnel injection.* Electron Devices, IEEE Transactions on, 1969. **16**(2): p. 251-251.
26. Elta, M.E. and Haddad, G.I., *High-Frequency Limitations of IMPATT, MITATT, and TUNNETT Mode Devices.* Microwave Theory and Techniques, IEEE Transactions on, 1979. **27**(5): p. 442-449.
27. Elta, M.E. and Haddad, G.I., *Large-signal performance of microwave transit-time devices in mixed tunneling and avalanche breakdown.* Electron Devices, IEEE Transactions on, 1979. **26**(6): p. 941-948.
28. Gunn, J.J.B., *Microwave oscillations of current in III-V semiconductors.* Solid State Communications, 1993. **88**(11): p. 883-886.
29. Streetman, B.G., *Solid state electronic devices*. 4th ed. Prentice Hall series in solid state physical electronics. 1995: Englewood Cliffs, N.J. : Prentice Hall, c1995.
30. Townsend, S. *Low resistance ohmic contacts to millimetre-wave graded gap Gunn diode oscillators*. in *Workshop on High Performance Electron Devices for Microwave and Optoelectronic Applications, EDMO*. 1997.
31. e2v Technologies Plc, *DC1279F-T 76–78GHz Gunn Diode Data sheet.*
32. Brown, E. R., Soderstrom, J. R., Parker, C. D., Mahoney, L. J., Molvar, K. M. and McGill, T. C., *Oscillations up to 712 GHz in InAs/AlSb resonant tunneling diodes.* Applied Physics Letters, 1991. **58**(20): p. 2291-2293.
33. Suzuki, S., Teranishi, A., Hinata, K., Asada, M., Sugiyama, H. and Yokoyama, H., *Fundamental oscillation up TO 831 GHz in GaInAs/AlAs resonant tunneling diode*. in *IEEE International Conference on Indium Phosphide & Related Materials, 2009. IPRM '09.* . 2009.
34. Sze, S.M. and Kwok K. Ng, *Physics of semiconductor devices*. 3rd ed. 2006, New York: Wiley-Blackwell.
35. Jun-ichi, N, Plotka, P., Makabe, H. and Kurabayashi, T., *GaAs TUNNETT diodes oscillating at 430-655 GHz in CW fundamental mode.* Microwave and Wireless Components Letters, IEEE, 2005. **15**(9): p. 597-599.
36. Elta, M., Fetterman, H., Macropoulos, W. and Lambert, J., *150 GHZ GAAS MITATT SOURCE.* Electron device letters, 1980. **1**(6): p. 115-116.
37. Robert LaGuerra, D.F., Ed Rerisi, *ABI (Automotive Radar/Lidar Systems) A component level market analysis of radar, lidar, ultrasonic, and optics-based automotive safety systems* 2004.
38. Pilgrim, N., Macpherson, R., Khalid, A., Dunn, G. and Cumming, D., *Multiple and broad frequency response Gunn diodes.* Semiconductor science and technology, 2009. **24**(10): p. 105010.
39. Pilgrim, N. J., Khalid, A., Li, C., Dunn, G. M. and Cumming, D. R. S., *Contact shaping in planar Gunn diodes.* physica status solidi (c), 2010. **8**(2): p. 313-315.

40. Perez, S., Gonzalez, T., Pardo, D. and Mateos, *Terahertz gunn-like oscillations in InGaAs/InAIAs planar diodes.* Journal of applied physics, 2008. **103**(9): p. 094516.
41. Huang, J., Yang, H., Tian, C., Dong, J., Zhang, H. and Guo, T., *Design and manufacture of planar GaAs Gunn diode for millimeter wave application.* Chinese Physics B, 2010. **19**(12): p. 127203.
42. Li, C., Khalid, A., Pilgrim, N., Holland, M., Dunn, G. and Cumming, D., *Novel Planar Gunn Diode Operating in Fundamental Mode up to 158 GHz.* Journal of physics. Conference series, 2009. **193**: p. 012029.
43. Crowe, T.T.W., *Terahertz GaAs devices and circuits for heterodyne receiver applications.* International journal of high speed electronics, 1995. **6**(1): p. 125-61.
44. Zhong, H. *Inspection of Space Shuttle Insulation Foam Defects Using a 0.2 THz Gunn Diode Oscillator*. in *IEEE conference Digest of the 2004 Joint 29th International Conference on Infrared and Millimeter Waves and 12th International Conference on Terahertz Electronics*. 2004.
45. Federici, J.J.F., *THz imaging and sensing for security applications-explosives, weapons and drugs.* Semiconductor Science and Technology, 2005. **20**(7): p. S266-80.
46. Leahy-Hoppa, M.M.R., *Wideband terahertz spectroscopy of explosives.* Chemical Physics Letters, 2007. **434**(4): p. 227-30.
47. Frost and Sullivan, *The Market for Obstacle Sensing Technologies in Passenger Cars and Commercial Vehicles in Europe*. 2005.
48. Khlopov, G. and Schuenemann, K., *Application of Millimetre Wave Coherent Radar for Remote Measurement of Vibrations and Displacements*. in *Conference Digest of the 2004 Joint 29th International Conference on Infrared and Millimeter Waves and 12th International Conference on Terahertz Electronics* 2004: IEEE.
49. Barth, H. and Menzel, W., *GaAs Gunn Oscillators Reach the 140 GHz Range*. in *Microwave Symposium Digest, 1985 IEEE MTT-S International*. 1985.
50. Neylon, S.S., *State-of-the-art performance millimetre wave gallium arsenide Gunn diodes using ballistically hot electron injectors.* IEEE MTT-S International Microwave Symposium Digest, 1989. **1**: p. 519-522.
51. Beton, P.P.H., *Use of n⁺ spike doping regions as nonequilibrium connectors.* Electronics letters, 1988. **24**(7): p. 434-435.
52. Kiuru, T., et al. *Gunn oscillator modeling and second harmonic output power optimization at 76 GHz*. in *Microwave Symposium Digest, 2008 IEEE MTT-S International*. 2008.
53. Carlstrom, J.E., Plambeck, R.L., and D.D. Thornton, *A Continuously Tunable 65--15-GHz Gunn Oscillator.* Microwave Theory and Techniques, IEEE Transactions on, 1985. **33**(7): p. 610-619.
54. Jones, S. H., Zybura, M. F., Carlstrom, J. E. and O'Brien, T. M., *A 63-170 GHz second-harmonic operation of an InP transferred electron device.* Electron Devices, IEEE Transactions on, 1999. **46**(1): p. 17-23.
55. Van Zyl, R., Perold, W., and Botha, R.. *The Gunn-diode: fundamentals and fabrication*. in *Communications and Signal Processing, 1998. COMSIG '98. Proceedings of the 1998 South African Symposium on*. 1998.
56. Bullman, J., Hobson, G.S, and Taylor, B.C., *The Gunn-Hilsum Effect*. 1979, New York: Academic Press Inc.

57. Wang, B., AbouElnour, A., and Schunemann, K., *Determination of the influence of doping profile on the performance of mm-wave gunn elements by using an efficient physical simulator.* International journal of infrared and millimeter waves, 1996. **17**(7): p. 1205-1218.
58. Butcher, P.P.N., *Theory of stable domain propagation in the Gunn effect.* Physics letters, 1965. **19**(7): p. 546-547.
59. Dunn, G. and Kearney M., *A theoretical study of differing active region doping profiles for W-band (75-110 GHz) InP Gunn diodes.* Semiconductor science and technology, 2003. **18**(8): p. 794-802.
60. Teoh, Y., Dunn, G., Priestley, N. and Carr, M., *Monte Carlo simulations of asymmetry multiple transit region Gunn diodes.* Semiconductor science and technology, 2005. **20**(5): p. 418-422.
61. Kamoua, R. and Eisele H., *Theoretical and experimental comparison of optimized doping profiles for high-performance InP Gunn devices at 220-500 GHz*, in *2003 Ieee Mtt-S International Microwave Symposium Digest, Vols 1-3*, H. Thal, Editor. 2003, Ieee: New York. p. 907-910.
62. Pilgrim, N., Khalid, A., Dunn, G. and Cumming, D., *Gunn oscillations in planar heterostructure diodes.* Semiconductor science and technology, 2008. **23**(7): p. 075013.
63. Bosch, B.G. and Engel, R.W.H., *Gunn-effect electronics*. 1975: London (etc.) : Pitman.
64. Bulman, P.J., *Transferred electron devices* 1972: New York ; London : Academic Press.
65. Navon, D.H., *Semiconductor Microwave and Materials*. 1987: HRW Int. Edition.
66. Li, S.S., *Semiconductor physical electronics*. Microdevices. 1993 New York : Plenum.
67. Couch, N.N.R., *Hot electron injection in millimetre wave Gunn diodes.* Solid-state electronics, 1989. **32**(12): p. 1685-8.
68. Ruch, J.J.G., *Temperature dependence of the transport properties of gallium arsenide determined by a Monte Carlo method.* Journal of applied physics, 1970. **41**(9): p. 3843-9.
69. Couch, N.N.R., *The use of linearly graded composition AlGaAs injectors for intervalley transfer in GaAs: theory and experiment.* Solid-state electronics, 1988. **31**(3): p. 613-16.
70. Lee, C.C., *Monte Carlo comparison of heterojunction cathode Gunn oscillators.* Electronics letters, 1990. **26**(7): p. 425-7.
71. Copeland, J.J.A., *A new mode of operation for bulk negative resistance oscillators.* Proceedings of the IEEE, 1966. **54**(10): p. 1479-1480.
72. Copeland, J.J.A., *Characterization of bulk negative-resistance diode behavior.* IEEE transactions on electron devices, 1967. **14**(9): p. 461-463.
73. Copeland, J., *LSA Oscillator-Diode Theory.* Journal of applied physics, 1967. **38**(8): p. 3096.
74. Harrison, W.W.A., *Universal linear-combination-of-atomic-orbitals parameters for d-state solids.* Physical review. B, Condensed matter, 1980. **21**(8): p. 3214-21.
75. Greenwald, Z.Z., *The effect of a high energy injection on the performance of mm wave Gunn oscillators.* Solid-state electronics, 1988. **31**(7): p. 1211-14.
76. Missous, M., *Conduction and Valence Band Offsets at the AlGaAs/GaAs heterostructure interface*. Properties of Aliminium Galium Aesenide, ed. S. Adachi. 1991: IEE INSPEC. 325.

77. Missous, M., *In situ, near-ideal epitaxial $Al_xGa_{1-x}As$ Schottky barriers formed by molecular beam epitaxy.* Journal of applied physics, 1990. **68**(5): p. 2239-45.
78. Vurgaftman, I.I., *Band parameters for III-V compound semiconductors and their alloys.* Journal of applied physics, 2001. **89**(11): p. 5815-75.
79. Stock, J., *Herstellung und Charakterisierung von GaAs Gunn-Dioden für Anwendungen bei 77GHz*. 2003, University of Aachen RWTH Aachen.
80. VWF Interactive Tools, *Device Simulation Software*. Vol. CA 95054. 2005, Santa Clara: SILVACO International.
81. Atlas User's Manual, *Device Simulation Software*. Vol. Version 5.10.R,. 2005, Santa Clara: SILVACO International.
82. DevEdit, *User's Manual*. 2006, Santa Clara, CA 95054: SILVACO International.
83. DeckBuild, *User's Manual*. Vol. Version 3.26.R. 2005, Santa Clara, CA 95054: SILVACO International.
84. TonyPlot, *User's Manual*. Vol. Version 3.4.0.R. 2006, Santa Clara, CA 95054: SILVACO International.
85. Palankovski, V. and Quay, R., *Analysis and simulation of heterostructure devices*. 2004, Wien, Austria: Springer.
86. Palankovski, V., Schultheis, R., and Selberherr, S., *Simulation of power heterojunction bipolar transistors on gallium arsenide.* Electron Devices, IEEE Transactions on, 2001. **48**(6): p. 1264-1269.
87. Caughey, D.M., *Carrier mobilities in silicon empirically related to doping and field.* Proceedings of the IEEE, 1967. **55**(12): p. 2192-2193.
88. Barnes, J.J.J., *Finite-element simulation of GaAs MESFET's with laterall doping profiles and submicron gates.* IEEE transactions on electron devices, 1976. **23**(9): p. 1042-1048.
89. Shockley, W.W., *Statistics of the recombinations of holes and electrons.* Physical review, 1952. **87**: p. 835-842.
90. Hall, R.R.N., *Electron-hole recombination in germanium.* Physical review, 1952. **87**: p. 387-387.
91. Wachutka, G.G.K., *Rigorous thermodynamic treatment of heat generation and conduction in semiconductor device modeling.* IEEE transactions on computer-aided design of integrated circuits and systems, 1990. **9**(11): p. 1141-9.
92. Farahmand, M., *Monte Carlo simulation of electron transport in the III-nitride wurtzite phase materials system: Binaries and ternaries.* IEEE transactions on electron devices, 2001. **48**(3): p. 535-542.
93. Stratton, R., *Semiconductor current-flow equations (diffusion and degeneracy).* Electron Devices, IEEE Transactions on, 1972. **19**(12): p. 1288-1292.
94. Stratton, R., *Diffusion of Hot and Cold Electrons in Semiconductor Barriers.* Physical Review, 1962. **126**(6): p. 2002.
95. Meinerzhagen, B., Bach, K. H., Bork, I. and Eng, W. L., *A New Highly Efficient Nonlinear Relaxation Scheme for Hydrodynamic MOS Simulations*. in *Numerical Modeling of Processes and Devices for Integrated Circuits, 1992. NUPAD IV. Workshop on*. 1992.
96. Apanovich, Y., et al., *Numerical simulation of submicrometer devices including coupled nonlocal transport and nonisothermal effects.* Electron Devices, IEEE Transactions on, 1995. **42**(5): p. 890-898.
97. Apanovich, Y., Blakey, P., Cottle, R., Lyumkis, E., Polsky, B., Shur, A. and Tcherniaev, A., *Steady-state and transient analysis of submicron devices*

using energy balance and simplified hydrodynamic models. Computer-Aided Design of Integrated Circuits and Systems, IEEE Transactions on, 1994. **13**(6): p. 702-711.

98. Manual, S.I.A.U.s., *Device Simulation Software*. Vol. Software version 5.16.3.R. 2010, Santa Clara, CA 95054: SILVACO International.
99. Amir, F., Farrington, N., Tauqeer, T. and Missous, M., *Physical Modelling of a Step-Graded AlGaAs/GaAs Gunn Diode and Investigation of Hot Electron Injector Performance*. in *Advanced Semiconductor Devices and Microsystems, 2008. ASDAM 2008. International Conference on*. 2008.
100. Amir, F., Farrington, N., Tauqeer, T. and Missous, M., *Development of a novel 3D physical model of an advanced mm-wave Gunn diode with hot-electron injection*, in *17th European Heterostructure Technology Workshop, HETECH 2008* 2008: Venice, Italy.
101. Amir, F., Mitchell, C., Farrington, N. and Missous, M., *Advanced Gunn Diode as High Power Terahertz Source for a Millimetre Wave High Power Multiplier*. in *SPIE Europe Security + Defence 2009*. 2009. Berliner Congress Centre, Berlin, Germany, Berlin Germany: SPIE.
102. Amir, F., Farrington, N., Mitchell, C. and Missous, M., *Time-domain analysis of sub-micron transit region GaAs Gunn diodes for use in terahertz frequency multiplication chains*. in *SPIE Europe Security + Defence 2010, SD108 ‘Millimetre Wave and Terahertz Sensors and Technology*. 2010. Centre de Congrès Pierre Baudis, Toulouse, France: SPIE.
103. Farrington, N. Norton, P., Carr, M., Sly, J. and Missous, M., *A ruggedly packaged D-Band GaAs Gunn diode with hot electron injection suitable for volume manufacture.* IEEE MTT-S International Microwave Symposium digest, 2008. **1-4**: p. 282-285.
104. Amir, F., Mitchell, C. and Missous, M., *Development of advanced Gunn diodes and Schottky multipliers for high power THz sources*, in *8th International Conference on Advanced Semiconductor Devices & Microsystems (ASDAM 2010)*, 2010.